Università di Roma "Sapienza"
Dottorato in Scienza Chimiche
XXIII ciclo

Formation and transformation of complex Silicon structures

Sergio Orlandini

University of Rome "Sapienza"
Chemistry Department

and
C.A.S.P.U.R.
Consorzio interuniversitario per le Applicazioni di Supercalcolo
Per Univerità e Ricerca

Tutors:
Prof. F.A. Gianturco
PhD. S. Meloni

A thesis submitted for the degree of
PhilosophiæDoctor (PhD)

2010 October

Contents

Chapter 1

Introduction

The present information and communication technology industry is based on the Silicon technology. The success of this technology is due to the significant increase of performance and reduction of costs achieved over years. The Moore's law [1], that predict a dubling of the number of transistors on a chip every two years, has been obeys till nowadays. However, micro-electronic is going towards the problem of "electronic bottleneck". Indeed, as the number of transistors inside a chip increases more interconnecting wires must be included in the chip to link the transistors. For instance current chips contain one kilometer of wires per cm^2. Sending informations along these wires introduce delays in signal transmission and an increase in power dissipation. The scaling process exacerbates both of these problems and the overall performance may be compromised. Until these days, the problem of the "electronic bottleneck" was postponed by the use of appropriate materials, such as Aluminum or Copper, for the interconnections between transistors. However a new approach to information transfers become necessary if Silicon devices will continue to shrink in the future.

A very promising approach is to use optical inter-connections between the transistors. No more electrons but photons will transport information under the form of an optical signal. By adopting this solution there will be the elimination of both problems: the delay in the transport of information and of power dissipation in signal propagation. The main goal of the micro-photonics is the development of a device that can emits/receives light signals and that can be efficiently integrated in Silicon based chips. A very appealing idea would be to make also this component by Silicon. Unfortunately bulk Silicon is a poor ma-

terial for light emitting devices, because it has an indirect electronic band gap. This means that the emission or absorption of a photon requires a simultaneous absorption or emission of a phonon in order to conserve the crystal momentum. Therefore the emission/absorption of a photon is a three particles process with a very low rate. Due to this reason, for long time Silicon has been considered not suitable for optical applications. However, Silicon nano-structures have been identified as a promising material for photonics. Indeed, once a semiconductor is reduced to the nano-scale the probability associated to an optical transition increases. This is due to the confinement which increases the energy gap between the valence and conduction band and introduces uncertainty on the momentum. The last effect relaxes the momentum conservation rule and allows a greater portion of the phonon density of states to assist the indirect band-to-band transition [2]. Moreover, the shrinking of the dimension of the system confines spatially the wave-functions of both the electron and the hole which are responsible for the transition. Thus, the rate of the optical transition is higher because, according to the Fermi's golden rule, it is proportional to the overlap integral that connects the wave-functions of the electron and the hole with the dipole operator [3].

The interest around nano-structured Silicon material as useful optical device began in the early nineties with the first experimental evidence of photoluminescence from porous Silicon by Canham [4]. After this first evidence, a great interest was focused on the Silicon nano-structure materials. The porous Silicon resulted to be not suitable for industrial applications due to its great chemical reactivity and very fragile mechanical nature. In order to solve these drawbacks Silicon nano-structures are embedded in a matrix. A lot of experimental works has been conducted with the aim of finding the best material for opto-electronic applications. At the moment the most promising candidate are the Silicon nano-particles embedded in an amorphous matrix of SiO_2 [5].

The optical efficiency of this system strongly depends on the structural properties, as the dimension, shape and phase (amorphous or crystalline), of the Silicon nano-particles. For instance, the optical emission can be tuned by simply varying the dimension of the nano-structures of Silicon [4, 6, 7]. These structural properties depend on the method and on the conditions under which the Silicon nano-particles are formed. Typically, Si nano-particles embedded in amorphous SiO_2 (a-SiO_2) are produced by starting from Silicon-rich a-SiO_2 samples. These

samples can be obtained by implanting Si atoms in stoichiometric a-SiO_2 or by interleaving a-SiO_2 to Si layers. In all cases, Si nano-particles are obtained after a proper thermal treatment. While the procedure for obtaining a generic Si/a-SiO_2 system is "as simple as just described", obtaining a system with well defined properties (size, nature of the nano-particle - if ordered or disordered) is much more complex. With the objective of optimizing this process, a significant effort was made to identify the formation mechanism of the nano-particles. However, the interplay between many parameters (temperature, size of the nano-particle, stoichiometry of the sample, etc.) prevented its clear identification via experiments.

Computer simulations can be a useful tool to get microscopic understanding of the physical process. Indeed, atomistic simulations, and in particular molecular dynamics (MD), might be helpful to achieve this objective but, unfortunately, often the characteristic time of these processes largely exceeds the timescale reachable by MD. In fact, often two meta-stable state, i.e. local minimum of the free energy, are separated by free energy barriers exceeding the thermal energy ($\Delta F \gg k_B T$ with F the free energy, k_B the Boltzmann constant and T the temperature). In these cases, the system spends a long time in a meta-stable state and rarely jumps to another state. Thus, a brute force simulation becomes prohibitively time consuming. As a consequence the evaluation of the free energy in the transition region is poor. In fact, the free energy is defined as the logarithm of the probability of observing the system in a given state, therefore its calculation requires an accurate estimate of this probability. A brute force molecular dynamics simulation will spend most of the time by sampling a region of the space that is irrelevant to the transition event. Instead let us image to force a MD trajectory to focus the sampling on transition region without wasting of time on the portion of the phase space where the rare events did not occur. In this way the statistical sampling of rare events will be accurate enough to get quantitative informations on the process.

In recent years, progresses on simulations of rare events provided techniques for overcoming the timescale problem. A variety of methods for computing the free energy have been developed, such as Umbrella Sampling [8, 9, 10], Meta-Dynamics [11], Temperature Accelerated Molecular Dynamics [12], etc.. A common approach shared by these methods is to describe the process in terms of a

set of collective variables rather than the actual configuration of the system. The collective coordinates are variables that depend on the configurations of all the atoms in a system and they are able to characterize the states of this system. For instance, let suppose to describe the isomerization of the cyclohexane. A useful choice of collective variables should be its torsional angles θ, ϕ. These collective variables depend on the position of all the six Carbon atoms. A certain realization of these collective variables identified a possible configuration of the cyclohexane. The discrimination between the boat and the chair conformation is due to the torsional angle θ, indeed, the chair is given by $\theta = 0°, 180°$, while $\theta = 90°$ corresponds to a boat. The probability to observe the system at a given value of θ is $P_\theta(\theta^*) = 1/\mathcal{Z} \int dx\ \rho(x)\ \delta(\theta(x) - \theta^*)$, where $\rho(x)$ is the probability density function (e.g. $e^{-\beta V(x)}$ for the canonical ensemble), $\mathcal{Z}$ is the relative partition function, $\delta(\cdots)$ is the Dirac's delta function and θ^* is a realization of the collective variable $\theta(x)$. As explained before the free energy of the system is related to the logarithm of this probability. The torsional angle θ is a good collective variable for the isomerization of the cyclohexane because the value of the angle describes the progress of the reaction of the molecule passing from a state to another. It is worth to mention that this collective coordinates would simplify the description of the process especially if the reactive is carried on in solution, where the actual position of the solvent molecules, especially those far apart from the cyclohexane, play no role in the isomerization. This latter argument is valid in general in most of the process occurring in condensed phase, where the actual configuration of the atoms belonging to the environment is irrelevant to the process. We applied collective variable based methods for reconstructing the free energy to the study of order-disorder phase transition in Si nano-particles embedded in a-SiO_2.

The collective variables can also be a useful tool to simply monitor the occurrence of a particular process. In Sec.(4) an accurate study of the self-diffusion in a-SiO_2 will be exposed. A particular set of collective variables is developed in order to monitor the occurrence of certain mechanisms of diffusion. The diffusion of Si (and O) in a-SiO_2 is very important for the formation of Si nano-particles as it is thought that the Ostwald ripening mechanism is the limiting step in this process. The principle of Ostwald ripening is that the growth of larger nano-particles is due to the diffusion of atoms from smaller ones. This is due to the fact that larger nano-particles are thermodynamically more favorable than smaller ones for

lower surface/volume ratio. Therefore the knowledge of the activation energy of Si self-diffusion in a-SiO_2 could give us indications on the mechanism of formation of Silicon nano-particles.

This thesis is organized as follows. In Sec.(2) is described the force field used for simulations of the Silicon-Silica system. This potential is relatively new (published in 2006) and little is known on the corresponding phase diagram. Therefore, with the aim of further validating the potential and correctly positioning our simulations on the diffusion in a-SiO_2 and phase change in Si nano-particles, the theoretical phase diagram of SiO_2 is computed. We studied the phase diagram of this material rather than that of Si for several reasons. First, the phase diagram is very rich, with several crystalline structures and it is therefore more challenging to reproduce. Second, since this potential does not include explicit electrostatic terms, the reproduction of the phase diagram of SiO_2 is once again expected to be more challenging. The results of this study are presented in Sec.(3). In Sec.(4) the self diffusion in a-SiO_2 is analyzed. While in Secs.(5, 6) is analyzed the problem of the phase transition of a Si nano-particle embedded in a a-SiO_2 matrix from the crystalline to the amorphous phase.

Finally the last chapter is the result of a period of study spends at the University College of Dublin in the group of Prof. G.Ciccotti funded by a grant of the SimBioMa scientific network. This chapter deals with the hydrodynamic evolution of an interface between two immiscible liquids. This problem is an example of an application of a method for non-equilibrium simulations that has been developed in collaboration with Prof. Ciccotti during this scientific visit. In the chapter will be presented a rigorous method to evaluate ensemble average in a non-equilibrium system subject to macroscopic initial conditions.

Chapter 2

Potential

Classical interatomic potential are less accurate than *ab-initio* methods, but such potentials are invaluable for treatment of complex and large systems of thousands of atoms or for extended in time calculations. Indeed molecular dynamic simulations using empirical potentials are a powerful tool for studying systems with a great number of atoms (10^4 or more).

For Silicon and Silica, several empirical potentials have been used. The most successful are the Stillinger-Weber potential [14], the van Beest, Kramer and van Santen (BKS) potential [15], Tersoff potential [16, 17, 18] and its modified version [19, 20].

The Stilling-Weber potential is widely used in molecular dynamic simulation of pure Si and Silica, since the melting point and other properties are well reproduced. The BKS potential is also a frequently used potential for Silicon based systems. However, the BKS does not contain any three body term. Many body effects is of crucial importance in reproducing the energetics and structures of amorphous silica. In particular in the case in which the silica is subject to heterogeneous environment like at the liquid-crystal interface or in the case of surfaces. A useful characteristic of this potential is the presence of environment-dependent terms which allows to properly treat various kinds of defects on distortions of the original geometry. A drawback of the BKS potential is that it includes a explicit electrostatic term, which makes it computationally expensive and therefore inadequate for large scale simulations. On the contrary, such a term is not present in Tersoff-like potential and this fact, together with their reliability makes them perhaps the most used class of force field for Si-based material simulations.

The environment-dependency in the original Tersoff potential was introduced by making the two and three body term depending on the coordination of the atoms [16]. The Tersoff potential is well known to reproduce reasonably well several properties of liquid and amorphous Si. However, in disagreement with experimental results, it favors the four-fold coordination in liquid Silicon and the simulated melting temperature is much higher than the experimental value. These drawbacks are partially solved in a Tersoff-like potential proposed by Billeter *et al.* [19, 20]. In the next section I will present this modified Tersoff potential used in the simulations.

1 Modified Tersoff Potential

The modified version of the Tersoff potential is a short-range potential for covalent systems where the environment-dependence is introduced via an effective coordination number that affect the strength of the bonds (two body term). Moreover, a penalty term is added to reduce the tendency of the original Tersoff potential to produce highly undercoordinated samples.

The functional form of the Billeter *et al.* potential is

$$E = \frac{1}{2}\sum_{i\neq j} V_{ij} + \sum_{I} N_I E_I^0 + \sum_{i} E_i^c \tag{2.1}$$

where V_{ij} is a generalized Morse potential, N_I is the number of atoms of the I-th element, E_I^0 is the core energy, and E_i^c is the penalty for under and over coordination.

The generalized Morse potential V_{ij} is an explicit function of the distance r_{ij} between the atoms i and j,

$$V_{ij} = f_{ij}^{IJ}\left[A_{IJ}\, e^{-\lambda_{IJ}\, r_{ij}} \;-\; b_{ij}^{IJ}\, B_{IJ}\, e^{-\mu_{IJ}\, r_{ij}}\right] \tag{2.2}$$

where I, J are indices for the species of the atoms i and j, f_{ij}^{IJ} is a cutoff function, b_{ij}^{IJ} is the damping factor, λ_{IJ} and μ_{IJ} are the inverse decay lengths, A_{IJ} and B_{IJ} are coefficients.

The environment-dependence is included in the b_{ij}^{IJ} term. All the deviations from a simple pair potential are due to the dependence of the b_{ij}^{IJ} term upon

the chemical environment. In practice, b_{ij}^{IJ} represents the strength of the bond between the atoms i and j.

The cutoff function is used to restrict the range of the potential to the first coordination shell and it is defined as

$$f_{ij}^{IJ} = \begin{cases} 1 & \text{if } \mathrm{r_{ij}} \leq \mathrm{R_{IJ}} \\ \frac{1}{2}\left[1 + \cos\left(\pi \frac{r_{ij} - R_{IJ}}{S_{IJ} - R_{IJ}}\right)\right] & \text{if } \mathrm{R_{IJ}} < \mathrm{r_{ij}} \leq \mathrm{S_{IJ}} \\ 0 & \text{if } \mathrm{r_{ij}} > \mathrm{S_{IJ}} \end{cases} \tag{2.3}$$

where R_{IJ} and S_{IJ} are the inner and outer cutoff radii between elements of the species I and J.

The inverse decay lengths λ_{IJ} and μ_{IJ}, the cutoff distances R_{IJ} and S_{IJ}, and the coefficients A_{IJ} and B_{IJ} depend only on the type of the two interacting atoms. For multicomponent systems the coefficients are defined through the following combination rules:

$$A_{IJ} = (A_I A_J)^{1/2}, \quad B_{IJ} = (B_I B_J)^{1/2} \tag{2.4}$$

$$R_{IJ} = (R_I R_J)^{1/2}, \quad S_{IJ} = (S_I S_J)^{1/2} \tag{2.5}$$

and

$$\lambda_{IJ} = \frac{\lambda_I + \lambda_J}{2}, \quad \mu_{IJ} = \frac{\mu_I + \mu_J}{2} \tag{2.6}$$

see Tab.2.1 for the values of these coefficients.

The three-body term, which takes into account the local symmetry, is introduced into the damping factors b_{ij}^{IJ} of the two-body attractive interaction through the effective coordination number $\beta_I \, \zeta_{ij}^{IJ}$:

$$b_{ij}^{IJ} = \chi_{IJ} \left[1 + \left(\beta_I \, \zeta_{ij}^{IJ}\right)^{n_I}\right]^{-\frac{1}{2n_I}} \tag{2.7}$$

where χ_{IJ}, β_I and n_I are parameters (see Tab.2.1), and ζ_{ij}^{IJ} is defined by

$$\zeta_{ij}^{IJ} = \sum_{k \neq i,j} f_{ik}^{IK} \, e_{ijk}^{IJK} \, t_{ijk}^{I} \tag{2.8}$$

where the sum runs over all the neighbours of the i-th atom apart the atom j. Here the terms e_{ijk}^{IJK} and t_{ijk}^{I} represents, the radial and the angular influence of a third atom on the bond between atoms i and j, respectively.

Parameter	Silicon	Oxygen
A_I	1830.80	3331.06
B_I	471.175	260.477
λ_I	2.45918	3.75383
μ_I	1.76191	3.35421
R_I	2.44810	2.26069
S_I	3.08355	3.31294
β_I	1.0999×10^{-6}	0.28010
n_I	0.78665	0.75469
m_I	3	1
c_I	1.0039×10^{5}	0
d_I	16.21697	1
h_I	-0.59912	0.96783

Table 2.1: Parameters of the modified Tersoff potential of Ref.[19]. Values are in eV, Å, and Å^{-1}.

The term e_{ijk}^{IJK} is introduced in order to take into account the fact that the radial influence of a third atom k on the bond between the atom i and j decreases when the distance r_{ik} becomes larger than the distance r_{ij} between i and j. The term e_{ijk}^{IJK} takes the form

$$e_{ijk}^{IJK} = e^{(\mu_{IJ}\, r_{ij} - \mu_{IK}\, r_{ik})^{m_I}}. \tag{2.9}$$

The term t_{ijk}^{I} incorporates the effect of the angle $i\hat{j}k$ (θ_{ijk})

$$t_{ijk}^{I} = 1 + \frac{c_I^2}{d_I^2} - \frac{c_I^2}{d_I^2 + (h_I - \cos(\theta_{ijk}))^2} \tag{2.10}$$

The pairwise interaction term is augmented by the core energies E_I^0, the second term (Eq.2.1). This term allows to make simulations at varying composition (e.g. gran-canonical MC). Moreover, another term is added, namely $\sum_i E_{i^c}$, that allows to properly treat coordination defective samples This further term is fundamental in the case of systems with an interface, such as those treated in this thesis. It is worth to mention that the occurrence of over coordination or under coordination is also included in the damping term (Eq.2.7). However, the

Parameter	Si-O
$A_{IJ}/(A_I A_J)^{1/2}$	1.04753
$B_{IJ}/(B_I B_J)^{1/2}$	1.00000
$\lambda_{IJ} - (\lambda_I + \lambda_J)/2$	0.67692
$\mu_{IJ} - (\mu_I + \mu_J)/2$	-0.43480

Table 2.2: Coefficients of mixed terms for Si-O species of the modified Tersoff potential of Ref.[19]

dependence on the coordination of this term only would not be sufficient. I shall illustrate this problem with an example. Consider the case in which the atom i is over/undercoordinated while the coordination of the atom j is the regular one. In this case only the term V_{ij} is damped, while the corresponding term V_{ji} remains unaffected. This drawback favors the formation of defects at Si/SiO_2 interfaces. In order to avoid this inconvenience the following miscoordination penalty term is added

$$E_i^c = c_{I,1}\,\Delta z_i + c_{I,2}\,\Delta z_i^2 \tag{2.11}$$

where Δz_i is the deviation from the expected coordination number and is given by

$$\Delta z_i = \frac{z_i - z_I^0}{|z_i - z_I^0|}\, f_s(|z_i - z_I^0|) \tag{2.12}$$

here z_I^0 is the ideal coordination numbers while z_i, the actual coordination, is given by

$$z_i = \sum_{j \neq i} f_{ij}^{IJ}\, b_{ij}^{IJ} \tag{2.13}$$

and $f_s(z)$ is a switching function that avoid discontinuity along the dynamic in case of bond breaking and formation. The functional form of $f_s(z)$ is

$$|f_s(z)| = int(|z|) + \begin{cases} 0 & \text{if } |z| \leq z_T - z_B, \\ \frac{1}{2}\left[1 + \sin\left(\pi \frac{|z| - z_T}{2 z_B}\right)\right] & \text{if } z_T - z_B < |z| \leq z_T + z_B, \\ 1 & \text{if } z_T + z_B < |z| \end{cases} \tag{2.14}$$

where $z_T = 0.49751$ and $z_B = 0.200039$ are equal for all the elements.

Parameter	Silicon	Oxygen
E_I^0	-103.733	-432.158
z_I^0	3.70	2.80
$c_{I,1}$	-0.1238	-0.0038
$c_{I,2}$	0.2852	0.1393

Table 2.3: Parameters of the terms in Eqs.(2.11,2.12,2.13,2.14). The values of E_I^0 are in eV.

Previous works have shown that this potential is able to correctly reproduce several properties of SiO_2 and Si/SiO_2 systems [19, 21, 22]. In Particular, we tested the ability of the Billeter *et al.* potential to reproduce the energetics and the path for the Oxygen vacancy-mediated diffusion in crystalline SiO_2. We started from the NEB trajectory obtained by Laino *et al.* [23] based on an *ab initio* force model. We performed a NEB simulation using the Billeter *et al.* potential finding a migration energy which is the 80 % of that found by Laino et al. The agreement between classical and *ab initio* configurations along the NEB trajectory is even better, being the maximum difference in the bond lengths lower than 3 %.

Chapter 3

Phase Diagram of Silicon Dioxide

A key element in the description of a material is its phase diagram. The phase diagram is the stability fields of the liquid, gas and various crystal phases as function of thermodynamical variables. In a phase diagram is reported the domains of stability of the various phases of a given system with respect to the thermodynamic variables (V, T, P, $\{x_i\}_{i=1,N}$i in the case of multicomponent systems, etc.). The knowledge of the stability domains of the various phases is crucial in simulation to define the external conditions (P, T, etc.) at which to run the calculation as, usually, neither classical nor ab-initio force field reproduce well the experimental phase diagram. As a result, by picking the value of, say, P and T, in the stability domain of a given phase of the experimental phase diagram might introduce severe artifacts in the simulation results.

The aim of this section is to test the reliability of the modified Tersoff potential described in Sec.(2), which is used as potential in the calculations of Secs.(4, 5, 6). In the present section a procedure for evaluating the stability domains in the P-T diagram is presented and the results obtained for the liquid and various crystal phases of the SiO_2 are presented.

1 Theoretical Background

The phase diagram of a specie is constructed by identifying the equilibrium curves in, say, the P-T diagram. These curves represent the locus of points in which two phases are in equilibrium between them. When considering pressure and temperature as thermodynamical variables, the corresponding thermodynamic

potential is the Gibbs free energy. Two phases are in equilibrium if at a given P and T they have the same free energy. Therefore in order to evaluate the phase diagram of a species, the Gibbs free energy is determined numerically for each phase as a function of P and T.

The Gibbs free energy G is expressed as:

$$G = H - TS \tag{3.1}$$

where S is the entropy and $H = E - PV$ is the enthalpy. NPT simulations are strongly affected by finite size effects, therefore, following [24], the Gibbs free energy of the system is indeed computed by NVT MD simulations. The Gibbs free energy is given by the following equation

$$G(P,T) = E(P^*,T) + V^*P - TS(P^*,T) \tag{3.2}$$

where V^* is the average molar volume corresponding to the target pressure P. This approach is based on the observation that in the thermodynamic limit any average over the NPT ensemble is the same as the average over the NVT one. The way in which the various components of the Gibbs free energy are computed is explained in Sec.(2).

We restrict our attention to the liquid and few crystal phases of the silica. Five different crystal structures are taken in account: coesite, β-quartz, β-cristobalite and β-tridymite. A lot of other crystal phases are known for the SiO_2. However these crystal structures cover the phase diagram of the Silicon dioxide in a wide range of P and T.

For each phase, a large number of samples corresponding to the same number of points in the V-T plane are prepared. The points in the V-T plane are chosen in order to span only the range of existence of a given species. In Fig.(3.1) are reported the points corresponding to the samples simulated. Starting from these samples isobar or isotherm cuts of the $G(P,T)$ surface can be obtained. The phase diagram of the SiO_2 is evaluated analyzing the intersection of these cuts of the $G(P,T)$ surface of the different phases at the variation of T and at fixed P.

In Fig.(3.2) is reported an isobar cut of the G surface for different phases. In this figure the ΔG is reported as a function of T. It is worth to note that the ΔG is relative to the G of the β-cristobalite specie. The intersection of the curves means that the free energy of the relative phases is the same. Thus, the point of

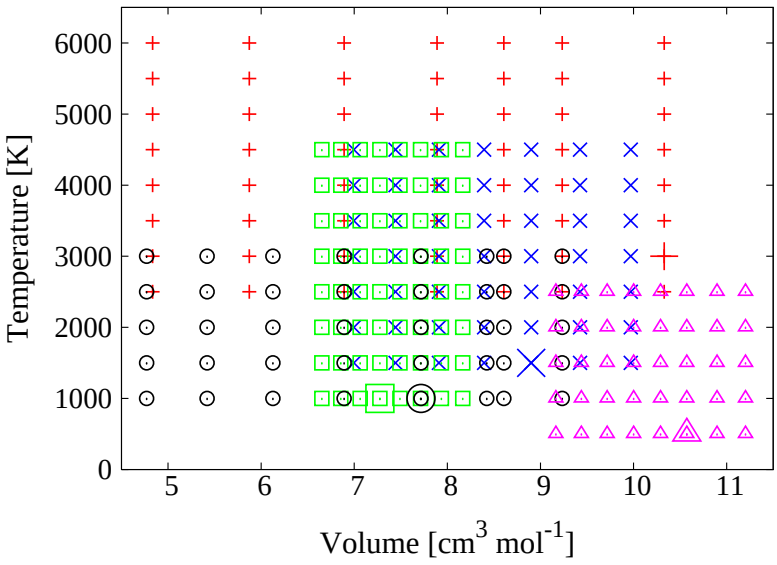

Figure 3.1: Position in the V-T plane of the state points simulated. For the liquid phase are used red pluses, for coesite green squares, for β-cristobalite black circles, for β-tridymite violet triangles, and finally for β-quartz blue crosses.

intersection of the two curves corresponds to a point in the phase diagram at the T of intersection and at the P of the isobar cut.

2 Calculation of the Gibbs Free Energy of the Various Phases

In order to calculate $G(P,T)$ from Eq.(3.2) we have to evaluate the $E(V^*,T)$, $P(V^*,T)$, $S(V^*,T)$ terms as functions of V^* and T. The computational procedure differs from the liquid to the crystalline phases. The different procedures are described separately in the following sections.

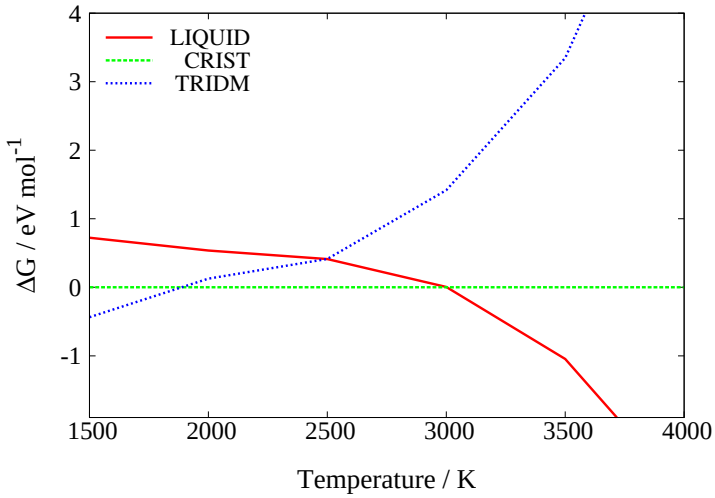

Figure 3.2: ΔG as a function of T at fixed P ($P = 0$). In the figure the ΔG is evaluated as the difference between the Gibbs free energy of a specie with respect to a reference specie. In the present case the reference specie is the β-cristobalite.

2.1 Liquid phase

The liquid phase is modeled by a sample containing 1536 atoms. The liquid samples consists of eight isochores from volumes of 4.83 cm^3 mol^{-1} to 10.59 cm^3 mol^{-1}. For each isochor the sample are equilibrated in a range of temperatures from 2500 K to 6000 K at intervals of 500 K (see Fig.(3.1)). In the present simulations the temperature is controlled via the Nosé-Hoover chain method [25] with a time step of 0.05 fs. In order to identify equilibrium curves in an accurate way we need to obtain an analytical approximation to $G(P, T)$. However, we compute the various terms of Eq.(3.2) only on a discrete grid. One pass from this discrete to a continuous representation by interpolating the data by third order, for the energy, and fourth order, for the pressure, polynomials.

In practice we first fit $E(V, T)$ along isochores

$$E(\bar{V}, T) = \sum_{n=0}^{3} \alpha_n(\bar{V})\, T^n \tag{3.3}$$

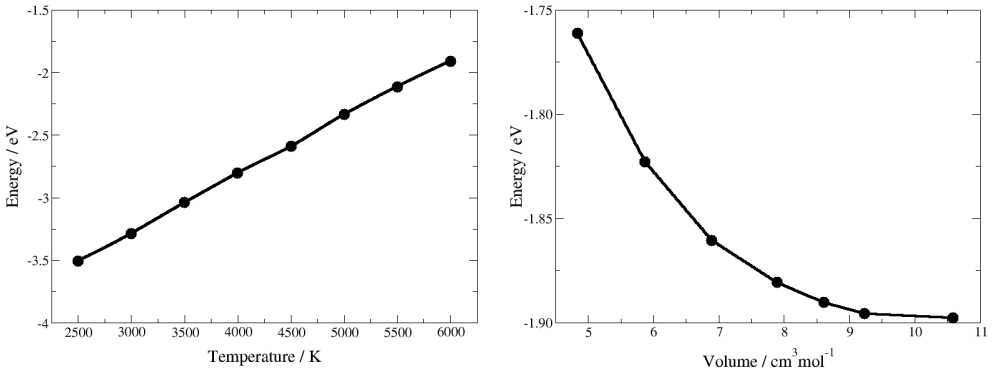

Figure 3.3: Example of the fitted procedure for E in the liquid phase. Left) E as a function of T at fixed volume $V = 6.9$ cm^3 mol^{-1}. Right) E as a function of P at fixed temperature $T = 4500$ K.

and then along isothermals

$$E(V,T) = \sum_{n=0}^{3} \sum_{m=0}^{3} \beta_{n,m} V^m \bar{T}^n \tag{3.4}$$

$P(V,T)$ is obtained in a similar way. In Fig.(3.3) and Fig.(3.4) the fitted curves of $E(V,T)$ and $P(V,T)$ are shown along an isochor and isothermal.

The value of the entropy S at a given point in V-T is calculated by thermodynamic integration using the following relation

$$S(V,T) = S_R(V_R,T_R) + \int_{T_R}^{T} \frac{1}{T} \left(\frac{\partial E(V_R,\tilde{T})}{\partial T} \right)_{V_R} d\tilde{T} + \frac{1}{T} \int_{V_R}^{V} P(\tilde{V},T)\, d\tilde{V} \tag{3.5}$$

where S_R is the entropy for a reference state at reference values of volume and temperature (V_R, T_R). Eq.(3.5) is indeed the variation of entropy from a reference state computed along a path composed of an isochor, bringing the system from (V_R, T_R) to (V_R, T), and then along an isothermal, bringing the system from (V_R, T) to (V, T). The second term of the Eq.(3.5) is evaluated analytically from the fitting for $E(V,T)$ as a function of T described above, see Eq.(3.3). While the integral over the volume is obtained numerically using the Simpson's rule from the fitting of the $P(V,T)$ as a function of V.

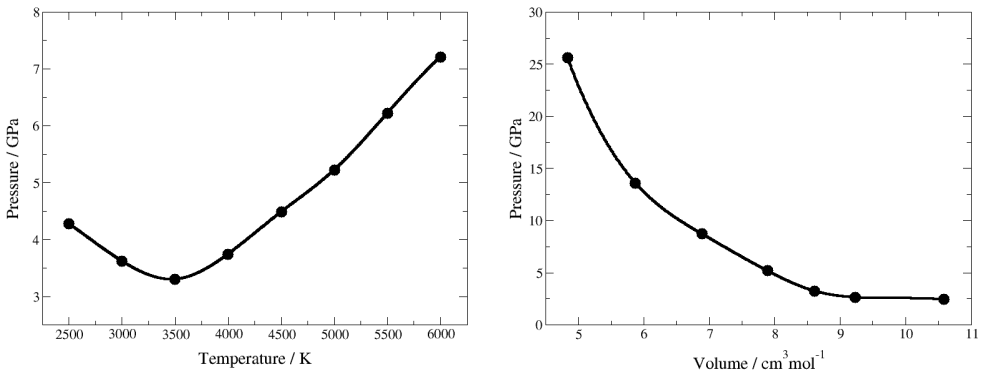

Figure 3.4: Example of the fitted procedure for P in the liquid phase. Left) P as a function of T at fixed volume $V = 6.9$ cm^3 mol^{-1}. Right) P as a function of P at fixed temperature $T = 4500$ K.

For the entropy at the reference point is used the expression of the entropy of an ideal gas composed of two species

$$\begin{aligned} S_R(V_R, T_R) = N_{Si}\, k_B \left\{ \ln \left[\frac{V_R}{N_{Si}} \left(\frac{2\pi\, m_{Si}\, k_B\, T_R}{\hbar^2} \right)^{3/2} \right] \right\} \\ + N_O\, k_B \left\{ \ln \left[\frac{V_R}{N_O} \left(\frac{2\pi\, m_O\, k_B\, T_R}{\hbar^2} \right)^{3/2} \right] \right\} \\ - k_B\, \ln(2\pi \sqrt{N_{Si}\, N_O}) \end{aligned} \tag{3.6}$$

here N_{Si}, N_O and m_{Si}, m_O are the number of atoms and the masses for Silicon and Oxygen, $\hbar$ the Planck constant and k_B the Boltzmann constant.

With the above procedure the value of E, P, and S for an arbitrary point V_0, T_0 can be obtained form molecular dynamic simulations at fixed V and T. Finally using Eq.(3.2) the value of G at the given point is evaluated for the liquid phase.

2.2 Crystal phases

As explained before, we focused on five different crystal structures. The crystal phase analyzed are: coesite, β-cristobalite, β-quartz and β-tridymite. In Tab.3.1 the crystal symmetries and lattice parameters of the crystal phases analyzed are

	β-crist. [26]	β-quartz [27]	β-trid. [28]	coesite [29]
symmetry	cubic	hexagonal	hexagonal	monoclinic
lattice	7.16	4.91 5.40	7.17 12.38	7.13 12.37 7.17
angles	90°	90° 120°	90° 120°	90° 120.34° 90°
Pearson sym.	Fd$\hat{3}$m	P$6_2$22	P6_3/mmc	C2/c
group N°	227	180	194	15

Table 3.1: crystallographic data for β-cristobalite, β-quartz, β-tridymite and coesite

reported. It is worth to note that the simulated crystal phases correspond to the main structures of the silica crystals.

In principle, the $E(V,T)$, $P(V,T)$ and $S(V,T)$ terms of Eq.(3.2) can be computed according to the procedure explained above for the liquid phase. However, at a variance with the liquid phase, the crystal one might be anisotropic. As a consequence, the ratio among the lattice parameter can change with T and V. So, the procedure for computing $G(P,T)$ must be adopted. The samples are first prepared according to experimental crystallographic data (see Tab.(3.1)). The structures at different volumes are obtained by scaling up and down the original structures. This step is followed by a geometry optimization. A 40 ps NPT simulation for relaxing the lattice structure follows. The pressure is fixed at the average value corresponding to the present volume, the latter is therefore almost preserved.

Finally a NVT simulation of 30 ps is performed, so that the average values of E and P are computed. At the end of this procedure the value of E and P at the grid points are computed. Using the same fitting procedure explained above, an approximation of the $E(V,T)$ and $P(V,T)$ surface over the entire V-T space of the given crystal are computed.

In order to estimate the entropy for an arbitrary point of the V-T plane the Eq.(3.5) can be used as in the liquid phase. However the reference state is different from the liquid phase. For a crystal phase the entropy at the reference state S_R can be approximated by

$$S_R = S_{harm} + S_{anh} \tag{3.7}$$

where the S_{harm} is the harmonic contribution and the S_{anh} is the anharmonic

one. The harmonic vibrational term is given by:

$$S_{harm} = \frac{R}{N} \sum_{i=1}^{3N-3} \left(1 - \ln \frac{\hbar \, \omega_i}{k_B \, T} \right) \tag{3.8}$$

where N is the number of the atoms, R is the gas constant, $\hbar$ is the Planck constant over 2π, k_B the Boltzmann constant and the set $\{\omega_i\}$ are the vibrational density of states. The $\{\omega_i\}$ are defined as $\omega_i = \sqrt{h_i}$, where h_i are the eigenvalues of the Hessian matrix H, which is given by

$$H_{ij} = \frac{1}{\sqrt{m_i \, m_j}} \, \frac{\partial^2 V}{\partial q_i \, \partial q_j} \, \Bigg|_{q \, = \, q_0} \tag{3.9}$$

where the set $\{m_i\}$ are the masses of the atoms, V is the interatomic potential and the set $\{q_i\}$ define the $3N$ atomic coordinates, and the notation $q = q_0$ indicates that the Hessian matrix is evaluated at the configuration corresponding to the minimum of the energy. Since the system is at a minimum, the eigenvalues of the Hessian matrix are all greater than zero, except the three zero eigenvalues corresponding to the translations modes. These three eigenvalues are excluded from the evaluation of the harmonic contribution to the entropy.

It is worth to note that in the present calculation the evaluation of the second derivatives term of the interatomic potential described in Sec.2 is calculated analytically. A complete treatment of the second derivatives of the interatomic potential is reported in Appendix A.

The anharmonic contribution to the entropy is evaluated with the formula

$$S_{anh} = \int_0^T \frac{1}{T} \left(\frac{\partial E_{anh}}{\partial T} \right) dT \tag{3.10}$$

where E_{anh} is given by

$$E_{anh}(T) = U(T) - \frac{3}{2} \, R \, T \, \left(1 - \frac{1}{N} \right) \tag{3.11}$$

here R is the gas constant, N is the number of atoms and $U(T)$ is the potential energy.

The computational procedure for the evaluation of the entropy of the reference S_R requires the choice of the reference volume V_R and temperature T_R for each of the crystal phases. The chosen reference points for each crystal phase are

reported in Fig.(3.1). Then starting from the final configuration of the previous procedure for evaluating the E and P surface the atomic position of this configuration are optimized so that the minimum energy configuration is reached. Then the eigenfrequency spectrum of the Hessian matrix (see Eq.3.9) is evaluated from these minimum energy configurations, one for each crystal phase. The eigenfrequency spectrum is evaluated diagonalizing the Hessian matrix in order to found the Hessian eigenvalues. Using Eq.(3.8) the harmonic contribution to the S_R is obtained.

To calculate S_{anh} we use the energy optimized configuration used for the evaluation of the Hessian matrix as starting point for a set of simulation at constant T and V from 100 K to 1500 K equally spaced of 100 K. First the temperature is raised from 0 K to the desired T until 1500 K. Then the systems are equilibrated at the desired T for 50 ps with a NVT simulation at constant T. From these simulations the value of E_{anh} is evaluated, see Eq.(3.11), using a polynomial fit

$$E_{anh} = c_0 + \sum_{n=2}^{n_{max}} c_n T^n \tag{3.12}$$

From the evaluation of E_{anh} using the Eq.(3.10) the value of the anharmonic contribution of S_R is obtained for each crystal phase. Finally the value of the entropy of the reference points is obtained as a sum of the harmonic and anharmonic contributions (see Eq.3.7).

With the previous procedure the E, P and S surfaces of a crystal phase are obtained for every arbitrary point (V, T). From these surface the value of the Gibbs free energy can be evaluated, as in the liquid phase.

3 Results

In Fig.(3.5) is reported the diagram of the SiO_2 in the P-T plane as obtained by the method above. The phase diagram must be compared with the experimental one reported in Fig.(3.6). It is quite evident that the agreement between theoretical and experimental diagram is only qualitative. Indeed the simulated phase diagram shows clear quantitative deficiencies. The phase boundaries between the species are not at the same condition of neither T nor P.

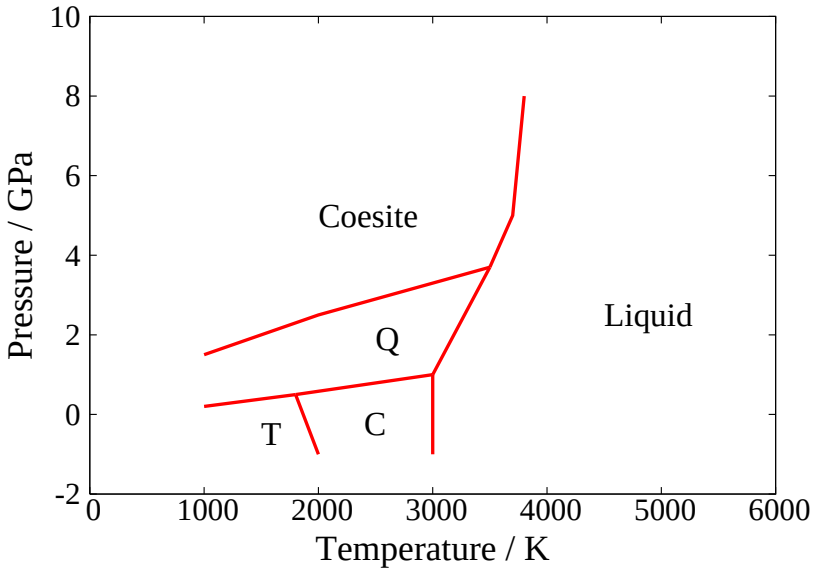

Figure 3.5: Simulated phase diagram of SiO_2 in the P-T plane. In the figure the stability fields for liquid, β-tridymite (T), β-cristobalite (C), β-Quartz (Q), and coesite phases are reported.

In particular the differences in pressure are quite marked. The coexistence curves of Fig.(3.5) are shifted at lower pressure. The diagram of Fig.3.5 reveals also significant differences in the thermal behavior. In particular the simulated melting temperature of the β-cristobalite ($\sim$ 3000 K) is much higher than the experimental one ($\sim$ 1700 K). In the Ref.[24] the phase diagram of the BKS potential [15] is obtained with the same procedure. Also in the case of the BKS potential the quantitative discrepancies are relevant. However, for the Tersoff-like potential there is a better agreement both in temperature and pressure behaviors than in the case of BKS. Indeed the melting temperature of coesite and especially of quartz are closer to the experimental value more in the Tersoff potential than in the BKS potential.

However, the phase diagram obtained from the present calculations are in qualitatively agreement with the experimental one. Indeed the position of the phases in the diagram are respected. The topology of the diagram is the same

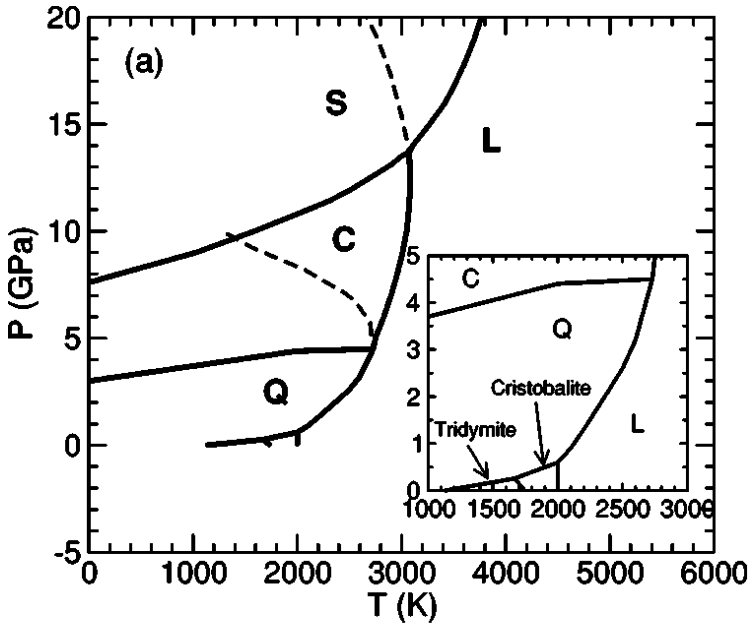

Figure 3.6: Experimental phase diagram of SiO_2 in the P-T plane. In the figure the stability fields for liquid (L), β-Quartz (Q), coesite (C), stishovite (S) phases are reported. In the inset is reported the stability fields of β-cristobalite ad β-tridymite. Figure taken from Ref.[24].

in both cases. It is worth to note that the equilibrium phases at ambient P, i.e. $P = 0$ GPa, of modified Tersoff potential are the same like the experimental diagram. Indeed at ambient temperature the stable phase is the quartz, for higher temperature first the tridymite and then the cristobalite become the stable phase. On the contrary for the BKS potential the stable phase is the coesite for all the temperature range [24]. For the modified Tersoff potential in exam, the only drawback at ambient P is that the coexistence lines between the phases are shifted at higher temperature. This means that, taking in account the deficiencies, the modified version of the Tersoff potential [19] is suitable for molecular dynamics simulations at ambient pressure.

Chapter 4

Self Diffusion in Amorphous Silicon Dioxide

Several authors suggest that the formation of nano-particles is governed by the Ostwald ripening mechanism [30] and, in particular, by the diffusivity of Si atoms from smaller to larger nano-particles. It was also found a strong dependency of the crystal growth from Si supersaturation, which seems to be in conflict with the Ostwald mechanism (see Ref.[31] and reference therein). However, also in this case, this was considered an indication that the Si diffusion is the limiting step of the overall process. It would be therefore of particular interest to study the diffusivity of Si and its mechanism in stoichiometric and non-stoichiometric conditions. Unfortunately, to the best of my knowledge, no experimental studies on diffusion of Si in amorphous SiO_2 in absence of a Si/SiO_2 extended interfaces (i.e. in real conditions for the formation of nano-particles) are available, especially concerning the identification of the mechanism of the diffusion. This is likely due to the fact that it is hard to generate a controlled concentration profile of isotopic Si into a bulk-like sample (with no interface), so as to measure its variation upon thermal annealing. However, in a recent paper, Yu et al. [31] have addressed the identification of the atomistic mechanisms of diffusion of one excess Si atom in a-SiO_2 by performing ab-initio calculations. In this paper, the authors identified possible equilibrium sites and calculated the corresponding energy barrier for the diffusion of the excess Si atom by means of the Nudged Elastic Band (NEB) method [32, 33]. However, this investigation did not take into account neither the different concentrations of excess Si atoms nor the possible fluctuation of Si

density within the samples. Finally, because of the use of NEB, the effect of temperature is not taken into account.

In this section I will present the results on the study of the diffusion mechanisms of Si and O in a-SiO_2 at different temperatures and for different Si-atoms concentrations by means of classical molecular dynamics (MD) simulations. We do not assume any *a priori* hypothesis on the mechanisms. Rather, by analyzing the MD trajectories we identify the set of most relevant mechanisms occurring at various thermodynamical and chemical conditions. Finally, we calculate the contribution of each individual mechanism to diffusion and analyze the role of thermodynamical and chemical conditions.

The section is organized as follows: in Sec.(1) the theoretical background of calculation of diffusivity within MD framework is shortly revised. Moreover a novel method for calculating the contribution of different mechanisms to the diffusivity is presented. In Sec.(2) the preparation of the sample is presented. In Sec.(3.1) the results on the diffusivity are presented and they are compared with experimental and computational results available in literature. Finally, in Sec.(3.2) the contribution of a set of possible mechanisms to the diffusivity of silicon are analyzed.

1 Theoretical Background

Solid-state self-diffusion is commonly due to several possible concurrent mechanisms, typically related to the presence and the dynamics of defects of different kind. For example, in crystals these defects typically are vacancy, self-interstitial, etc. Even though in amorphous materials the origin of self-diffusivity is less well understood, also in this case it is thought that it is induced by several concurrent mechanisms. Typically, however, the experimental interpretation of diffusivity-vs-temperature measurements is based on the phenomenological Arrhenius law

$$D(T) = D_\infty \; exp\left(-\frac{E}{k_B}\right) \tag{4.1}$$

where D_∞ is the diffusivity at high temperature and E is the (average) migration energy, representing the (average) energy barrier to be overcome during diffusion. In Eq.(4.1) T and k_B represent the temperature and the Boltzmann constant,

respectively. The theoretical atomic scale investigation on self-diffusion is rather based on the calculation of the mean square displacement (MSD), according to the Einstein random-walk equation

$$D(T) = \lim_{t\to\infty} \frac{1}{6} \frac{d\langle \Delta r^2(t) \rangle}{dt} \tag{4.2}$$

where the $t \to \infty$ limit stands for simulations performed for long enough times. Eq.(4.2) is straightforwardly implemented in molecular dynamics (MD) since the MSD is defined as

$$\langle \Delta r^2(t) \rangle \quad = \quad \langle \sum_{i=1}^{N} [\vec{r}_i(t) - \vec{r}_i(0)] \rangle \tag{4.3}$$

where $\vec{r}_i(t)$ and $\vec{r}_i(0)$ are the positions of the i-th atom at time t and time $t = 0$, respectively, and it is therefore directly computed from the computer-generated atomic trajectories. Indeed, $\langle \cdots \rangle$ is the ensemble average over all possible initial configurations and velocities. The ensemble average is extended over the configurational space available to the system. Since we perform MD simulations, the integral implied by Eq.(4.3) is calculates by means of a time average over the trajectory of the atoms. This means that we assume that the ergodic hypothesis holds true for these systems in the given thermodynamical conditions.

In addition, by means of Eq.(4.2) it is relatively easy to calculate the contribution to self-diffusion by each given mechanisms, provided that they are clearly identified. Once again, this information can be extracted by animation and inspection of atomic trajectories.

However, determining the contribution of each individual mechanism to the diffusivity is not trivial. In the following we shall demonstrate that under proper conditions the MSD is additive and therefore $D(T)$ is additive as well. We can therefore resort to Eq.(4.2) for calculating the $D(T)$ of each mechanism.

We assume that the diffusion occurs through a sequence of stepwise events. This assumption is justified by the empirical observation that indeed Si and O atoms diffuse through a stepwise mechanism in this material (see Fig.(4.1)). We can therefore rewrite Eq.(4.3) as follows

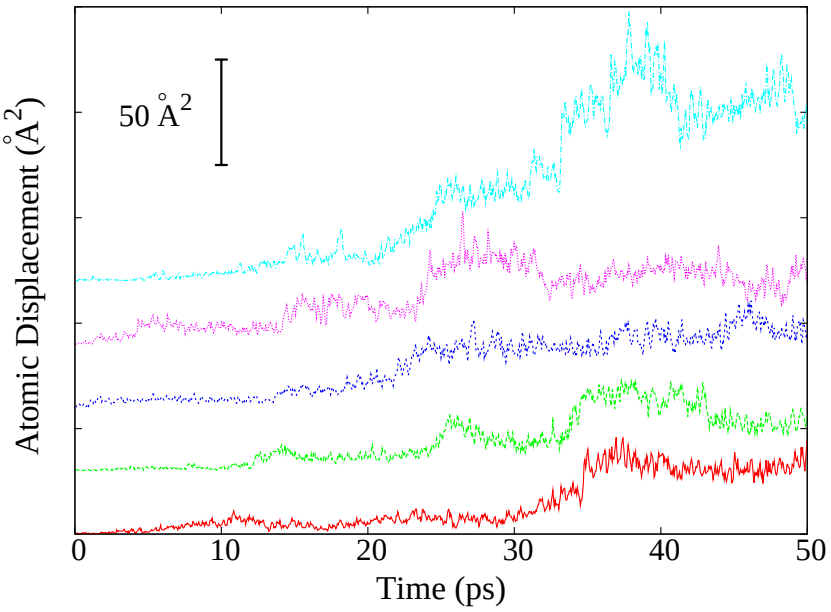

Figure 4.1: MSD displacement of few Si atoms selected randomly in the sample. The figure clearly shows that the diffusion occurs via stepwise events.

$$\langle \Delta r^2(t) \rangle = \langle \frac{1}{N} \sum_{i=1}^{N} \left[\sum_{\alpha=1}^{L} \Delta \vec{r}_i(t_\alpha) \right]^2 \rangle \tag{4.4}$$

where L is the number of diffusive steps and $\Delta \vec{r}_i(t_\alpha)$ is the (vector) displacement of i-th atom occurring at the time t_α. If the diffusive steps belong to different mechanisms, then Eq.(4.4) can be rewritten as follows:

$$\langle \Delta r^2(t) \rangle = \langle \frac{1}{N} \sum_{i=1}^{N} \left[\sum_{\alpha \in M_1} \Delta \vec{r}_i(t_\alpha) + \sum_{\beta \in M_2} \Delta \vec{r}_i(t_\beta) + \cdots \right]^2 \rangle \tag{4.5}$$

where $\Delta \vec{r}_i(t_\alpha)$ is the displacement of i-th atom due to an event of type M_1. An analogous definition is valid for $\Delta \vec{r}_i(t_\beta)$. The indexes α and β run over the set of events belonging to mechanism M_1 and M_2, respectively.

Eq.(4.5) can be further manipulated

$$\langle \Delta r^2(t) \rangle = \langle \Delta \vec{r}^2_{M_1}(t) \rangle + \langle \Delta \vec{r}^2_{M_2}(t) \rangle + \cdots + 2\langle \Delta \vec{r}_{M_1}(t) \cdot \Delta \vec{r}_{M_2}(t) \rangle + \cdots \quad (4.6)$$

where

$$\langle \Delta r^2_{M_1}(t) \rangle = \langle \frac{1}{N} \sum_{i=1}^{N} \left[\sum_{\alpha \in M_1} \Delta \vec{r}_i(t_\alpha) \right]^2 \rangle \quad (4.7)$$

and

$$\langle \Delta \vec{r}_{M_1}(t) \cdot \Delta \vec{r}_{M_2}(t) \rangle = \langle \frac{1}{N} \sum_{i=1}^{N} \sum_{\alpha \in M_1} \sum_{\beta \in M_2} \Delta \vec{r}_i(t_\alpha) \cdot \Delta \vec{r}_i(t_\beta) \rangle \quad (4.8)$$

Similar definitions are assumed for other mechanisms.

If the sample is monophasic and there are no external fields acting on it, the product $\Delta \vec{r}_{M_1}(t_\alpha) \cdot \Delta \vec{r}_{M_2}(t_\beta)$ can assume with the same probability positive and negative values. Therefore, the term $\langle \Delta \vec{r}_{M_1}(t) \cdot \Delta \vec{r}_{M_2}(t) \rangle$ becomes zero. This is the case in the performed simulations. In fact, the term $\langle \Delta \vec{r}_{M_1}(t) \cdot \Delta \vec{r}_{M_2}(t) \rangle$ is about three order of magnitude smaller than the smallest $\langle \Delta r^2_{M_\alpha}(t) \rangle$ term. Therefore, Eq.(4.6) reduces to

$$\langle \Delta r^2(t) \rangle \cong \langle \Delta r^2_{M_1}(t) \rangle + \langle \Delta r^2_{M_2}(t) \rangle + \cdots \quad (4.9)$$

Eq.(4.9) states that, under the above hypothesis, the total MSD is the sum of MSDs relative to each mechanism. Under the same hypothesis, using once again the fact that two discrete diffusive steps (even if belonging to the same mechanism) are independent, Eq.(4.7) can be further simplified into:

$$\langle \Delta r^2_{M_1}(t) \rangle \cong \frac{1}{N} \langle \sum_{i=1}^{N} \sum_{\alpha \in M_1} \Delta r^2_i(t_\alpha) \rangle \quad (4.10)$$

Also in this case the cross term $\langle \sum_i \sum_{\alpha,\alpha'} \Delta \vec{r}_i(t_\alpha) \cdot \Delta \vec{r}_i(t_{\alpha'}) \rangle$ is negligible with respect to $\langle \sum_i \sum_\alpha \Delta r^2_i(t_\alpha) \rangle$ (about three order of magnitude smaller).

Unfortunately, $\Delta r^2_i(t)$ is noisy (see top panel of Fig.(4.2)). This is due to the interplay of two phenomena: diffusive steps and atomic vibrations about equilibrium positions. The problem of the noise can be reduced by averaging the

atomic positions on a time window τ centered on the time t. The window τ needs to be larger than the period of a vibration, but not too large otherwise distinct diffusive steps can be confused. A τ of 100 fs is used in the simulations. The $\Delta r_i^2(t)$ computed on average positions is much more regular (compare Fig.(4.2/a) and Fig.(4.2/b)) and shows a clear stepwise behavior. The $\bar{\Delta r_i^2}(t_\alpha)$ to be used in Eq.(4.10) is computed by the difference of average atomic positions before and after the time t_α.

A key issue is still open, namely how to identify the times t_α, t_β, ... at which the events of type M_1, M_2, ... occur. For each mechanism, order parameters $\theta_l(\vec{r}_1(t), \cdots, \vec{r}_N(t))$ that monitor the occurrence of a diffusive step can be identified. For example, assuming that one diffusive mechanism implies the change of coordination number of a Si atom. By monitoring changes of the coordination number of each silicon the total displacement of the mechanism can be evaluated, as indicated in Eq.(4.10) (see Fig.(4.2)).

The complete description of the collective coordinates used for monitoring the mechanisms identified in this paper is given in Sec.(3.2). Anticipating the results, it is worth remarking that using this technique a set of three mechanisms accounting for more than the 90 % of the diffusivity is identified.

On the basis of the so computed MSD, we can calculate the diffusivity of each self-diffusion mechanism and, from this, the corresponding migration energy E_{M_α} and the pre-exponential factor $D_\infty^{M_\alpha}$. Of course, as for the overall E and D_∞, these are phenomenological parameters.

A somewhat related approach for the calculation of parameters governing the mass transport in crystals has been devised and applied by Da Fano and Jacucci [34]. In this approach, the frequency of events of a given type occurring in a MD run is counted and analyzed according to the following Arrhenius-type formula

$$\begin{aligned} \Gamma_{M_\alpha}(T) &= D_\infty^{M_\alpha} \exp\left(-\frac{E_{M_\alpha}}{k_B T}\right) \\ &= \nu_{M_\alpha} \exp\left(S_{M_\alpha}/k_B\right) \exp\left(-\frac{E_{M_\alpha}}{k_B T}\right) \end{aligned} \tag{4.11}$$

where $\Gamma_{M_\alpha}(T)$ is the number of events of a give type, ν_{M_α} is the corresponding attempt frequency, E_{M_α} is the migration energy and S_{M_α} is the migration entropy. In this case, Eq.(4.11), and therefore the parameters contained into it, is no longer

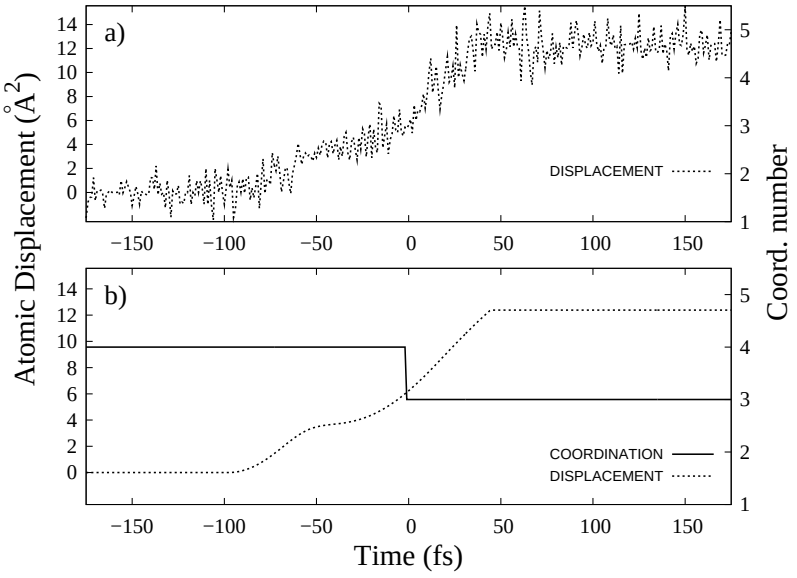

Figure 4.2: Panel a) $\Delta r_i^2(t)$ for a Si atom (dotted line) and the corresponding variation of the coordination number (continuous line). Panel b) same data after time average over a time window τ. Values are reported with respect to average values in the period plotted. The time origin in the graph is taken at the instant at which the average coordination number changes its value, i.e. the instant at which an event of this mechanism occurs.

phenomenological. Rather, it is derived from Transition State Theory in harmonic approximation.

It is worth mentioning that while the Da Fano and Jacucci method is perfectly justified in the case of crystals, where all the events of the same kind give the same contribution to the mass transport, in the case of amorphous materials the validity of this method is more questionable. In fact, depending on the environment of the atoms undergoing to a diffusive event, the corresponding displacement can vary significantly. This means that in the case of amorphous materials we must understand a diffusive mechanism in a more loose sense. However, in the following we have performed both kind of analysis and, anticipating our results, they both bring to the same qualitative conclusions.

2 Sample Preparation and Computational Setup

The stoichiometric a-SiO_2 sample was obtained by quenching from the melt. Within this approach disordered structures are generated by quenching from an equilibrated silica melt to room temperature. The procedure starts from a well equilibrated sample of fluid SiO_2 at 8500 K. The silica melt is obtained by molecular dynamic simulations at constant volume and the temperature is controlled using the Nosè-Hoover chain method [25] using a time step of 0.5 fs. The liquid sample is obtained by melting a *beta*-cristobalite sample. The density of the sample was kept fixed at the experimental density of a-SiO_2 (2.17 g/cm^3). After 25 ps at 8500 K, the high temperature liquid is cooled down to 4000 K with a rate of $4 \cdot 10^{13}$ K/s. The sample is equilibrated at 4000 K for 50 ps. Then the sample is cooled slowly down to room temperature as follows. First a run of 50 ps is performed to obtain a sample at 2000 K which is equilibrated for 25 ps. Then the sample at 2000 K is cooled again to 300 K in 100 ps and finally it is equilibrated at room temperature. In Fig.(4.3) the complete amorphization procedure is shown.

a-SiO_2 was modeled by samples of size ranging from 5184 to 24000 atoms. Three samples of different size are prepared in order to compare the results. In all cases a cubic cell of β-cristobalite are prepared. The smallest sample consists of 5184 atoms, that correspond to 1728 units of SiO_2. The cell dimension for this sample is 42.996 x 42.996 x 42.996 Å. Another sample of 12288 atoms (4096 SiO_2 units) is prepared from a cubic cell with L=57.328 Å. For the last sample, a cubic cell of 71.660 Å containing as many as 24000 atoms (8000 SiO_2 units) is used. It is worth to note that the results for the three samples are essentially the same. This means that the size of the smallest sample obtained is big enough to correctly reproduce the self diffusion of a-SiO_2. The atomic interactions are treated by means of the modified Tersoff potential developed by Billeter *et al.* [19] and described in Sec.(2).

It is important to stress that, since the cooling rate is several order of magnitude higher than the experimental one, the consistency of this computational model with the experimental samples must be carefully checked. The g(r) (see Fig.(4.4)) obtained with the above procedure is compared with previous experimental [35, 36] and *ab initio* [37] data, obtaining a very good quantitative agree-

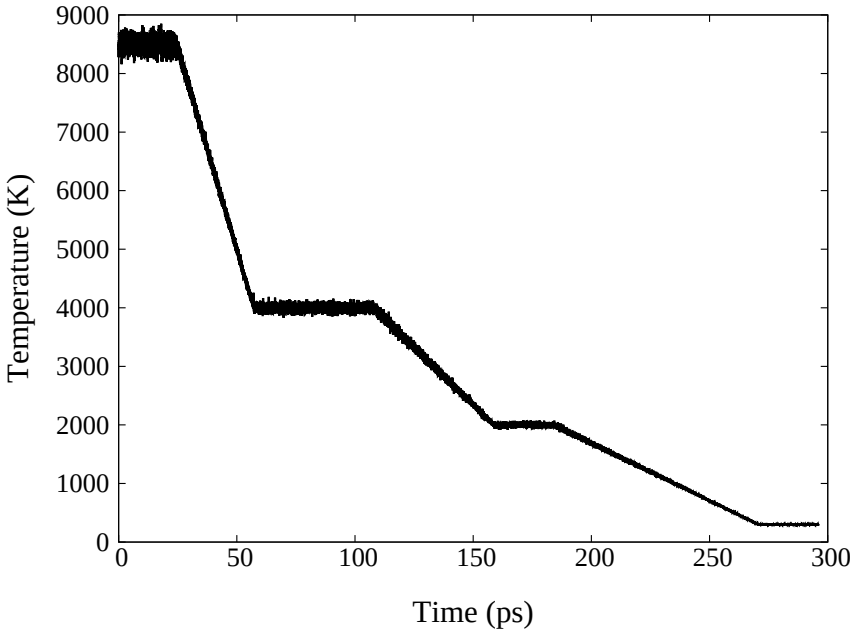

Figure 4.3: Quenching thermal cycles used for the amorphization of SiO_2.

ment.

a-SiO_2 samples at various stoichiometries (from 33 % to 45 % of Si) are obtained from the stoichiometric SiO_2 by random substitution of Oxygen atoms with Silicon atoms. After the substitution, the system was relaxed for 50 ps, with a time step of 0.5 fs, by mean of constant temperature MD using the Nosè-Hoover chain method [25]. Since the experimental density is not available, the density of these systems is fixed at the density of stoichiometric a-SiO_2. However, we verified that with this setup the internal pressure of such samples is negligible.

The self diffusion in stoichiometric and sub-stoichiometric samples of SiO_2 is investigated in a range of temperature from 1500 K to about 3000 K, depending on the concentration of Si. Total and mechanism specific MSD of Eqs.(4.3-4.6) are computed by means of MD at constant number of particles, volume and energy (NVE). Simulations at different temperatures is performed changing the total energy of the system. At each concentration and temperature, 200 ps MD simulations are run. We verified that such long simulations are adequate for reaching the linear regime of the MSD required by Eq.(4.2).

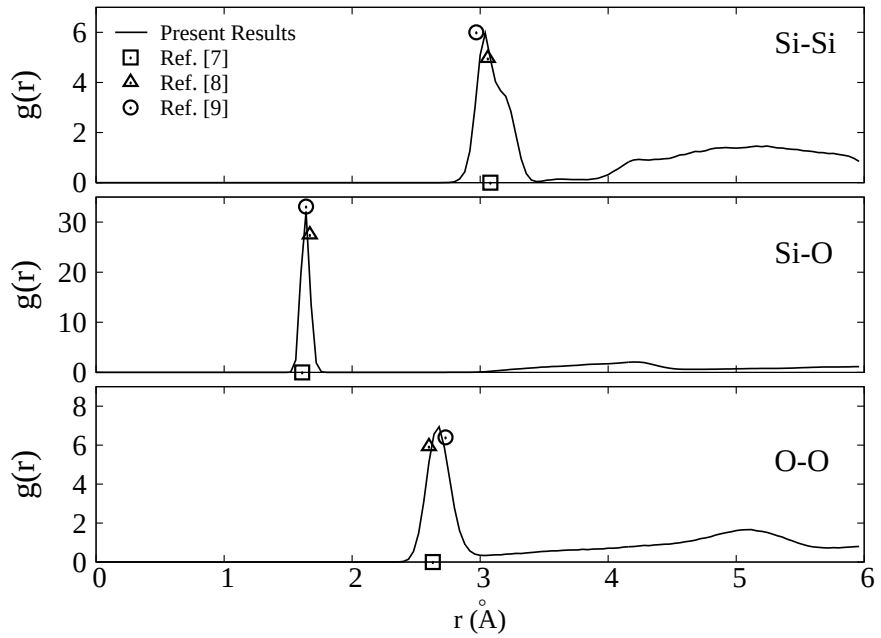

Figure 4.4: Pair correlation function of stoichiometric a-SiO_2 as obtained from the quenching from the melt procedure described in the text. Positions and, when available, magnitudes of peaks as obtained in previous experimental (Johnson et al.[35] and Susman et al.[36]) and *ab initio* MD (Sarnthein et al.[37]) works are reported for comparison.

3 Results and Discussion

3.1 Migration Energy

Fig.(4.5) shows the diffusivity of Si atoms at various temperatures and concentrations as obtained from MSD (see section 1). Corresponding data for O were computed as well but not shown in figure as there are no corresponding experimental data to compare with. It is worth noticing that we performed MD simulations in a temperature range higher than the experimental one. This is a standard method for accelerating MD simulations to study diffusivity. In particular, under the only hypothesis of an Arrhenius dependence upon temperature (a very widely and common-sense assumption, indeed) high-temperature data can safely be extrapolated down to room temperature. Of course the reliability of

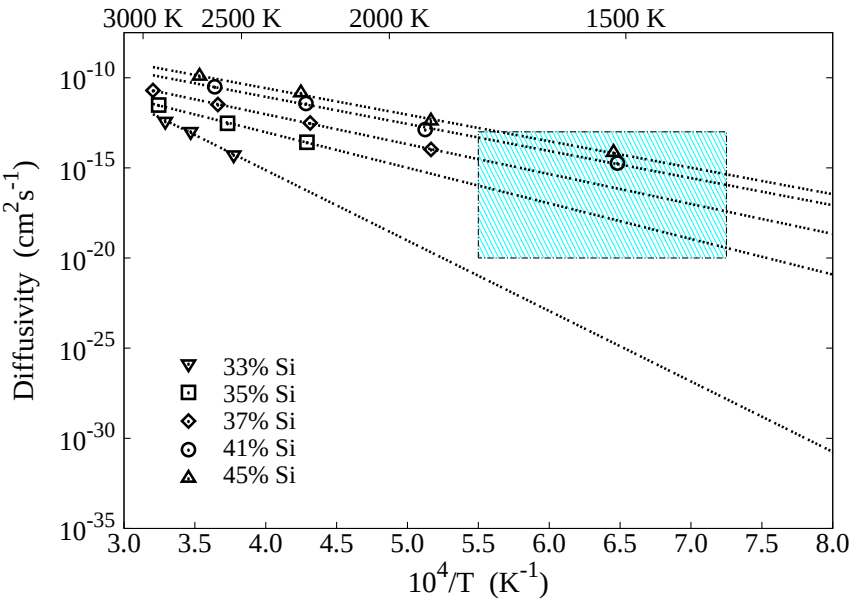

Figure 4.5: Diffusivity of Si atoms as a function of the inverse of temperature for SiO_{2-x} samples at various Si concentrations. The cyan frame in the graph represents the range of observed experimental values.

the results must be checked *a posteriori*. In the present case, we have performed two tests: (i) assessing whether the system was still in amorphous phase at the higher temperatures; (ii) assessing whether the diffusion data extracted from such a sample can be extrapolated at lower temperatures. As for (i), by analyzing the g(r) we verified that the system persisted in the amorphous phase also at the higher temperatures. This is not surprising as in simulations, especially constant volume simulations of (relatively) small samples, large fluctuations of the density are forbidden and the system can stay in a metastable state despite the fact that exists another phase at lower free energy. As for (ii), we verified that the log of diffusivity is inversely proportional to the temperature over the whole range of temperature simulated, as requested from the Arrhenius law. For sake of comparison, we also report the $D(T)$ vs T range of experimental data[38, 39, 40, 41] (the cyan box in Fig.(4.5)). It can be seen that extrapolated computational data are well within the experimental range, confirming the overall agreement of the present results with experimental data.

From Fig.(4.5) and the corresponding data for the diffusion of O, we calculated migration energies as a function of the Si concentration (see Fig.(4.6), top). For the migration energy of Si at the stoichiometric composition we found a value that is the 65-75 % of the experimental values [38, 39, 40, 41], depending on the considered experiment. These results are in line with the predictive capability of the Billeter *et al.* potential, as evaluated by the test of diffusion in α-Quartz, which is in the range of 80 % (see section 2), and the typical accuracy of diffusivity calculated by means of classical MD.

A relevant difference exists between the present simulations and the experimental setup. The experimental diffusivity is calculated by fitting the concentration distribution of radioactive Si atoms in a sample of SiO_2. The radioactive Si is provided by a sample of crystalline Si through a Si/a-SiO_2 interface. The diffusivity is therefore due to a possible two-step mechanism: i) crossing of the Si/a-SiO_2 interface, ii) diffusion in a-SiO_2. Moreover, these experiments are performed in non-equilibrium conditions. So, the experimental conditions, which are meant to study the diffusivity occurring in different kind of systems, are not directly mimicked by our simulations.

Finally, the results are in qualitative agreement with previous DFT calculations [31], which report an energy barrier of 4.5-5 eV. However, also in this case it is worth noticing some difference in the setup. In fact, the DFT calculations were carried out by guessing a diffusion path composed of several steps. The atomistic model for simulating each of these steps was indeed a cluster model, therefore elastic forces due to the condensed phase environment were neglected. Moreover, even though the authors mention that the diffusion energy changes from one initial/final site to another of the same type, results are reported only for one of them. In addition, the small size of the sample (just 24 SiO_2 units) does not allow neither the fluctuation of the (local) density nor of the (local) chemical composition of the sample. Since migration energy is affected by the concentration (see below), results might change in function of these fluctuations. Furthermore, since just one path has been tested, results of Yu et al. [31] might be strongly biased by the only mechanism actually considered.

As for the stoichiometry of the sample, Fig.(4.5) shows an increase of diffusion of Si with its concentration. This is reflected by a decrease of the migration energy E (see Fig.(4.6), top) and by an increase of the pre-exponential coefficient D_∞

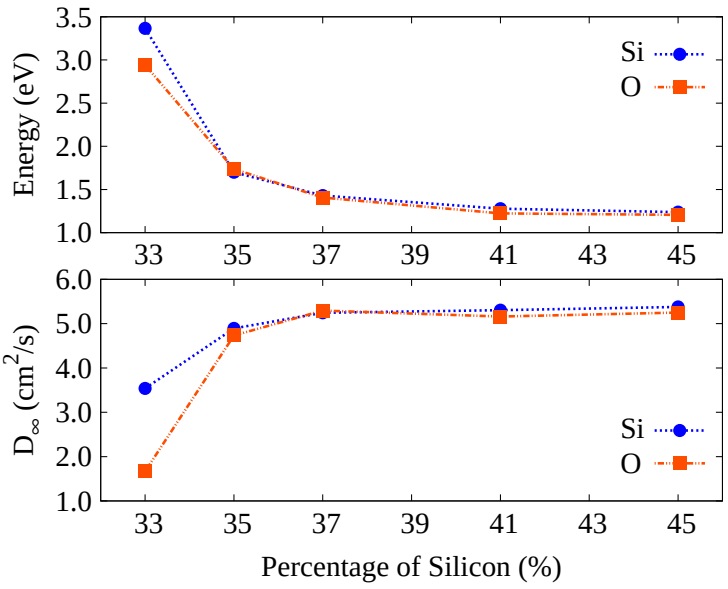

Figure 4.6: Si and O migration energy (top panel) and pre-exponential factor D_∞ (bottom panel) as a function of the Si concentration.

(see Fig.(4.6), bottom). This trend is in agreement with experimental findings [41]. It is interesting noticing that a similar trend is observed for the diffusion of O as well. This seems to suggest that the diffusion of O and Si atoms is indeed correlated.

3.2 Mechanisms

In this paragraph the diffusion mechanisms of silicon and their dependence on the stoichiometry of the sample are analyzed.

By visual inspection of the trajectories three types of stepwise mechanisms (see Sec.(1)) are identified. These types of mechanisms can be described in terms of change of coordination for Si and O atoms or swapping of a Si-Si bond for a Si-O bond (or viceversa). Please notice that, at a variance from previous papers[31], the model under consideration does not take into account the actual value of the coordination number, rather its variation. The rationale for this choice is that in amorphous samples there might exist many atoms with different coordination,

all undergoing to one of the mechanisms introduced above.

More in detail, the first mechanism consists in the change of coordination of Oxygen atoms. An example of such an event is presented in the top panel of Fig.(4.7). In this diffusive event an O atom which is initially one-fold coordinated (the blue atom labeled "O1" in the panel) recovers its complete coordination by forming a bond with a Si atom (the violet atom labeled "Si" in the panel). In order to do so, the Si atom breaks a bond with another O (the green atom labeled "O2" in the same panel) which therefore becomes one-fold coordinated. Hereafter this mechanism is called O-driven. Of course, events with O and Si atoms with different initial and final coordination, all belonging to the O-driven mechanism, occur in the simulations.

The second kind of mechanism is analogous to the first one but for that in this case Si atoms change their coordination. An example of such an event is shown in the central panel of Fig.(4.7). Here, two Si atoms are initially 3-fold coordinated (blue and green atoms labeled "Si1" and "Si2", respectively, in the panel). By forming a bond among them they change their coordination from 3 to 4, so restoring their perfect coordination. Hereafter this mechanism is called Si-driven. As above, events with O and Si atoms with different initial and final coordination, all belonging to the Si-driven mechanism, occur in the simulation.

Finally, in the third kind of mechanism a Si-Si bond is swapped for a Si-O bond (or viceversa). An example of this mechanism is presented in the bottom panel of Fig.(4.7). In this event, the green Si (labeled "Si2' and the violet O (labeled "O") are initially bonded. After the swapping the green Si atom is bonded to the blue Si (labeled "Si1"). This mechanism shall be called bond-swapping. A possible explanation of the behavior described above is the attempt of miscoordinated Si and O atoms to restore the optimal coordination (O-driven and Si-driven mechanisms) or to establish a network of chemical bonds that minimize the stress in a region of the sample (bond-swapping).

In order to implement the method described in Sec.(1) a set of collective variables able to monitor the occurrence of events of the above types is needed. For this purpose we use total and partial coordination numbers. The former counts the total number of neighbors of a given atom, while the latter takes into account also their chemical nature. Mathematically, the partial coordination number is defined as:

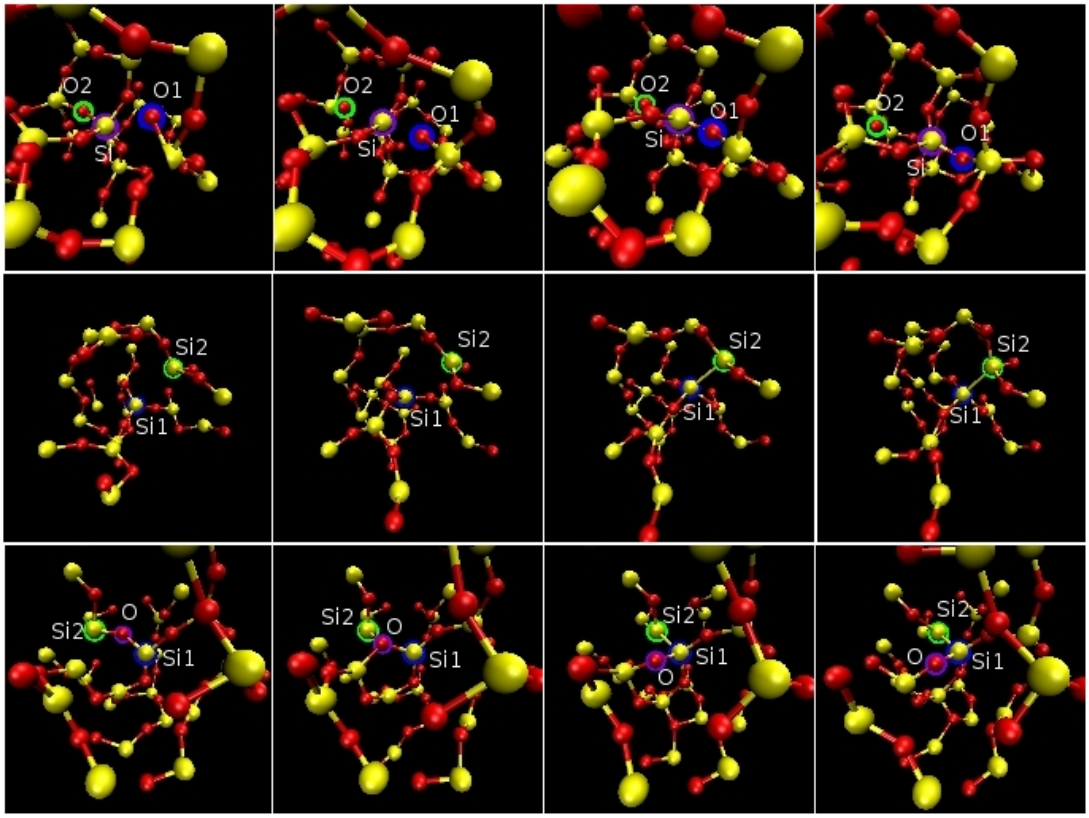

Figure 4.7: Snapshots of events belonging to the O-driven mechanism (top), Si-driven mechanism (center), and bond-swapping mechanism (bottom). The mechanisms are described in detail in the text. Atoms involved in the processes are highlighted in green, blue and violet.

$$\theta_i^B = \sum_{j \in B} \Theta(r_{ij} - r_{cut}) \tag{4.12}$$

where θ_i^B is the coordination number of the i$-th$ atom with respect to atoms of the species B, $\Theta(r - r_{cut})$ is the Heaviside step function, r_{ij} is the distance between atom i and atom j, r_{cut} is the cutoff distance beyond which two atoms are no longer considered bonded. The sum in Eq.(4.12) runs over atoms of the chemical species B. The total coordination number can be obtained from partial coordination number according to the following formula:

$$\theta_i = \sum_{B=1}^{N_{sp}} \theta_i^B \tag{4.13}$$

where the sum runs over the N_{sp} chemical species in the sample (two in the present case).

The O-driven mechanism can be monitored following the variation of the total coordination number of the O atoms (hereafter referenced by the symbol θ_O). It is worth mentioning that analyzing the partial coordination numbers we discovered that θ_O^O (number of O atoms bonded to O atoms) is always zero. This means that under the condition of the present simulations O_2 molecules are never formed. Similarly, events belonging to the Si-driven mechanism are identified by monitoring changes in the value of the total coordination of Si atoms (θ_{Si}). Finally, the partial coordination θ_{Si}^O and θ_{Si}^{Si} are used to identify events in which a Si-O bond is swapped for a Si-Si bond (or viceversa), under the constrain that the total coordination number of the atom considered is unchanged ($\Delta\theta_{Si}^O + \Delta\theta_{Si}^{Si} = 0$).

Using these collective variables, the time at which events of a given mechanism occurs can be identified. The change of collective variables θ_i^B and θ_i also indicates that the atom i (and possibly the atoms bonded to it) is involved in the diffusive step. Then, applying Eq.(4.10) on these atoms, distinguishing between Si and O, we compute the MSD displacement relative to a given mechanism and the corresponding diffusivity. The three mechanisms introduced above account for more than the 90% of the total MSD at all temperatures and Si concentrations.

From the so computed MSD the $D_{M_\alpha}(T)$ of each individual mechanism and, from this, the corresponding E_{M_α} and $D_\infty^{M_\alpha}$ can be calculated. In Fig.(4.8) are reported E_{M_α} and $D_\infty^{M_\alpha}$ at various stoichiometries. For comparison, in Fig.(4.9) are reported the corresponding data obtained through the Da Fano and Jacucci method [34]. Our calculations (Fig.(4.8), top) show that at lower Si-concentration the mechanism with the lowest migration energy is the O-driven mechanism. When the Si-concentration is increased, the activation energy of the Si-driven and bond-swapping mechanisms is reduced below that of the O-driven mechanism which, for a Si-concentration above 37%, rises. Concerning the pre-exponential factor, for Si-concentration below 39% the $D_\infty^{M_\alpha}$ of Si-driven and O-driven mechanism is about the same (see Fig.(4.8/B)). However, above this value, the $D_\infty^{M_\alpha}$ of the O-driven mechanism is largely reduced.

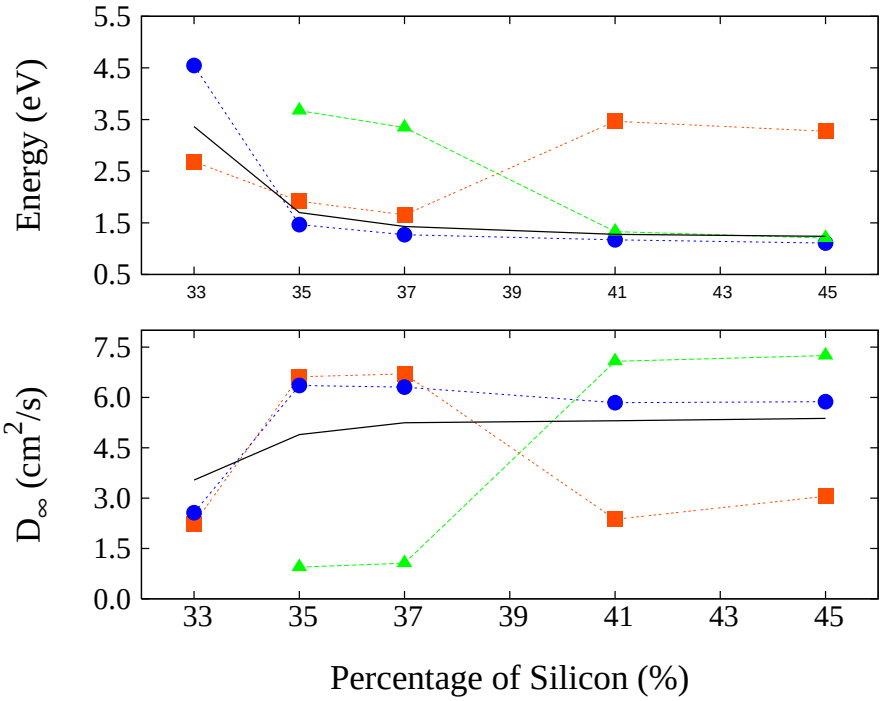

Figure 4.8: Relative contribution to the total diffusivity due to O-driven (red squares), Si-driven (blue dots), and bond-swapping (green triangles) mechanisms.

An equivalent analysis performed on the basis of Eq.(4.11) taken from Da Fano and Jacucci [34] produced results in qualitative agreement with those obtained from the MSD of each individual mechanism (see above). E_{M_α} and $D_\infty^{M_\alpha}$ obtained from Eq.(4.11) are reported in Fig.(4.9). It can be seen that, as in the case of Fig.(4.8), the migration energy of the O-driven mechanism rises for higher Si-concentration. At the same time, the migration energy of the Si-driven and bond-swapping mechanisms both decrease.

It is also interesting to determine the relevance of each mechanism with respect to the total diffusivity at the given temperature and Si concentration. In Fig.(4.10) we report the relative occurrence of the $D(T)$ due to each of the three mechanisms (hereafter referred to as $\%D(T)$) as a function of the stoichiometry of the samples at few selected temperatures. A similar trend is observed in the whole range of temperature considered in this paper ($1500 - 3000$ K). For temperature

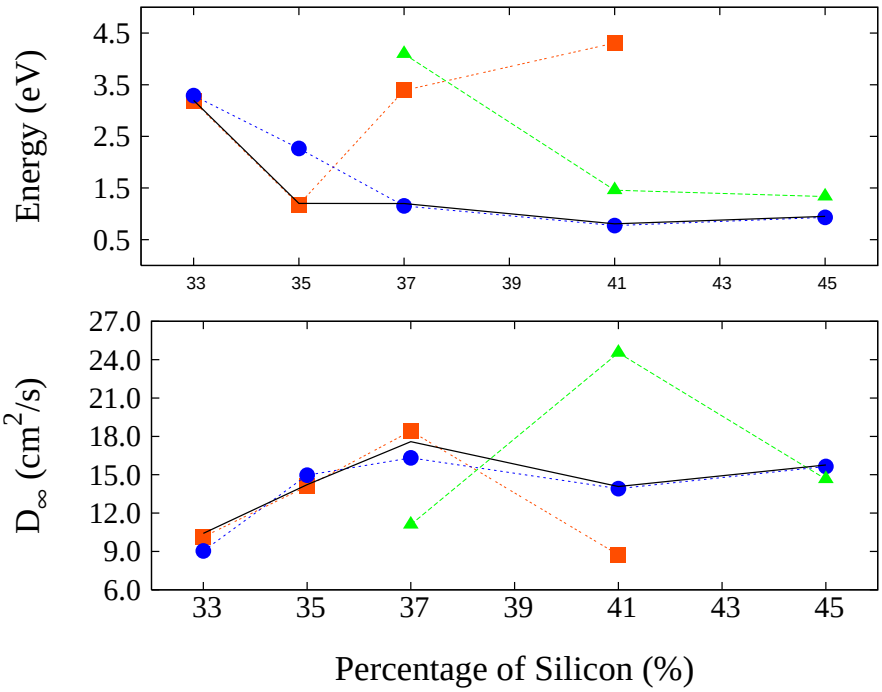

Figure 4.9: O-driven (red squares), Si-driven (blue dots), and bond-swapping (green triangles) migration energies E_{M_α} and pre-exponential factor $D_\infty^{M_\alpha}$ computed according to Ref.[34].

below 1500 K, we calculated the $\%D(T)$ on the basis of data extrapolated from the E_{M_α} and $D_\infty^{M_\alpha}$ of each mechanism, both using our method and the method of Da Fano and Jacucci. These results are shown in Fig.(4.11).

Fig.(4.10) shows that in stoichiometric conditions the O-driven mechanism is the dominating one. However, as the Si concentration increases, the Si-driven mechanism becomes the most relevant. At low temperatures ($T \leq 2300K$), already an increase of Si concentration as low as 2 % has a dramatic effect on the fraction of diffusivity due to Si and O under-coordination. At higher temperatures ($T \geq 2600$) this effect is less evident. For example, at 3000 K and a $\%\text{Si} = 35$ %, the contribution of Si-driven and O-driven mechanisms is about the same. Concerning the bond-swapping mechanism, its contribution to the diffusivity is negligible for Si concentration $< 37 - 41$ %. At higher Si concentrations

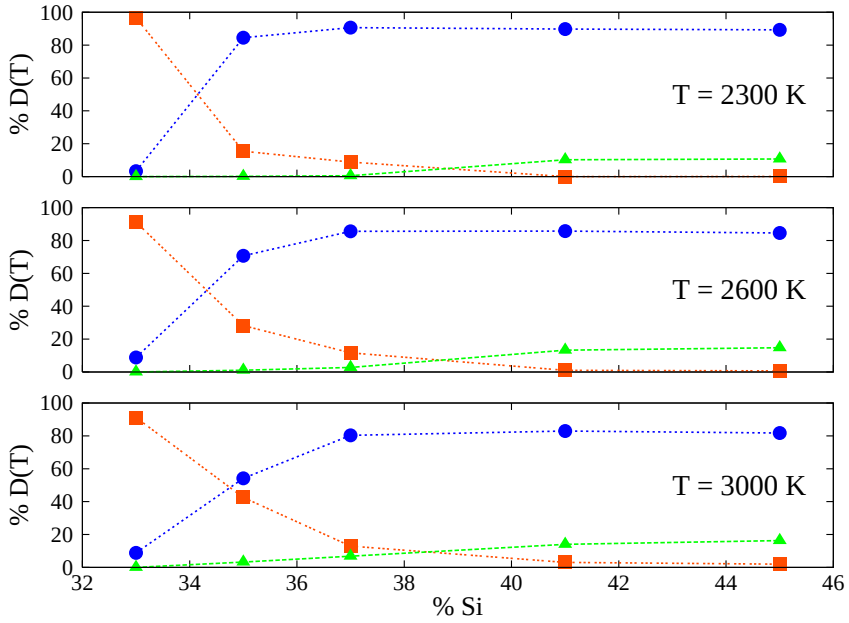

Figure 4.10: Relative contribution to the total diffusivity due to O-driven (red squares), Si-driven (blue dots), and bond-swapping (green triangles) mechanisms.

($\geq$ 41 %) it becomes active, reaching a level of contribution to the diffusivity as high as $15 - 20$ %.

Overall the above results substantiate a robust model for diffusion in stoichiometric and non-stoichiometric a-SiO_2. In systems close to stoichiometric SiO_2 (%Si $\leq$ 35 %) there is a natural abundance of Si and O coordination defects. However, while 3-fold coordinated Si atoms are rather stable one-fold coordinated O are not. Therefore, an higher number of defective O will undergoes to stepwise diffusive events aimed at restoring their perfect coordination and this causes the stepwise diffusive events observed in our simulations. Concerning the bond-swapping mechanism, it is not effective in causing the diffusivity as very few and stable Si-Si bonds are either present or can be formed at a low Si concentration.

At variance, for higher Si concentrations the overall amount of defects present in the samples, both of coordination or "local" stoichiometry nature, is higher and this increases the Si diffusivity. However, due to the overabundance of Si,

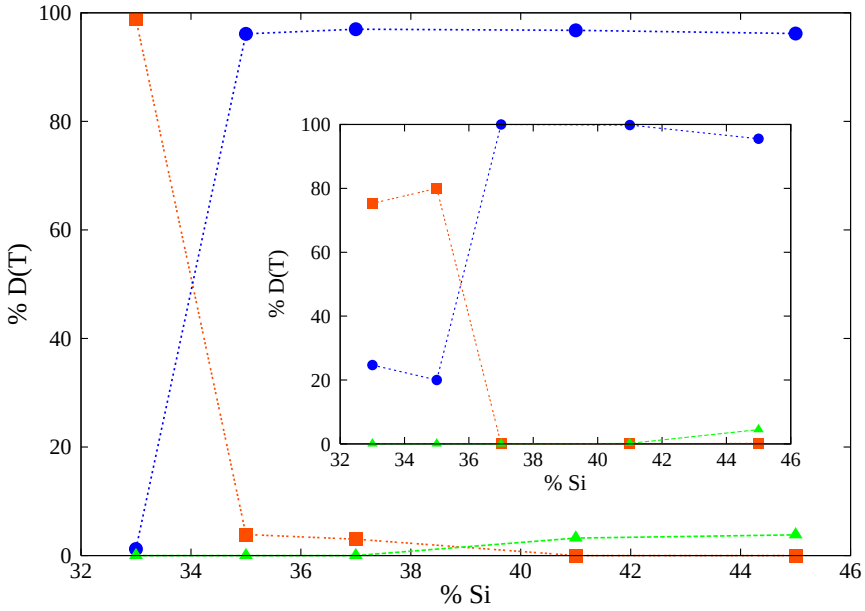

Figure 4.11: Relative contribution to the total diffusivity due to O-driven (red squares), Si-driven (blue dots), and bond-swapping (green triangles) mechanisms.

the amount of defective O atoms is reduced. This fact reduces the contribution of the corresponding mechanism to the diffusivity. On the contrary, the amount of defective Si is increased and therefore the Si-driven mechanism is more effective at these concentrations. At the same time, the concentration of Si-Si bonds is also increased which induce an increase of the diffusivity due to the bond-swapping mechanism.

Finally, as for the thermodynamical conditions, the effect of the temperature is to level the contributions of the various mechanisms to the diffusivity. This is consistent with our model as, at higher temperatures, energetically less favored defects become more abundant and therefore the corresponding mechanisms become more frequent.

Chapter 5

Amorphous-Crystal Phase Transition in Silicon Nano-particles Embedded in Amorphous SiO_2 Matrices

Nano-scale systems behave differently than ordinary bulk materials since, among other reasons, their physico-chemical properties do depend upon their size and shape. Considerable effort is ongoing to understand, design, fabricate, and manipulate materials at such a small length scale, so as to get tailored properties. In particular, the identification of how the structural features depend upon the actual thermodynamic conditions is attracting an increasing interest as it paves the way toward explaining the structure-property relationship, an issue of large technological impact. Among the nano-sized systems of technological interest, semiconductor nano-particles embedded in amorphous matrices are especially important for their possible application as photo-emitting materials for opto-electronics as well as materials for the light harvesting component of solar cells.

A feature strongly affecting the properties of nano-sized semiconductor particles is whether they are crystalline or amorphous. In particular, it has been experimentally observed that the photoluminescence intensity of Si nano-particles embedded in silica strongly depends (both in wavelength and intensity) on their crystallinity. Their structural evolution has been accordingly characterized: Si nano-particles are initially formed amorphous and then transformed into crys-

talline upon thermal annealing at high temperatures (typically at 1100°C or above) [30, 42, 43, 44, 45]. During annealing, another phenomenon has been nevertheless observed (namely the growth of nano-particles) which makes it difficult to unambiguously identify the actual atomistic mechanisms driving the observed evolution. Two models have been proposed to explain the experimental results: i) the system is always at the thermodynamic equilibrium state, but such a state could correspond to either a disordered or to an ordered atomic architecture, depending on the size of the nano-particles; ii) alternatively, the system is initially formed in the metastable disordered state, then evolving into the more stable crystalline one. In this latter case it is also assumed that the ordered phase is the most stable one for any nano-particle size (a typical bulk-like behavior), although the nano-particle is assumed to initially form in the amorphous state since this configuration is kinetically favored. Evolution towards the crystalline state is eventually observed provided that the temperature is high enough to overtake the free energy barrier separating the disordered from the ordered phase.

A fully atomistic theoretical explanation of the observed micro structure evolution of an embedded Si nano-particle is elaborated, by performing computer experiments aimed at measuring its free energy in different states of aggregation. The main output of the present investigation is that the most stable phase is identified as a function of the particle size and the thermal conditions. This result is unprecedented and valuable on its own since it was unclear whether at the nano-scale the relative stability of the ordered and disordered phase is the same as in bulk samples. We show that this result is able to explain the experimental findings on the mechanism of formation of crystalline nano-particles [46]. In addition, a fully characterization of the atomic architecture of the nano-particle is given by calculating its pair correlation function g(r) and by analyzing the Steinhardt et al. $\mathcal{Q}_6$ bond-orientational order parameter [47]. We shall demonstrate that standard theories of nucleation, such as the classical nucleation theory, are not able to model the formation mechanism of Si nano-particles in silica as the basic assumptions of these theories are violated.

1 Sample Preparation.

The sample consists of a nano-particle of pure Silicon embedded in a matrix of amorphous SiO_2. The computational samples are prepared by thermally annealing a periodically-repeated amorphous silica system, embedding Si nano-grains (extracted from a well equilibrates either amorphous or crystalline bulk).

Three systems are prepared which correspond to a nano-particle of Silicon with a radius varying in the range 1-2 nm. The computational procedure to obtain the sample is the following. First a matrix of amorphous SiO_2 of the dimension of the total system is prepared and amorphized with the quenching from the melt procedure described in the Sec.(2) Two samples of pure Silicon are also prepared for generating the nano-particles, one for the crystalline nano-particle and the other for the amorphous one. The crystalline Si sample is generated from a β-cristobalite crystal structure equilibrated at room temperature. From this sample an amorphous one is generated with the procedure described in Sec.(2). From the systems of pure Silicon a sphere with the radius of the nano-particle is taken. In the system of SiO_2 a spherical hole of the same dimension is cut out and the nano-particle of pure Si is inserted into it. Three systems with nano-particles of radius 1.0, 1.5 and 2.0 are prepared. Then, the obtained samples are first thermalized at 300 K in order to release possible stress at the Si/silica interface. Typically, during such a thermalization step, the nano-particles slightly shrinks. After this initial step, the restraint on the size of the nano-particles is imposed (see Sec.(3.1)) and the samples are thermalized at the various target temperatures. Because of the restraint on their size, at this stage neither a further shrinking nor a growing of the nano-particles are observed. After this treatment the samples are ready for the biased simulations described below. In order to verify possible artifacts due to finite-size effects, the calculation of the mean force are repeated at few selected value of $\mathcal{Q}_6^*$ (see below) on samples of different size of the silica matrix. No significant difference in the mean force is observed (the differences were within the statistical error). This demonstrates that there are no finite-size effects on our free energy calculations.

At the end of computational procedure the three systems have the following characteristic. The smallest nano-particle has a radius of 0.8 nm. It is embedded in an a-SiO_2 cubic matrix of about 43 Å of cell dimension. The total system

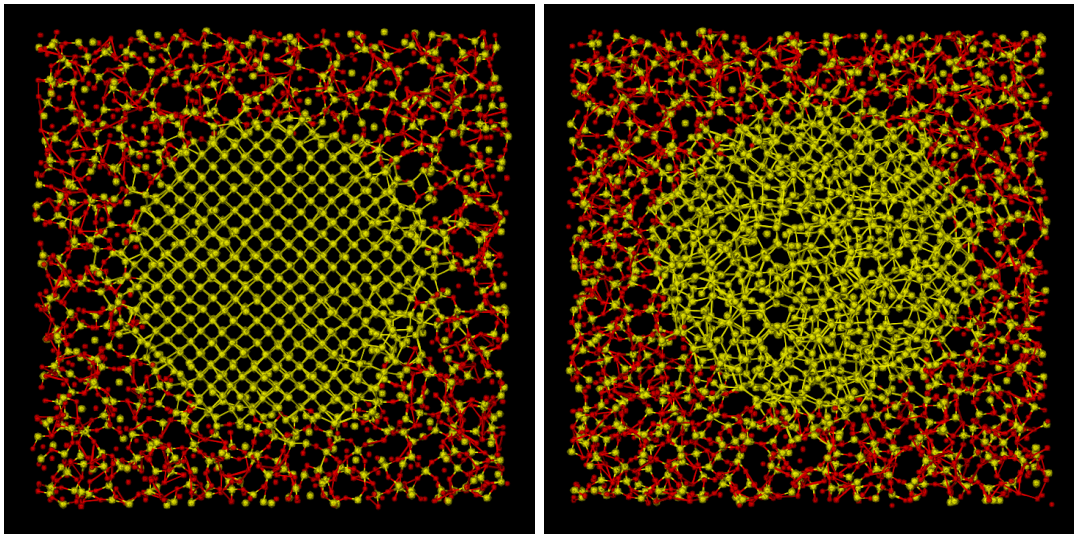

Figure 5.1: Section of the system of Si nano-particle, with radius of 1.3 nm, embedded in a matrix of SiO_2. In the left panel is reported the section of a crystal nano-particle, while on the right is shown the same section in the case of an amorphous nano-particle.

contains as many as 5109 particles. The other two nano-particles are inserted into a a-SiO_2 sample of $\sim$ 57 Å in size. At the end of the computational procedure the Si nano-particles have a radius of 1.3 nm and 1.8 nm. The total number of atoms is 12080 for the former system and 11788 for the latter.

In Fig.(5.1) a section of the total system is reported both for the crystal (left panel) and for the amorphous nano-particle (right panel) in the case of the nano-particle of radius 1.3 nm. It is quite clear the presence of order in the case of the crystal nano-particle in contrast with the random disposition of the atoms in the case of amorphous nano-particle.

In Fig.(5.2) are reported the pair correlation function (top panel) and the angular distribution (bottom panel) only of the atoms belonging to the nano-particle. The data are relative to the nano-particle with a radius of 1.3 nm after the thermalization at 300 K. The position of the first peak in the g(r) is the same for the two phases. On the other hand the intensities are different. Moreover, the g(r) of the crystalline phase shows a long range order which is absent in the amorphous one. Indeed, the amorphous sample has only one broad peak at

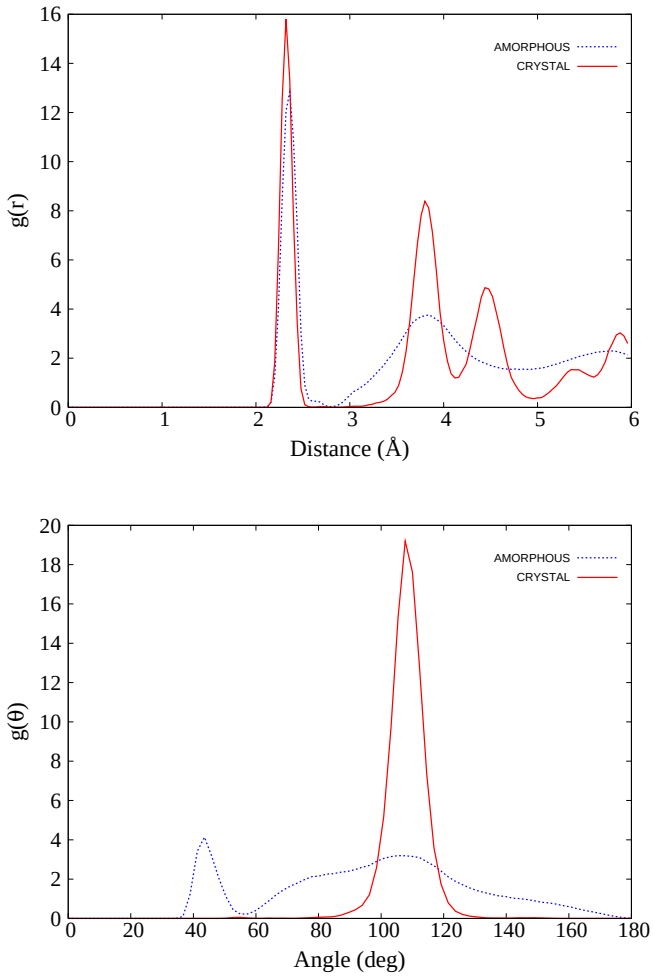

Figure 5.2: Pair radial distribution functions (top) and angle distributions (bottom) for the two nano-particles obtained with the computational procedure described in Sec.(1).

about 4 Å while the crystal sample shows several peaks between 3 and 6 Å. The differences in the g(θ) are more evident. The crystal structure has a narrow peak around 110° degrees relative to the tetrahedral disposition of the atoms in the β-cristobalite structure geometry. While the amorphous shows a more broad and less intensive peak in the same position and a new peak around 40° degrees.

2 Free Energy Calculations

For measuring the degree of order of the Si nano-particle I use the Steinhardt *et al.* [47] bond orientational order parameter $\mathcal{Q}_6$. The $\mathcal{Q}_6$ is described in detail in Sec.(3.2). Anticipating the conclusion of Sec.(3.2), for a disordered Si nano-particle $\mathcal{Q}_6$ is small (still not exactly zero due to finite size effects). On the contrary, in a crystalline object $\mathcal{Q}_6$ is much larger, and its actual value depends on the size. The free energy of nano-particles at different level of order are calculated according to this parameter.

The free energy of the system in the space of the collective variables $\mathcal{Q}_6$ is given by

$$\mathcal{F}(\mathcal{Q}_6^*) = -\, k_B T\, \ln \frac{\int dx\; e^{-\beta\, V(x)}\; \delta(\mathcal{Q}_6(x) - \mathcal{Q}_6^*)}{\int dx\; e^{-\beta\, V(x)}} \tag{5.1}$$

here $V(x)$ is the physical potential (see Sec.(2)) $\mathcal{Q}_6(x)$ is the collective variable which depends only on the position of the atoms and not on their momenta, $\mathcal{Q}_6^*$ is a particular value of the collective variable, T is the temperature and k_B is the Boltzmann constant.

The Eq.(5.1) is the free energy of a system in the state in which $\mathcal{Q}_6(x) = \mathcal{Q}_6^*$. Indeed, the ratio in Eq.(5.1) "counts" the number of configurations of the system associated to a given value $\mathcal{Q}_6^*$ of the collective variable. This means that the probability $P(\mathcal{Q}_6^*)$ of the macro-state $\mathcal{Q}_6(x) = \mathcal{Q}_6^*$ is given by

$$P(\mathcal{Q}_6^*) = e^{-\beta \mathcal{F}(\mathcal{Q}_6^*)}. \tag{5.2}$$

In principle, the probability density function of Eq.(5.2) can be computed running a molecular dynamic simulation and counting the number of times that

the system is found with a value of $\mathcal{Q}_6(x) = \mathcal{Q}_6^*$. The only requirement is that the simulation samples a canonical ensemble. Then monitoring the value of $\mathcal{Q}_6(x(t))$ the probability density can be obtained building a histogram of the value of $\mathcal{Q}_6(x)$ along the simulated trajectory. With the Eq.(5.2) one can estimate the value of the free energy as a function of $\mathcal{Q}_6$ from the probability density function.

Unfortunately, if the free energy barrier that separates the meta-stable states is higher than the thermal energy of the system, the accurate estimate of the histogram of the probability density become impossible in practice. In fact, the characteristic time for jumping between two meta-stable states separated by a barrier ΔF is proportional to $e^{\beta \Delta F}$ and when $\Delta F \gg \beta$ this time largely exceed the maximum duration of MD simulations, or the equivalent number of steps of Montecarlo simulations. Thus, the system can be trapped in one of this metastable state for all the duration of the simulation. As a consequence, the MD trajectory is not ergodic and the construction of the histogram of the probability density is impossible. This kind of situation is called a rare events; in the sense that this events are observed with a low frequency.

Unfortunately this is the case of the process under investigation. Indeed, starting from each of the two states obtained with the procedure described in the Sec.(1) the system remains for all the duration of the simulation in the initial state. The transition from one state to another is never observed in an unbiased simulation governed only by the physical potential developed by Billeter *et al.* [19] and described in Sec.(2).

A possibility to solve this problem is to perform a biasing simulation in order to drive the molecular dynamic. In this case, the method derived from the temperature accelerated MD of Maragliano and Vanden-Eijnden [12] is used. We introduce a biasing potential of the form

$$U_k(x) = \frac{1}{2}\, k\, (\mathcal{Q}_6(x) - \mathcal{Q}_6^*)^2 \tag{5.3}$$

where the parameter k determines the degree of biasing of the simulation (for $k = 0$ the MD simulation is unbiased) and $\mathcal{Q}_6^*$ is a given value of the collective variable $\mathcal{Q}_6(x)$. In the present investigation, the biased MD is governed by the superposition of the physical potential (namely the Billeter *et al.* [19, 20] environment-dependent force field described in Sec.(2)) and the biasing potential. As a consequence of the introduction of the biasing potential, a new dynamics is

defined, where the force is given not only by the gradient of the physical potential but also by the derivatives of the collective variable. This leads to the following expression for the time evolution of the i-th atom

$$\dot{p_i} = -\frac{\partial V(x)}{\partial x_i} + k\left(\mathcal{Q}_6^* - \mathcal{Q}_6(x)\right)\frac{\partial \mathcal{Q}_6(x)}{\partial x_i} \tag{5.4}$$

The new expression for the free energy with the biasing potential is given by

$$\mathcal{F}_k(\mathcal{Q}_6^*) = -\,k_B\,T\;\ln\frac{\int dx\; e^{-\beta\,\left(V(x)+U_k(x)\right)}}{\int dx\; e^{-\beta\,V(x)}} \tag{5.5}$$

In the limit of large k $e^{-\beta U_k(x)}$ goes into $\delta(\mathcal{Q}_6(x)-\mathcal{Q}_6^*)$ and the $\mathcal{F}_k(\mathcal{Q}_6^*)$ is the free energy of the system at the temperature T. Unfortunately, due to the presence of meta-stabilities the denominator in the logarithm of Eq.(5.5), and therefore the entire formulas cannot be computed directly from MD. However, Maragliano and Vanden-Eijnden in Ref.[12] demonstrate that the derivative of the free energy can be obtained from a MD simulation. Indeed, an approximation to the derivative of the free energy with respect the $\mathcal{Q}_6(x)$ (hereafter referred to as "mean force") is given by

$$\frac{\partial \mathcal{F}_k(\mathcal{Q}_6^*)}{\partial \mathcal{Q}_6^*} \xrightarrow{\beta\,k\to\infty} \frac{\int dx\; e^{-\beta\,\left(V(x)+U_k(x)\right)}\; k(\mathcal{Q}_6(x)-\mathcal{Q}_6^*)}{\int dx\; e^{-\beta\,\left(V(x)+U_k(x)\right)}} \tag{5.6}$$

And in the limit of $\beta k \to \infty$ (in practice large k)

$$\lim_{\beta\,k\to\infty}\frac{\partial \mathcal{F}_k(\mathcal{Q}_6^*)}{\partial \mathcal{Q}_6^*} = \frac{\partial \mathcal{F}(\mathcal{Q}_6^*)}{\partial \mathcal{Q}_6^*} \tag{5.7}$$

where $\mathcal{F}(\mathcal{Q}_6^*)$ is the free energy of the system in the state $\mathcal{Q}_6(x) = \mathcal{Q}_6^*$. As a consequence, one can use MD to estimate the integral in Eq.(5.6). This integral gives, in the proper regime, the derivative of $\mathcal{F}(\mathcal{Q}_6^*)$ as a function of $\mathcal{Q}_6(x)$ (see Eq.(5.7)) from which the free energy of the system can be obtained by integration over $\mathcal{Q}_6^*$ (thermodynamic integration). of the free energy with respect the $\mathcal{Q}_6(x)$ is performed. Assuming ergodicity apart for $\mathcal{Q}_6(x)$, the mean force is computed according to the expression

$$\frac{\partial \mathcal{F}_k(\mathcal{Q}_6^*)}{\partial \mathcal{Q}_6^*} = \frac{1}{\tau}\int_0^\tau dt\; k(\mathcal{Q}_6(x(t)) - \mathcal{Q}_6^*) \tag{5.8}$$

where $x(t)$ is the all-atom configuration at the time t along a biased molecular dynamics trajectory generated at temperature T, and τ is the duration of the MD simulation. Please note that the k in this expression is the same as in Eq.(5.4).

The above computational device holds valid for a bulk system. However, the aim of the present study is to investigate possible order-disorder transitions at a given (i.e. fixed) nano-particle dimension. Therefore, the above procedure is modified by introducing the notion of size through the collective coordinate $\mathcal{R}(x)$, defined as the distance between the center r_c of the nano-particle (a point kept fixed during the simulations) and the closest oxygen atom, i.e. $\mathcal{R}(x) = \min|r_c - r_i^O|$, where r_i^O is the coordinate of the i-th oxygen atom. The biased MD described above is therefore further extended by introducing a second biasing potential given by

$$U'_{k'}(x) = \frac{1}{2}\, k'\, (\mathcal{R}(x) - \mathcal{R}^*)^2 \tag{5.9}$$

here k' is a parameter that control the biasing only on the size of the nano-particle. The k' parameter could be different from the k parameter of the biasing potential of the $\mathcal{Q}_6(x)$ of the Eq.(5.3). The integral given in Eq.(5.8) is therefore calculated along a biased MD in which $\mathcal{Q}_6(x)$ and $\mathcal{R}(x)$ are both restrained. Moreover an advantage can be taken of this second collective coordinate to identify the Si atoms belonging to the nano-particle to be used in the calculation of the $\mathcal{Q}_6(x)$ collective coordinate (see Sec.(3.2)). These atoms satisfy the condition $|r_c - r_i^{Si}| < \mathcal{R}^* - l$, where l is a parameter introduced to exclude the atoms at the frontier with the silica matrix ($l = 2.3$ Å in the present calculations). By MD simulations biased both on $\mathcal{Q}_6(x)$ and $\mathcal{R}(x)$, $\partial\mathcal{F}(\mathcal{Q}_6(x);\mathcal{R}^*)/\partial\mathcal{Q}_6(x)$ has been computed at several values of $\mathcal{R}^*$, keeping $\mathcal{R}^*$ fixed. By numerically integrating the $\partial\mathcal{F}(\mathcal{Q}_6(x);\mathcal{R}^*)/\partial\mathcal{Q}_6(x)$ over $\mathcal{Q}_6^*$ the free energy at given size of the nano-particle $\mathcal{R}^*$ can be obtained.

3 Collective Variables

3.1 Size of the Nano-particles

The second biasing potential of Eq.(5.9) gives rise to additional contributions to the interatomic forces which, unfortunately, cannot be straightforwardly evaluated since $\mathcal{R}(x) = \min |r_c - r_i^O|$ is a non-analytical function of x (and, therefore, there is no way to proceed through the direct calculation of $\nabla\mathcal{R}(x)$). However, we were able to approximate $\mathcal{R}(x)$ by a smooth analytical function and to perform biased MD runs according to this representation of $\mathcal{R}(x)$.

The smooth analytical approximation to the $\mathcal{R}(x)$ is obtained in two steps: i) first obtaining an analytic and explicit expression of $\min |r_c - r_i^O|$ as a function of the positions r_i^O of an Oxygen atom, where r_c is the vector of the center of the nano-particle, ii) then introducing a smooth approximation to this expression. The first step consists in recognizing the following identity:

$$\min_i |r_c - r_i^O| \equiv \sum_{i=1}^{N_i} |r_c - r_i^O| \prod_{j\neq i}^{N_i} H(|r_c - r_j^O| - |r_c - r_i^O|) \tag{5.10}$$

where N_i is the number of Oxygen atoms and $H(x)$ is the Heaviside step function, that is a function such that

$$H(x) = \begin{cases} 0 & \text{if x} < 0 \\ 1 & \text{if x} \geq 0. \end{cases} \tag{5.11}$$

If k is the Oxygen atom closest to the center of the nano-particle, then

$$\prod_{j\neq i}^{N_i} H(|r_c - r_j^O| - |r_c - r_i^O|) = \delta_{ik} \tag{5.12}$$

where δ_{ik} is the Kronecker symbol. Thus, the product is 1 if and only if the atom i is the closet Oxygen atom k to the center of the nano-particle and it is 0 otherwise. In Fig.5.3 has been reported the Heaviside step function of a generic element of the product in Eq.5.10. It is evident that if the i-th atom is not the closet atom to the center of the nano-particle there will be at least one Oxygen atom j for which $r_{ic} > r_{jc}$ therefore the product of Eq.5.10 will be zero. The only term different from zero in the sum is the one relative to the Oxygen atom closest

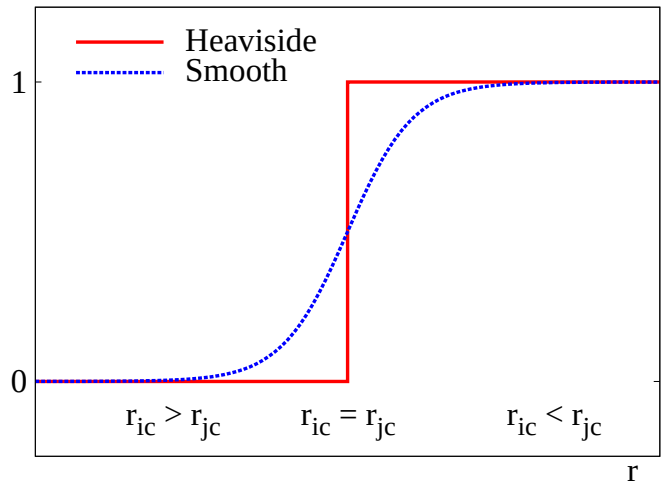

Figure 5.3: Heaviside step function and the corresponding smoothed function. Generic contribution of a term in the product of Eq.(5.10). If the i-th atom is the closest Oxygen atom to the center of the nano-particle for all the other atoms $r_{ic} < r_{jc}$ and the corresponding Heaviside function is unitary. While if the atom i is not the closest there is almost one j atom for which $r_{ic} > r_{jc}$ and the Heaviside step function is zero. The smoothed version of the Heaviside step function is reported with the dashed line.

to r_c, for which every Oxygen atom j will satisfy $r_{ic} < r_{jc}$. In this case the product will be unitary (see Fig.5.3) and the only distance $|r_c - r_i^O|$ that "survives" is the one of the closet Oxygen atom. Eq.(5.10) is therefore the definition of the particle size.

The analytical expression for the collective variable of Eq.5.10 is not useful in a molecular dynamic simulation because it leads to an impulsive dynamic. In order to avoid this drawback a smooth approximation to $\mathcal{R}(x)$ has to be used. It can be obtained by replacing the Heaviside step function by a sigmoid function (see Fig.5.3). In this case, the sigmoid function is expressed in term of the Fermi function:

$$\mathcal{S}(x; x_0, \lambda) = 1 - \frac{1}{1 + \exp^{\lambda(x - x_0)}} \tag{5.13}$$

where λ is the parameter controlling the smoothness of the Fermi function and x_0 is the center of the function. In the present case $x_0 = \mathcal{R}^*$ In the simulations λ has been chosen such that the sigmoid function goes from 0.95 to 0.05 in one atomic layer ($\approx$ 2 Å). In Fig.5.4 is reported a schematic representation of the nano-particle. In the figure r_c is the center of the particle and r_i and r_j are two generic Oxygen atoms, where the atom i is the closest to the center. The continuous line passing through r_i represents the value of the radius of the nano-particle obtained from Eq.5.10 with the use of the Heaviside step function. The use of the Heaviside function implies that every Oxygen atom that is distant more than the atom i has a zero contribute to the radius. While using a smoothed version of the Heaviside function every atom inside a shell around the atom i contributes to the radius of the nano-particle. The contribution of these atoms is weighted by the value of the sigmoid function at the point corresponding to their position. A consequence of this is that the size of the nano-particle is now defined as a weighted average of the distance of one atomic layer of oxygen atoms from the center of the nano-particle (see Fig.5.4).

The collective variable $\mathcal{R}(x)$ has to be modified in order to take in account the fact that more than one Oxygen atom can be found in the spherical region around the radius of the nano-particle. The new and final functional form of the collective variable is given by:

$$\mathcal{R}(x) = \frac{\sum_{i=1}^{N_i} |r_c - r_i^O| \prod_{j \neq i}^{N_i} \mathcal{S}(|r_c - r_j^O| - |r_c - r_i^O|)}{\sum_{i=1}^{N_i} \prod_{j \neq i}^{N_i} \mathcal{S}(|r_c - r_j^O| - |r_c - r_i^O|)} \tag{5.14}$$

where $\mathcal{S}(x)$ is the smoothed function of the Heaviside step function. It is worth to note that the smoothed version of Eq.5.10 is normalized for the number of Oxygen atoms found in the spherical shell around the radius of the particle, in order to include in the correct way the situation of multi-contribution of the Oxygen atoms.

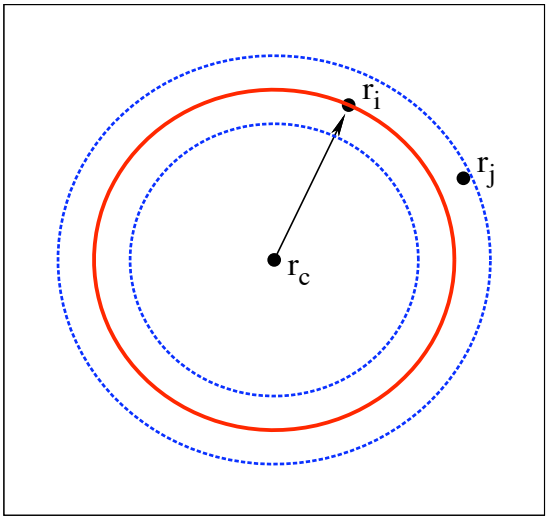

Figure 5.4: Schematic representation of the nano-particle. r_c is the center of the nano-particle, r_i is the closet Oxygen atom to r_c and r_j is another Oxygen atom. Using the analytical functional form of $\mathcal{R}(x)$ of Eq.(5.10) the radius of the nano-particle is the continuous line passing for r_i. The contribution relative to r_j in the Eq.(5.10) is zero. While using the Eq.(5.14) all the atoms inside the dashed line, i.e. r_j in the figure, contribute to the $\mathcal{R}(x)$.

3.2 Bond Order Parameter

As explained in Sec.(2), in order to compute the free energy an order parameter that is sensitive to the overall degree of crystallinity of the system is needed. The crucial point of the procedure explained in Sec.(2) is the choice of the collective variables.

A good order parameter should satisfy certain requirements. The principal characteristics are the following. i) It must not only distinguish between a crystal phase and a disordered phase but it must also quantitatively measure the degree of order of the system; ii) It does not favour one crystal structure over all the others; iii) The value of the order parameter should be rotational invariant, so it should be independent on the orientation of the crystal on the space; iv) Moreover the order parameter should be suitable for constrained molecular dynamics; v) Finally a good parameter should be easy to calculate.

The distinction between a crystal and a liquid, or more in general a disordered

phase, is that the former has two distinct types of order that do not exist in the latter. Indeed, in the crystal phase there are both translational and rotational symmetries. Instead, in a liquid or amorphous phase, the particle are disposed in a random arrangement which does not exhibit neither translational nor rotational symmetry.

Different methods have been proposed in order to quantify the degree of order in a system. The principal characteristic of a solid is that the positions of the particles are repeated periodically in the three dimensions of the space. A typical measure of this order is the structure factor S(k). This corresponds in real space to the pair distribution function (g(r)) and the angle distribution function (g(θ)). In the top panel of Fig.(5.2) are reported the g(r) of the amorphous and crystal phase of the Silicon nano-particle. The shape of the curves is very different for the two phases. A clear evidence of the presence of order can obtained comparing the pair correlation function of the two phases. Another order parameter could be obtained analyzing the Voronoi tessellation of the space [48, 49, 50, 51]. In order to analyze the structure of the system a Voronoi signature is obtained from the Voronoi tessellation of the space. In a Voronoi tessellation the Voronoi polyhedra are used. A Voronoi polyhedron associated with a given atom is defined as the part of space containing the set of points that are closer to the given atom than any other atom in the system. The Voronoi signature consists in a string of numbers that shows the number of triangular, square, pentagonal, etc. faces of the Voronoi polyhedra. For example the Voronoi signature of a body center cubic cell is (0608), because the Voronoi polyhedra consist of 0 triangular, 6 squared, 0 pentagonal and 8 hexagonal faces. There are also oder parameter that quantify the order analyzing the translational or rotational properties of the system. A typical example of these parameters is the one developed by Torquato *et al.* [52] which is a translational order parameter. In order to quantify the affinity to a tetrahedral structure a parameter is obtained from the distribution of cosines [53, 54]. The functional form of this parameter is $(\cos(\theta) + 1/3)$, where θ is the bond angle[54].

Although the order parameters listed above are able to discriminate between an ordered and a disordered phases, i.e. the first requirement, they do not satisfy all the other requirements. The structure factor is not a "good" order parameter because it is dependent on the type of the crystal. Indeed the structure factor is a

function of the wave vector k which is a basis vector in the reciprocal lattice that is relate to the crystal lattice under consideration. In this sense the structure factor does not satisfy the second requirement. The Voronoi signatures are very sensitive to the thermal fluctuations. Indeed a thermal vibration of the particles around their lattice positions can significantly modify the Voronoi signature of a crystal structure. This drawback leads to a distribution of Voronoi signature for a given structure rather than a single signature. Moreover different crystal structures have very different Voronoi signature. While is useful an order parameter which has a similar value for every crystal structure and a very different value for the disordered phase. In the best condition the value for the crystals should be large and the parameter should be vanishing for the disordered phase. Therefore a quantitative measure of the order of the system is not simple to achieve with the Voronoi signature. The g(r) and g(θ) are not good order parameters because they are vectorial variables and therefore not suitable for driving a molecular dynamics. The translational order parameters are not rotationally invariant and so they does not satisfy the third requirement of a "good" parameters. Finally the tetrahedral order parameters favour only one crystal structure, the tetrahedral precisely, over all the others.

A good starting point to develop an order parameter that satisfy all the characteristic described above is to focus the attention on the orientation of the bonds of the system. A key feature of a crystal is the positional ordering of the atoms, in the sense that any particle is surrounded by other ones in a certain preferred direction. A good measure of the crystallinity should be the bond order of the system. A bond order parameter is a quantitative measure of this preferred orientation. As a consequence it should assume a certain value for a crystal phase and on the contrary it should be zero for a disordered phase where there is the lack of the preferred orientation.

A good choice is to use of the bond order parameter developed by Steinhardt *et al.* [47] used by other authors with good results especially in the field of nucleation of Lennard-Jones liquids [55, 56, 57, 58].

The procedure for obtaining the bond order parameter is the following. First the neighbours of an atom are identified by introducing a distance cutoff. The value of the cutoff radius is set to the distance of the first minimum of the radial partial distribution functions. In this way only the first coordination shell is taken

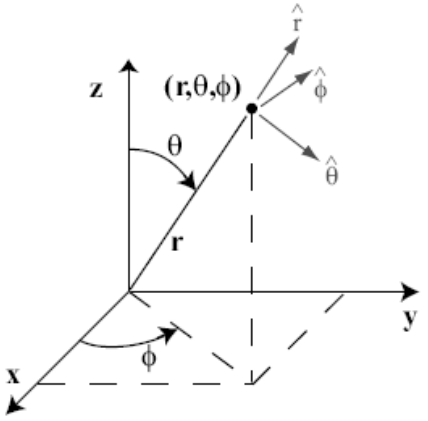

Figure 5.5: Spherical coordinates (r, θ, ϕ) in a Cartesian reference frame. The orientation of a vector $\vec{r}$ is defined by the polar angle θ and the azimuthal angle ϕ.

in account (i.e. chemical bonded atoms). In the present case, for the Silicon atom a cutoff radius of 2.8 Å is set in the case of the Si-Si distance and otherwise a value of 1.5 Å is set in the case of the Si-O pair. Once identified the neighbours, a bond is defined as the vector $\vec{r}$ connecting two atom. The unit vector $\hat{r}$ specifies the orientation of this bond. In a given arbitrary frame (see Fig.(5.5)) the orientation of the unit vector $\hat{r}$ is uniquely specified by the couple of angles θ and ϕ that correspond to the polar and the azimuthal angles, respectively. We want to define a measure of the coherence of the orientation of the bonds formed by the atoms belonging to the sample. In a crystal this coherence is high, in a liquid is low. In order to achieve this objective for each bond r_{ij} formed by the atom i the value of the spherical harmonic $\mathcal{Y}_{\ell m}(\theta(\hat{r}), \phi(\hat{r}))$ of degree ℓ and component m is computed From them, a local order parameter $q^{(i)}_{\ell m}(r_{ij})$, associated to a given atom i, can be defined summing over all contributions of the values of the spherical harmonics of the neighbours and normalizing for the number of neighbours. This leads to the following relation

$$q_{\ell m}^{(i)}(r_{ij}) = \frac{1}{M_i} \sum_{j=1}^{M_i} \mathcal{Y}_{\ell m}(r_{ij}) \tag{5.15}$$

where the sum runs over the number of neighbours M_i of the atom i. This order parameter is able to characterize a local structure around a given particle. It is worth to note that this parameter depends only on the orientation of the bonds around a certain atom and not on the distance of the bond.

Then a global order parameter $\mathcal{Q}_{\ell m}(r_{ij})$ can be defined summing the $q_{\ell m}^{(i)}(r_{ij})$ of every atom, this leads to

$$\mathcal{Q}_{\ell m}(r_{ij}) = \frac{\sum_{i=1}^{N} M_i \, q_{\ell m}^{(i)}(r_{ij})}{\sum_{i=1}^{N} M_i}. \tag{5.16}$$

However the global order parameter $\mathcal{Q}_{\ell m}(r_{ij})$ depends on the reference frame. Indeed the spherical harmonics $\mathcal{Y}_{\ell m}(\theta, \phi)$ form a $(2\ell{+}1)$-dimensional representation of the rotational group SO(3). As a consequence a rotation of the frame shuffle the spherical harmonics. In order to eliminate this drawback, an associated rotationally invariant property can be defined as follows

$$\mathcal{Q}_\ell = \left(\frac{4\pi}{2\,\ell + 1} \sum_{m=-\ell}^{\ell} |\mathcal{Q}_{\ell m}(r_{ij})|^2 \right)^{\frac{1}{2}}. \tag{5.17}$$

The $\mathcal{Q}_\ell$ is able to quantify the order in a system. Indeed, when the system is crystalline and the temperature is 0 K the environment of all the atoms is the same and therefore $\mathcal{Q}_\ell$ are maxima as there is not interference among the $q_{\ell m}^{(i)}(r_{ij})$. In other words, every atom has the neighbours in the same orientation and all the contribution of the spherical harmonics is in phase. On the contrary, in a perfectly disordered system the orientation of bonds is random and therefore there is complete destructive interference among the $q_{\ell m}^{(i)}(r_{ij})$, and $\mathcal{Q}_\ell$ is zero. Indeed in a disordered phase there is only a local orientational order which decay rapidly, so the global bond order parameter is small.

Only the spherical harmonics of a certain ℓ are suitable as order parameters. In particular, only the spherical harmonics with even ℓ order are used. As spherical

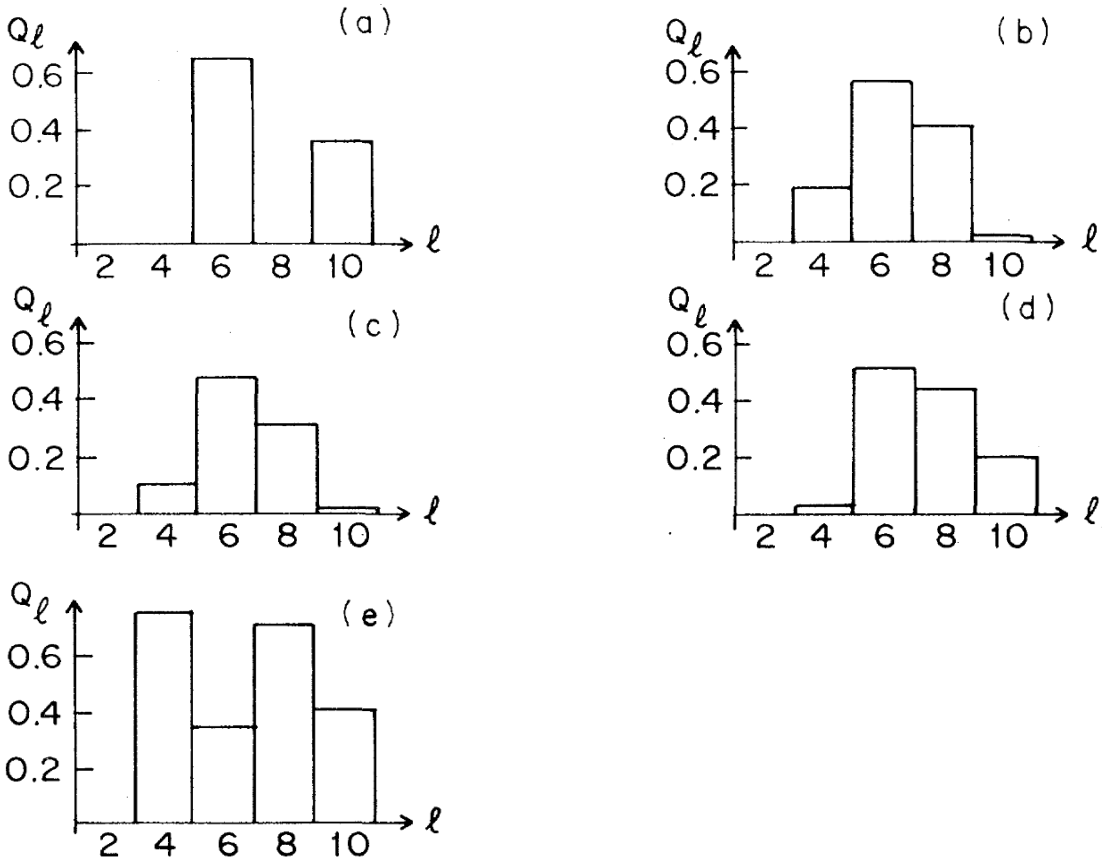

Figure 5.6: Histograms of $\mathcal{Q}_l$ with even ℓ for simple crystal structures. Figure is taken from Ref.[47].

harmonics with odd ℓ are anti-symmetric by inversion and so the corresponding $q^{(i)}_{\ell m}(r_{ij})$ is zero by construction. Moreover, The spherical harmonics $\mathcal{Y}_{00}$ is not suitable because its value is always constant ($\mathcal{Y}_{00} = 1/\sqrt{4\pi}$), so the corresponding order parameter $\mathcal{Q}_{00}$ depends only on the number of neighbours and not on their orientation. This means that ordered and disordered phases may have the same $\mathcal{Q}_\ell$. In Fig.(5.6) the value of $\mathcal{Q}_\ell$ with even ℓ (ℓ = 2, 4, 6, 8, 10) are reported for few simple crystalline structures. It is worth to note that for the icosahedral geometry only the $\mathcal{Q}_\ell$ with $\ell = 6, 10$ are different from zero. From Fig.(5.6) it is clear that the only $\mathcal{Q}_\ell$ that has a high value for every crystal geometry is the $\mathcal{Q}_\ell$ of 6-th order. Tab.5.1 shows value of $\mathcal{Q}_6$ for different geometries. It is worth to note that the value of $\mathcal{Q}_6$ is included in the range from 0.35 to 0.66 and for

	fcc	hpc	bcc	sc	ico	liquid
$\mathcal{Q}4$	0.191	0.097	0.036	0.764	0	0
$\mathcal{Q}6$	0.575	0.485	0.511	0.354	0.663	0

Table 5.1: Bond order parameter $\mathcal{Q}_4$ and $\mathcal{Q}_6$ for a set of simple geometries. fcc: face centered cubic structure; hpc: hexagonal closepacked structure; bcc: body centered cubic structure; sc: single cubic structure; ico: icosahedral structure; tetra: tetrahedral structure.

every crystal phase is significantly different from zero. In such way the order parameter $\mathcal{Q}_6$ is able to measure the crystallinity of a system, that is the first requirement for a order parameter. Moreover the $\mathcal{Q}_6$ parameter is very useful for a restrained MD, in the sense that none of the crystal phase is favourite with respect to another. Indeed, a MD can be driven from a liquid to an ordered phase simple forcing the system to increase its value of $\mathcal{Q}_6$. Any of the crystal structure can be formed because all the crystal phases have a value of $\mathcal{Q}_6$ well above zero and their values are very similar to each other.

It is worth to note that the values of $\mathcal{Q}_6$ in Tab.5.1 are relative to an ideal case where the system has zero temperature and infinite size. For real systems at finite temperature the value of $\mathcal{Q}_\ell$ oscillates around the value reported in Tab.5.1. Moreover for finite systems the value of $\mathcal{Q}_6$ for a liquid is not zero, but it is usually very small. This value decreases with N, number of atoms, with the usual $1/\sqrt{N}$ law. It is also worth to mention that the value of $\mathcal{Q}_6$ of amorphous sample is very near to zero, like in liquids.

The $\mathcal{Q}_\ell$ order parameter as defined in Eqs.(5.17, 5.16, 5.15) is not suitable for restrained molecular dynamics because of the presence of a cutoff radius used to identify nearest neighbor atoms. This means that $\mathcal{Q}_\ell$ is not a continuous differentiable function. This drawback can lead to an impulsive dynamics. In order to avoid this problem, a smooth approximation of Eq.(5.16) is defined. In this approximation, each $q^{(i)}_{\ell m}(r_{ij})$ term is weighted by a function of the r_{ij} distance. This function goes smoothly from 1 (when $r_{ij} < R_c$) to 0 (when $r_{ij} > R_c$) where R_c is the cutoff radius used to find the nearest neighbours. The new functional form of the $q^{(i)}_{\ell m}(r_{ij})$ is given by

$$q_{\ell m}^{(i)}(r_{ij}) = \frac{1}{M_i} \sum_{j=1}^{M_i} \mathcal{Y}_{\ell m}(r_{ij})\ \mathcal{S}(|r_i - r_j|; R_c) \tag{5.18}$$

where $\mathcal{S}(|r_i - r_j|; R_c)$ is the smooth function mentioned above. Different analytical forms of the smooth function can be used. The one used in this work is based on the Fermi function

$$\mathcal{F}(r_{ij} - R_c; \lambda) = \frac{1}{e^{\lambda(r_c - R_c)} + 1} \tag{5.19}$$

λ is a parameter controlling the smoothness of the function. The Fermi function does not definitively goes to zero in a certain range.

In conclusion, the bond orientational order parameter of Steinhardt *et al.* satisfies all the requirements of a "good" order parameter. As a matter of fact it is sensitive to the degree of crystallinity in the system but insensitive to the specific nature of the system (see Tab.5.1). Moreover the $\mathcal{Q}_\ell$ is insensitive to the orientation of the crystal in the space. This requirement is satisfied by the rotationally invariant combination of Eq.(5.17). The $\mathcal{Q}_\ell$ is relative easy to calculate because the only requirement is to know the nearest neighbours of the atoms. Finally, using the $q_{\ell m}^{(i)}(r_{ij})$ of Eq.(5.18), the $\mathcal{Q}_\ell$ order parameters is also suitable for a restrained molecular dynamics.

The bond order parameter of Steinhardt *et al.* [47] is developed for bulk systems. On the contrary, we want to monitor/accelerate the crystallization in a confined system Thus, the original definition of $\mathcal{Q}_{\ell m}(r_{ij})$ is modified by limiting the sum to just the atoms belonging to the nano-particle. The functional form of $\mathcal{Q}_{\ell m}(r_{ij})$ in the case of confined systems is given by

$$\mathcal{Q}_{\ell m}(r_{ij}) = \frac{\displaystyle\sum_{i=1}^{N} M_i\ q_{\ell m}^{(i)}(r_{ij})\ \left(1 - H(|r_i^{Si} - r_c| - \mathcal{R}^*)\right)}{\displaystyle\sum_{i=1}^{N} M_i} \tag{5.20}$$

where $H(x)$ is the Heaviside step function (see Eq.5.11) and $\mathcal{R}^*$ is the size of the given nano-particle (see Sec.(3.1)). The last term in Eq.5.20 damps down abruptly the $q_{\ell m}^{(i)}(r_{ij})$ contributions of the Silicon atoms beyond the radius of the nano-particle.

The biasing potential related to $\mathcal{Q}_6(x)$ gives rise to additional contributions to the interatomic forces that include the term $\nabla\mathcal{Q}_\ell$. There is therefore the problem of computing the derivative of an Heaviside step function, which would produce an impulsive force. This problem is solved by replacing the Heaviside step function $H(x)$ with a sigmoid function $S(x)$, which makes the force no longer impulsive. In conclusion, the functional form of the $\mathcal{Q}_{\ell m}(r_{ij})$ implemented in the restrained molecular dynamic is

$$\mathcal{Q}_{\ell m}(r_{ij}) = \frac{\sum_{i=1}^{N} M_i \; q_{\ell m}^{(i)}(r_{ij}) \; \mathcal{S}(|r_i^{Si} - r_c| - \mathcal{R}^*)}{\sum_{i=1}^{N} M_i} \tag{5.21}$$

Also in this case the sigmoid function is defined in terms of a Fermi function (see Eq.(5.19)). In this case the parameter λ, controlling the smoothness of the sigmoid, is chosen such that the sigmoid goes from 0.95 to 0.05 in one atomic layer (≈ 2 Å). In this way only the atoms belong to the nano-particle according to the definition $|r_i^{Si} - r_c| \leq \mathcal{R}^*$ are biased.

4 Improving the Sampling of the Configurational Space

Despite the use of biased MD, the calculation of $\partial\mathcal{F}(\mathcal{Q}_6^*;\mathcal{R}^*)/\partial\mathcal{Q}_6^*$ through Eq.(5.8) resulted to converge very slowly for some values of $\mathcal{Q}_6^*$. This is because there can exist more than one metastable state in the domain of unbiased degrees of freedom corresponding to the same $\mathcal{Q}_6^*$ value. If these metastable states are separated by a free energy barrier larger than the thermal energy, then the ergodic hypothesis on the unbiased degrees of freedom at the basis of Eq.(5.8) is violated: therefore mean force cannot be accurately estimated via the biased MD described above. An example is offered by the two quasi-crystalline configurations shown in Fig.(5.7), corresponding to the same value of the $\mathcal{Q}_6$ parameter, but embedding different defected structures. The configuration shown in the top panel is characterized by an extended disordered region in the bottom-right part of the nano-particle. At a variance, two smaller disordered regions characterize the sec-

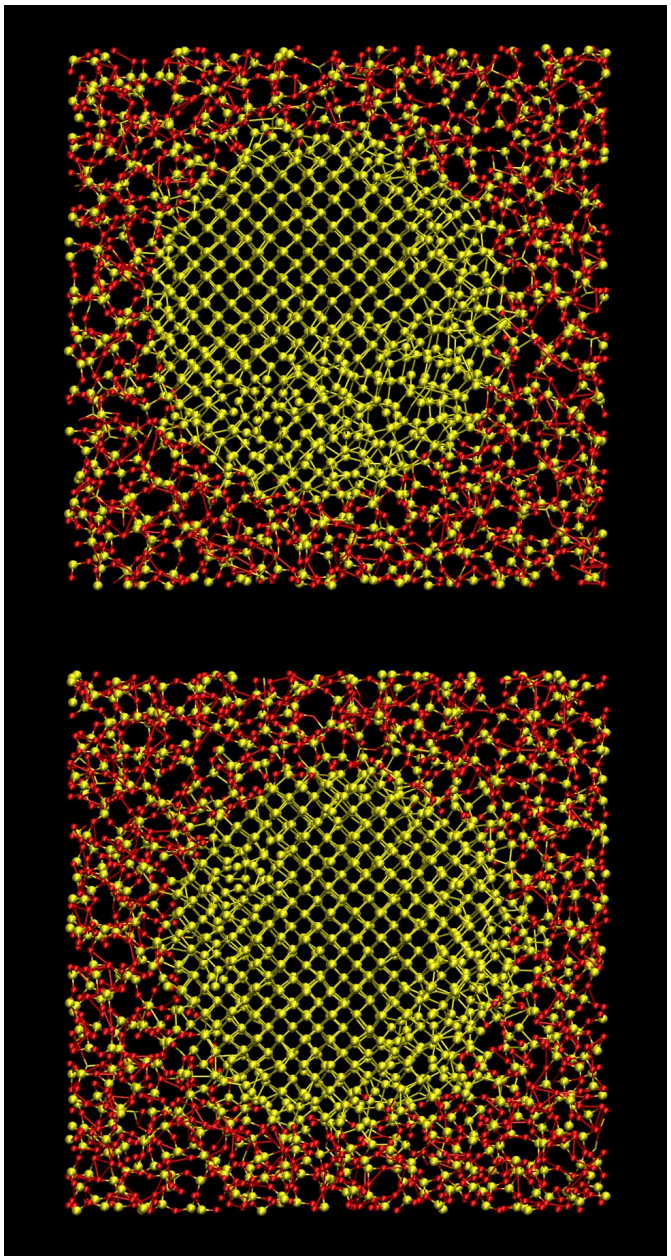

Figure 5.7: Two different configurations of an embedded silicon nano-particle with radius as large as 0.18 nm. They both correspond to $\mathcal{Q}_6^* = 0.19$. Oxygen atoms are displayed in red and Silicon atoms in yellow. In order to improve the readability, only the atoms laying within a 15 Å-thick slice are drawn.

ond configuration shown in bottom panel, respectively in the bottom-right and top-left part of the nano-particle. Both configurations should be considered for the correct evaluation of the integral appearing in Eq.(5.8) corresponding to the same value of $\mathcal{Q}_6^*$. While these additional "slow" but unbiased degrees of freedom most likely affect the mechanism of nucleation of an ordered phase within the disordered nano-particle (and vice versa), our description of the temperature-induced disorder-to-order transition depends only on the relative stability of the initial and final metastable states (which are adequately described by the $\mathcal{Q}_6^*$ and $\mathcal{R}^*$ collective coordinates). The difference of free energy between the two states can be computed by integrating the mean force along whatever path connecting them. Therefore the original plan can still followed, namely computing and integrating the mean force on $\mathcal{Q}_6^*$ at fixed values of $\mathcal{R}^*$, provided that the derivative of the free energy can accurately computed.

4.1 Parallel Tempering (aka Replica Exchange Method)

The problem of poor sampling is solved by combining biased MD with the parallel tempering (also known as replica exchange method) [59].

The basic idea of the parallel tempering is to simulate a number of replicas of the original system each in a canonical ensemble and at different temperatures [59, 60, 61]. Each replica of the system, at its own temperature, is simulated in parallel with the others. From time to time two replica are allowed to exchange their configurations according to a given probability. This procedure guarantees an ergodic sampling of the system. As replica at high T can overcome free energy barriers and visit unsampled meta-stable states. Then, their swapping at low temperature allows to perform a proper sampling of the unsampled region at the relevant physical T. In conclusion, the key feature of this method is that the sampling of the system phase space obtained by the piece-like replica exchange trajectories is consistent with the canonical probability density function at each target temperature. However, since the individual pieces of the replica exchange trajectories are obtained by swapping from higher temperatures, they more likely overcome possible free energy barriers. In short: the replica exchange trajectories are ergodic.

In practice, in this work a version of replica exchange method for molecular

dynamics developed by Sugita and Okamoto [61] is used. In the following a description of the principles of this method will be described. Let us consider a general system of N atoms. The Hamiltonian of this system is given by the sum of the kinetic energy $K(\vec{p})$ and the potential energy $V(\vec{r})$, where the coordinates of all the atoms are denoted with the set $\vec{r} \equiv \{\vec{r}_1, \ldots, \vec{r}_N\}$ and the momenta with the set $\vec{p} \equiv \{\vec{p}_1, \ldots, \vec{p}_N\}$.

$$H(\vec{r}, \vec{p}) = K(\vec{p}) + V(\vec{r}) \tag{5.22}$$

where

$$K(\vec{p}) = \sum_{i=1}^{N} \frac{\vec{p}_i^{\,2}}{2m_i} \tag{5.23}$$

here m_i is the mass of the i-th atom. In the present case $V(\vec{r})$ is the biased potential of Eq.5.3. Each replica of the system can be identified by the set of coordinates and momenta and by the temperature. Thus, for the i-th replica at the temperature T_m we can define the replica $x^i_{T_m}$ as

$$x^i_{T_m} \equiv (\vec{r}^{\,i}, \vec{p}^{\,i})_{T_m} \tag{5.24}$$

here the index i identify the replica and the subscript is related to the temperature of the replica. If we consider a generalized ensemble formed by all the M replica of the system, we can define a state X of this generalized ensemble as the set of all the M replica of the system

$$X \equiv (x^i_{T_m}, \ldots, x^M_{T_M}). \tag{5.25}$$

In the canonical ensemble at the temperature T each state is weighted by the Boltzmann factor $\exp(-\beta H(\vec{r}, \vec{p}))$ with $\beta = 1/k_B T$. As a consequence of the fact that the replica are non interacting, the Boltzmann factor W of the state X of the generalized ensemble is given by the product of the Boltzmann factor of each replica. Thus, the partition function of the extended system is given by

$$
\begin{aligned}
W(X) &= \prod_{i=1}^{M} W_i \\
&= \exp\left(-\sum_{i=1}^{M} \beta_i \, H(\vec{r}^{\,i}, \vec{p}^{\,i}) \right)
\end{aligned}
\tag{5.26}
$$

where $\beta_m = 1/k_B T_m$ and $W_i = \exp(-\beta_i H)$ is the canonical partition function for a single replica i at temperature T_i.

When a swapping between a pair of replicas is attempted, the coordinates of the replica are exchanged while the momenta are rescaled to the target T. Let us suppose that the i-th replica at temperature T_m is swapped with the replica j-th at temperature T_n. The exchange of replica can be written as

$$
\begin{cases}
x^i_{T_m} \equiv (\vec{r}^{\,i}, \vec{p}^{\,i})_{T_m} \;\longrightarrow\; x^{j'}_{T_m} \equiv (\vec{r}^{\,j}, \vec{p}^{\,j'})_{T_m} \\
x^j_{T_n} \equiv (\vec{r}^{\,j}, \vec{p}^{\,j})_{T_n} \;\longrightarrow\; x^{i'}_{T_n} \equiv (\vec{r}^{\,i}, \vec{p}^{\,i'})_{T_n}
\end{cases}
\tag{5.27}
$$

where the $\vec{r}^{\,i}$ are simply exchanged with the $\vec{r}^{\,j}$ while the momenta are rescaled following the given criterion

$$
\begin{cases}
\vec{p}^{\,i'} = \sqrt{\dfrac{T_n}{T_m}} \, \vec{p}^{\,i} \\
\vec{p}^{\,j'} = \sqrt{\dfrac{T_m}{T_n}} \, \vec{p}^{\,j}
\end{cases}
\tag{5.28}
$$

This uniform rescaling of the momenta by the square root of the ratio of the two temperatures ensures that the average kinetic energy remains equal to $3/2 N k_B T$

$$
\langle K(p) \rangle = \langle \sum_{k=1}^{N} \frac{\vec{p}^{\,2}_k}{2\, m_k} \rangle = \frac{3}{2} N k_B T. \tag{5.29}
$$

When a swapping move is performed the corresponding state of the generalized ensemble is modified as follow

$$
X \equiv (\dots, x^i_{T_m}, \dots, x^j_{T_n}, \dots) \rightarrow X' \equiv (\dots, x^{j'}_{T_m}, \dots, x^{i'}_{T_n}, \dots). \tag{5.30}
$$

Imposing the detailed balance condition on the transition probability $w(X \rightarrow X')$ we obtain

$$W(X)\, w(X \to X') = W(X')\, w(X' \to X) \tag{5.31}$$

From Eqs.(5.22,5.23,5.26,5.31) we obtain

$$\begin{aligned}\frac{w(X \to X')}{w(X' \to X)} &= \exp\Big(-\beta_m H(\vec{r}^{\,j}, \vec{r}^{\,j'}) - \beta_n H(\vec{r}^{\,i}, \vec{r}^{\,i'}) + \beta_m H(\vec{r}^{\,i}, \vec{r}^{\,i}) + \beta_n H(\vec{r}^{\,j}, \vec{r}^{\,j})\Big) \\ &= \exp\Big(- (\beta_n - \beta_m)\, (V(\vec{r}^{\,i}) - V(\vec{r}^{\,j}))\Big)\end{aligned} \tag{5.32}$$

The move can be accepted/rejected according to the Metropolis criterion

$$w(X \to X') = \begin{cases} 1 & \text{for } \Delta \leq 0 \\ \exp(-\Delta) & \text{for } \Delta > 0 \end{cases} \tag{5.33}$$

where $\Delta \equiv (\beta_n - \beta_m)\, (V(\vec{r}^{\,i}) - V(\vec{r}^{\,j}))$. If the swapping is rejected, the microstates are further aged at their own temperature.

Summarizing, a parallel tempering procedure consists in two steps:

i) A certain number of replicas of the system is simulated at different temperature simultaneously and independently for a fixed number of steps;

ii) A pair of replica are exchanged according to the probability given by Eq.(5.33).

Typically only the swapping between adjacent temperatures is allowed. In Fig.5.8 a schematic picture of the swapping process is shown.

Unfortunately, there are no simple tests to be performed to check the adequacy of the maximum T. One can just compare the results obtained with and without parallel tempering. Anticipating the results, with the use of the constrained molecular dynamics plus parallel tempering two meta-stable states are found. One is relative to the crystalline nano-particle and the other corresponds to the amorphous particle. It is worth to note that the same results are obtained starting the dynamics from the disordered phase and going to the ordered one and *viceversa* (no hysteresis). On the contrary without parallel tempering only one meta-stable state is found. Moreover, the nature meta-stable of this state depends on the direction of the path followed by the restrained molecular dynamics. Indeed, starting from a disordered phase and going toward the crystalline,

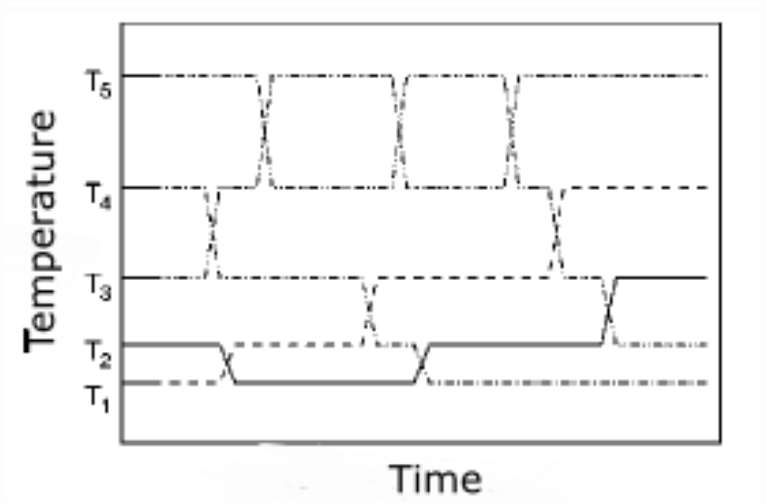

Figure 5.8: Schematic swapping between the replicas in a parallel tempering simulation. Figure takes from Ref.[60].

only the meta-stable state corresponding to the amorphous phase is found. While moving in the opposite direction only the crystalline meta-stable state is found. This hysteresis is a consequence of a poor sampling of the phase space which produce an unreliable mean force. The behavior described above is well represented by the free energy vs. $\mathcal{Q}_6$ curves reported in Fig.(5.10). These curves have been obtained with restrained MD without parallel tempering and have been computed following the two opposite path described above.

It is evident that two different metastable states are obtained. The results shown in Fig.(5.9) should be compared with the one obtained with the parallel tempering reported in the middle panel of Fig.((5.10)). We can see that using parallel tempering two meta-stable states are found. It is worth noticing that in the latter case the same results are obtained through both paths. This clearly illustrates that parallel tempering allows to get out meta-stable states in the remaining possible "slow" degrees of freedom not accelerated by the bias on $\mathcal{Q}_6$ (see Fig.(5.7)).

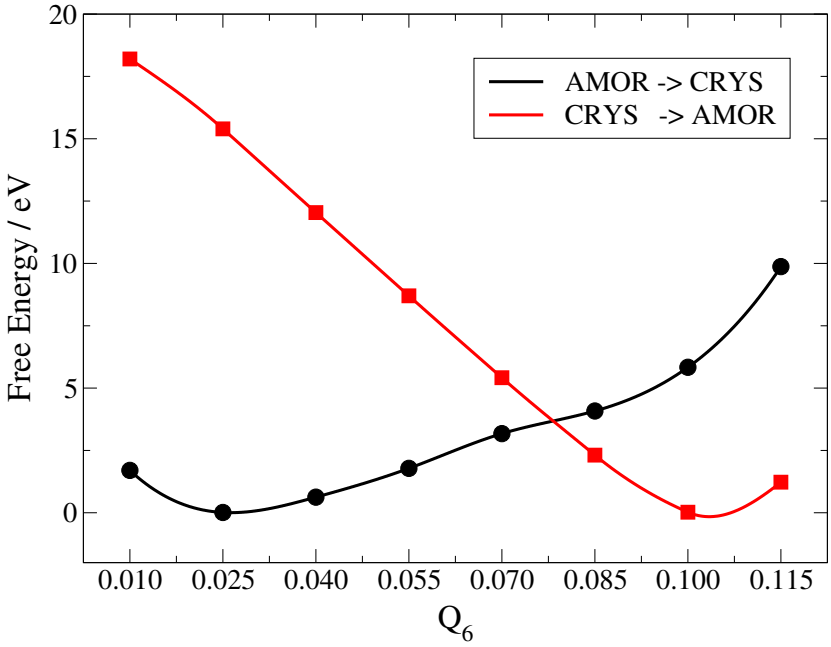

Figure 5.9: Free energy profiles as a function of the bond order parameter $\mathcal{Q}_6$ for the system n-Si/SiO_2 containing a Si nano-particle with a radius of 1.3 nm at the temperature of 750 K. The free energy profile reported in black/circle line is relative to the path from amorphous to crystalline phase. While the free energy profile relative to the path from crystal to amorphous is reported with the red/square line.

5 Simulation Protocol

The simulations proceed as follows. Eight biased MD simulations are run in parallel at different temperatures (ranging from 500 K and 2000 K) but at the same target value of $\mathcal{Q}_6^*$ and $\mathcal{R}^*$. After a relaxation time, in which the swapped trajectories reach the thermal equilibrium at the new temperature, we use these trajectories to compute the integral of Eq.(5.8). In principle, the replica exchange method implies the extra cost of running several MD simulations at different temperatures. However, since we are interested in computing the free energy at all these temperatures we rather took advantage by following this procedure. The parallel tempering technique can make efficient use of large CPU clusters where

the replicas can be run in parallel. In practice, we implemented the replica exchange/biased MD scheme in our CMPTool code [62, 63] by adopting a two-fold parallel scheme. Since the replica exchange protocol involves a minimal level of synchronization and interaction among the independent biased MD runs, parallelism is here implemented at a level of scripting language. However, as mentioned above, each individual MD simulation is computationally intensive as the samples contains up to ~ 12000 atoms. Therefore, each MD simulation is a parallel run implemented by the Message Passing Interface (MPI) API [64]. Each MPI simulation was ran on eight cores and, therefore, the complete replica exchange/biased MD simulation was globally executed on 64 cores. One advantage of this approach is that it works well also on non-tightly connected cluster of multicore/multisocket machines. For example, part of the simulations were ran on a cluster of quad-core/dual-socket compute nodes interconnected via gigabit Ethernet.

6 Results

6.1 Order-Disorder Phase Change

Before presenting the results, the experimental findings, which are interpreted atomistically, are summarized. By comparing Energy Filtered Transmission Electron Microscopy (EFTEM) and Dark-Field Transmission Electron Microscopy (DFTEM) images in Si-rich SiO_x samples it was shown that Si nano-particles start to form at 1000°C [46]. At this temperature they all are amorphous, while at 1100°C about one third become crystalline. By further increasing the annealing temperature by 50°C, the fraction of crystalline nano-particles rises up to 60%, while the average size of the nano-particles and the distribution of their size remains almost unchanged. Finally, at the annealing temperature of 1250°C, 100% of nano-particles are crystalline. At this temperature the average size is slightly increased, but the particle size distribution is still largely superimposed to the distributions observed at 1100°C and 1150°C. It was also found that the system has reached the thermodynamic equilibrium with respect to the amorphous vs. crystalline population. Similar investigations have been performed on Si/SiO_2 multilayers [46] where the growth of the crystalline fraction with the annealing

temperature is even more sudden: the degree of crystallinity increases from about 15% to 90% when the annealing temperature is increased from 1100°C to 1200°C. Also in this case it was demonstrated that the samples are at the equilibrium.

Turning to the results of the present simulations. In Fig.(5.10) are shown the free energy curves of Si nano-particles of size $\mathcal{R}^* = 0.8$ nm, $\mathcal{R}^* = 1.3$ nm, and $\mathcal{R}^* = 1.8$ nm at various temperatures in the range 227°C - 1477°C (please note that calculation were performed in Kelvin while the results are presented in Celsius for homogeneity with available experimental data). It is worth mentioning that this curves are computed both starting from the crystalline region (high $\mathcal{Q}_6$) and going toward the amorphous region (low $\mathcal{Q}_6$) and vice versa without observing any significant difference. In other words, the results are not affected by hysteresis. The present simulations provide a qualitative but sharp picture, namely: for small nano-particles ($\mathcal{R}^* = 0.8 - 1.3$ nm) at low temperature (T < 727°C) the most stable configuration corresponds to a disordered phase, while the crystalline state is found to be more stable at higher temperatures. On the contrary, for larger particles ($\mathcal{R}^* \geq 1.8$ nm) this behavior is inverted resulting similar to bulk-like conditions: at low temperatures (T < 977° C) the crystalline phase is the most stable one, while the disordered phase is preferred at higher temperatures. Interestingly enough, for small nano-particles the equilibrium temperature (i.e. the temperature at which the free energy of the disordered and ordered phase are the same) decreases with the increase of the size of the nano-particle. This is indeed an effect of the steady increase of stability of the crystalline phase with respect the disordered one with the size of the nano-particles.

The simulations further provide the following all-atom picture, consistent with the experimental results. At low annealing temperature the nano-particles are small and amorphous as, due to the inversion of stability with respect to bulk-like systems, this is thermodynamically the most stable phase. At moderately higher temperatures the size and the size distribution of the nano-particles is unchanged and the largest particles in the sample transform from amorphous to crystalline, the most stable phase at this temperature. By further increasing the temperature the average size of the nano-particles increases and the larger nano-particles tend toward the crystalline state (i.e. they follow the change in stability from disorder to order, as induced by their growing size). On the other hand, the smaller particles undergo a disorder-to-order transition due to the increase of

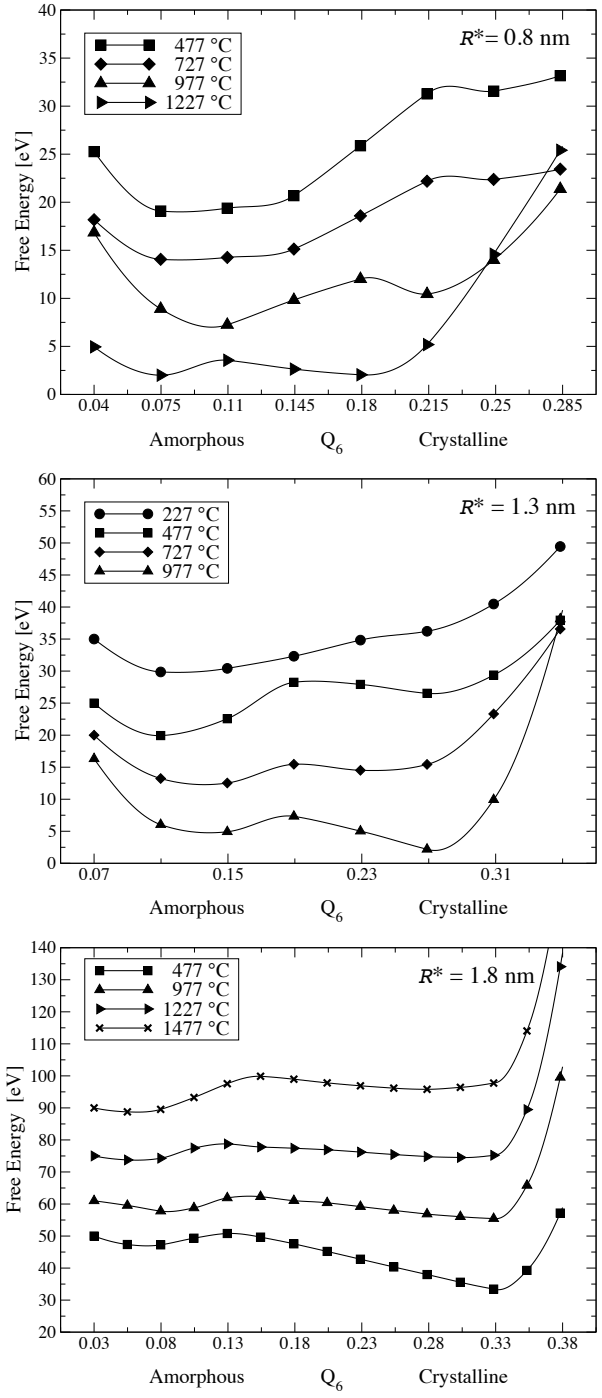

Figure 5.10: Free energy vs $\mathcal{Q}_6$ curves for nano-particles with radius 0.8 nm (top), 1.3 nm (middle) and 1.8 nm (bottom). The curves are shifted to improve readability.

the temperature and the inversion of the stability with respect to the bulk-like system. Even in this case they eventually crystallize.

6.2 Structural Trends

Fig.(5.10) contains also information on the structural differences among nano-particles with unsimilar size. These information are provided by the values of $\mathcal{Q}_6^*$ corresponding to the local minima of the free energy. Let us indicate such values as $\mathcal{Q}_6^d(\mathcal{R}^*, T)$ and $\mathcal{Q}_6^c(\mathcal{R}^*, T)$, for the disordered and crystalline phase respectively. We remark that the $\mathcal{Q}_6^d(\mathcal{R}^*, T)$ turns out to be essentially independent from both the size and the temperature. This indicates that there is essentially no effect on the ordering by these parameters in the disordered phase. This is because in disordered (amorphous) Si there is only short range order which is hardly affected by the size of the nano-particle and by the temperature. On the contrary, $\mathcal{Q}_6^c(\mathcal{R}^*, T)$ is affected by both the temperature and the size. In the following we shall compare the $\mathcal{Q}_6^c(\mathcal{R}^*, T)$ corresponding to temperatures well within the domain of stability of the crystal line phase, namely 1227 °C, 977 °C and 477 °C corresponding to the 0.8 nm, 1.3 nm and 1.8 nm nano-particles, respectively. The values of $\mathcal{Q}_6^c(\mathcal{R}^*, T)$ are 0.18, 0.27 and 0.33 for the 0.8 nm, 1.3 nm and 1.8 nm nano-particles, respectively, clearly indicating that the order increases for larger dots tending to the bulk value ($\mathcal{Q}_6 \approx 0.63$ at $T = 0$ K and $\mathcal{Q}_6 \approx 0.57$ at $T = 1000$ K).

The $\mathcal{Q}_6$ difference between bulk Si and crystalline nano-particles possibly stems from two effects. On the one hand, this difference might be due to the presence of the interface: atoms at the interface have a different environment from atoms in the core and this reduces the total $\mathcal{Q}_6$. On the other hand, the difference could be due to a distortion of the core of the nano-particle or to the presence of a significant number of localized as well as extended defects in the internal region.

In the text above the fact that the meta-stable state at higher $\mathcal{Q}_6$ correspond to a crystalline one has been assumed. However, this is not at all self-evident and a more specific analysis need to be carried out in order to prove it. This is especially needed as we can see that the higher $\mathcal{Q}_6$ meta-stable state of the 0.8 nm nano-particle is in the same $\mathcal{Q}_6$ range of the low $\mathcal{Q}_6$ meta-stable state of the

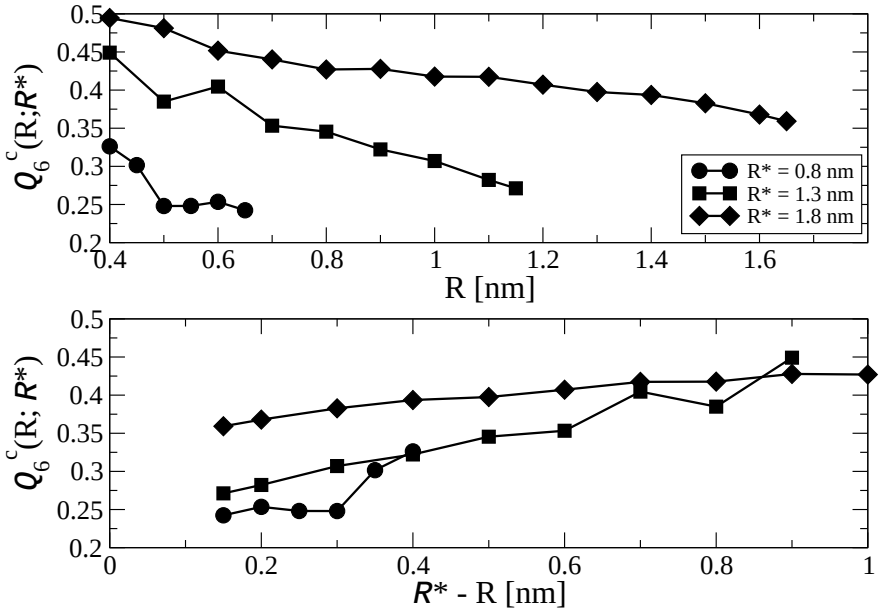

Figure 5.11: (top) $\mathcal{Q}_6^c$ as a function of the distance R from the center of the nano-particles. (bottom) $\mathcal{Q}_6^c$ as a function of the distance from the interface.

1.3 nm one, which seems to indicate a significant difference in the structure as a function of the size.

Indeed after having confirmed that the meta-stable states at high $\mathcal{Q}_6$ are crystalline, remains to demonstrate the origin of the different level of order in the crystalline phase of nano-particles of different size. In particular, we want to address the question whether in smaller nano-particle the larger level of disorder is homogeneously distributed or localized in a specific region.

Experimental results on Si nano-particles and, more in general, on confined systems, indicate that the degree of order decreases in going from the center to the surface of the cluster [65, 66]. In order to clarify this issue we computed the $\mathcal{Q}_6$ by including only atoms falling within a given distance R from the center of the nano-particle ($\mathcal{Q}_6^c(R;\mathcal{R}^*)$). The top panel of Fig.(5.11) demonstrates that the degree of order as measured by the $\mathcal{Q}_6^c(R;\mathcal{R}^*)$ decreases in going from the center

to the periphery of the nano-particles. Once again, this result is consistent with the experimental picture of Ref.[65, 66].

Present results suggest that well established theories for modeling the nucleation of new phases, such as the classical theory of nucleation (see [67]), are inadequate in the case of formation of Si nano-particles in amorphous silica. In fact, several results contrast with the basic assumption of these theories. Perhaps the most relevant one is that Si nano-particles are initially formed amorphous and then transformed into crystalline, as shown by experiments and by now understood by our simulations. As a consequence, the chemical potential is not constant during the nucleation and growth of the nano-particle, as assumed in the classical nucleation theory. In addition, the results shown in Fig.(5.11) also suggest that: i) when the nano-particle is in the crystalline phase the structure as described by the $\mathcal{Q}_6^c$ parameter is different from the bulk one and therefore the chemical potential should differ from the bulk value as well; ii) the $\mathcal{Q}_6^c$ changes in going from the center to the periphery of the nano-particle and therefore the chemical potential will not be constant within the nano-particle; and iii) $\mathcal{Q}_6^c$ depends on the size of the nano-particle and therefore the chemical potential and the surface free energy change during the nucleation process.

Another interesting conclusion can be achieved by reporting the $\mathcal{Q}_6^c(R;\mathcal{R}^*)$ versus $\mathcal{R}^* - R$ (i.e. the distance from the interface), as shown in the bottom panel of Fig.(5.11). From this plot we conclude that far enough from the interface the degree of order is independent of the nano-particle size. On the other hand, $d\mathcal{Q}_6^c(R;\mathcal{R}^*)/dR$ strongly depends on the size of the nano-particle close to the interface. A possible qualitative interpretation relies on the assumption that the matrix is a source of stress on the nano-particle. Such a stress field generates a distortion (with respect to the bulk configuration) which is randomly distributed on the interface atoms. This prevents the reconstruction that normally occurs at surfaces. Furthermore, since the number of interface atoms among which the stress is distributed changes as a function of the size of the nano-particle (in particular is proportional to $(\mathcal{R}^*)^2$), the degree of distortion at the interface is a function of the nano-particle size. The stress induced by the matrix is balanced by the opposite action of the crystalline core of the nano-particle. Let us call this effect "inertia" of the nano-particle against the distortion. This phenomenon is as well function of the area of the layer which is subject of this inertia which, for a

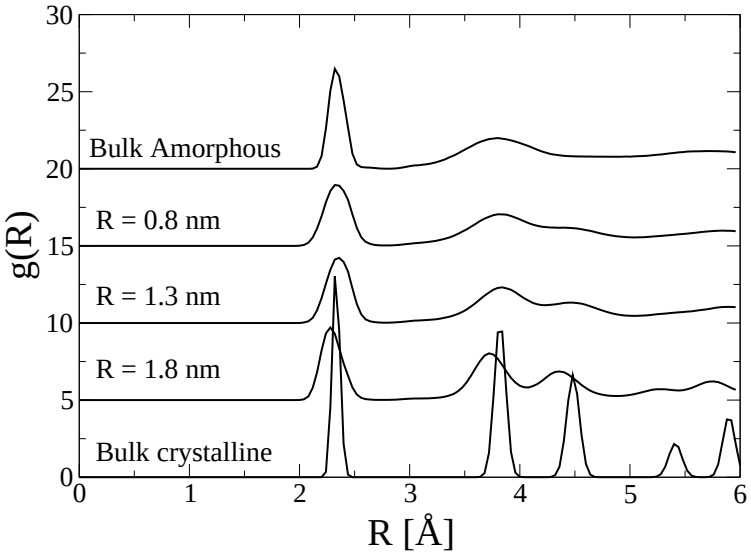

Figure 5.12: Pair distribution function of nano-particles of different size. For comparison, the g(r) of bulk silicon is also reported.

given distance from an interface, is stronger for smaller nano-particles. The overall effect of the two contrasting phenomena is inducing a disorder distributed over few layers beyond which the original order is recovered. For the reasons described above, the (negative) slope of $\mathcal{Q}_6^c(R;\mathcal{R}^*)$ is higher for smaller nano-particles. Of course there can be cases in which the level of order in the nano-particle cannot recover the bulk value. For example, in the present simulations only the largest particle recover the finite temperature bulk value in the core region.

The structural differences among the crystalline phase of the three nano-particles is also illustrated by the g(r) calculated on the biased MD trajectories (see Fig.(5.12)). Indeed, the main difference between bulk crystalline Si and the largest nano-particle is, essentially the intensity of the peaks, which however remain all well separated. In particular, the intensity of the first peak is significantly decreased but its integral is preserved. This means that the number of nearest neighbors is preserved. Indeed, the change of intensity is due to a broader distribution of the Si-Si bond length rather than an increase of the Debye-Waller

factor, which is essentially unchanged between the bulk and nano-sized Si. With the shrinking of the nano-particle the second set of peaks becomes broader and less intense. However, also in the case of the 0.8 nm nano-particle, the two peaks of the second set are still visible. As for the first peak, its intensity is not significantly affected by the size of the nano-particle. These results indicate that also in small nano-particle there is still a short and medium range order. Concluding, the ordered states of the three nano-particle are identified to be crystalline.

Chapter 6

Committor Analysis

For many physical problems the energy landscape is characterized by some meta-stable states separated by energy barriers. The configuration corresponding to this energy barrier is often call transition state. The study of the transition processes, i.e. the path by which the system goes from one meta-stable to another, has been a topic of great interest in the recent years. In the reconstruction of the transition pathways the low temperature limit approximation is often made. This allows to focus on the most likely path rather than computing the ensemble of transition paths. In cartesian coordinates, this path is represented by the minimum energy path (MEP). The MEP allows us to identify the relevant saddle points which are the bottlenecks of a reaction process.

Several methods have been proposed in order to identify and analyze the MEP of a transition. The most successful are the nudged elastic band (NEB) [68, 69], the zero-temperature-string method (ZTS) [70, 71], the transition path sampling (TPS) [72, 73, 74].

Unfortunately, the methods mentioned above are not well suited for complex system with many degrees of freedom and only few of them participating into the process (e.g. chemical reaction in solution). For these systems the standard technique is to coarse grain the system using a set of collective coordinates. A collective variable is a property of the system, that alone or in conjunction with others, is able to properly describe the process. Examples of collective variables are bond length, bond and dihedral angles but more complex, and more collective, variables might also be needed for describing the process. The $\mathcal{Q}_6$ collective variable introduced in Sec.(3.2) is an example of this second class of collective

variables.

The success of this approach depends strongly on the choice of the collective coordinates. Indeed if little is known about the mechanism of a reaction a poor choice of the collective coordinates may lead to a wrong description of the transition mechanism. Due to the fact that the system may sample the wrong part of the phase space. It is worth noticing that a coordinate that is able to distinguish between two meta-stable states may be not sufficient to characterize also the dynamical process between them. In other words, the projection of the free energy landscape onto a lower dimensional space, the space of the collective coordinates, may be too restrictive for the representation of the process.

In general, the term order parameter is used for variables which are able only to distinguish between meta-stable states, while the term collective coordinate (variable) is used for coordinates which are also able to describe the mechanism of the transition. This distinction may be illustrated by an example, assume an energy landscape with two meta-stable states, A and B, as reported in Fig.(6.1). In the figure, two illustrative examples of two-dimensional energy landscapes are reported. In the top panels are shown the energy landscapes in the two-dimensional space (function of q and q'). The free energy in the two-dimensional space is given by $F(q,q') = -1/\beta \ \ln \rho(q,q')$ where $\rho(q,q')$ is the probability density function. In order to express the free energy as a function of only one coordinate we have to consider the marginal probability of $\rho(q,q')$ which for q is obtained integrating $\rho(q,q')$ over q': $\rho(q) = \int dq' \ \rho(q,q') = \int dq' \ \exp(-\beta F(q,q'))$. From the marginal probability one can obtain the free energy associated to $\rho(q)$, function of only q, which is given by $F(q) = -1/\beta \ \rho(q)$. In the bottom panels are reported the energy profile projected in the space of only the coordinate q. For both cases the coordinate q is a good order parameter. In the sense that if the free energy profile is reported as a function of q the two basins of attraction of the energy are well reproduced. In other words, the q coordinate is able to reproduce the bi-stable profile of the energy landscape. In such way the q coordinate is a good coordinate for obtain thermodynamic information in both cases. The same is not true if we want to know dynamical informations. In the left scenario the coordinate q can also used as collective coordinate because the maximum at $q = q^*$ is a good approximation of a transition state which divide the two basins of the energy. Instead, in the right scenario the q can not be used as

collective coordinate because the crossing events of the barrier occur also in the space of q' coordinate. This means that in the latter case the configurations of the phase space relative to the maximum at $q = q^*$ are pour approximations of the transition state. As a consequence in the right case the use of q as a collective coordinate can lead to misleading conclusions. This situation is common in real physical scenarios where complex systems are described with using few collective variables.

In the previous section, two meta-stable states have been found in the free energy landscape in the system of Si nano-particle embedded in a-SiO_2. It has been shown that the $\mathcal{Q}_6$ order parameters is able to reproduce the bi-stable nature of the systems. This means that the $\mathcal{Q}_6$ is a good order parameter. The aim of this section is to investigate the reliability of the $\mathcal{Q}_6$ parameter also as collective coordinate. If the $\mathcal{Q}_6$ parameter is also a good collective coordinate, informations about the mechanism of the nucleation of the Si nano-particle can also be obtained. Moreover the values of the free barrier energies can be taken in account for kinetic considerations.

1 Theoretical Background

Typically, a trajectory in a system with meta-stabilities spends most of the time in the meta-stable states. Sometimes, the trajectory goes (quickly) from one meta-stable state to another. This portion of the trajectory corresponds to the activated event. The dynamical informations on the transition can be obtained from the analysis of the reactive part of the trajectory. In this section a method to define the probability density of a reactive process is reported. This method implies the use of the committor function. The committor functions is the probability that a system at a given point in the phase space reaches the products before the reactants. It will be shown how to obtain dynamical informations, as transition rate and probability current, from the committor function.

Let consider a system of N atoms in which the dynamics is ergodic. This means that for a generic observable $\mathcal{O}(x)$, with $x \equiv (r^{3N}, p^{3N})$ a point in phase space, the time average is equivalent to the ensemble average in the limit of an

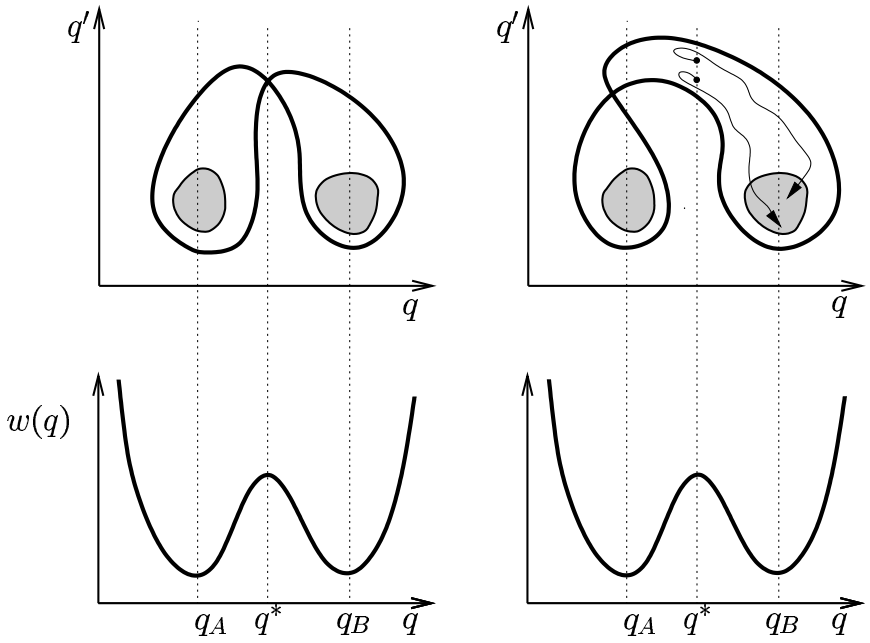

Figure 6.1: Two illustrative examples of bi-stable free energy landscapes. Top panels) Free energy landscapes as functions of two collective coordinates q and q'. Bottom panels) Free energy curves as functions of only the coordinate q. In both cases the bi-stable form of the energy landscape is well reproduced. In the left scenario q is a reasonable collective variable because the transition surface coincides with the maximum of the free energy in the bottom panel ($q = q^*$). In the example the coordinate q' is also important in the reaction mechanism. The maximum at $q = q^*$ does not coincide with the transition surface. Indeed trajectories started from a configuration with $q = q^*$ all end in the state B. In this case coordinate q alone is not a good collective coordinate. Figure taken from Ref.[74].

infinitely long trajectory

$$\lim_{T\to\infty}\frac{1}{T}\int_0^T \mathcal{O}(x(t))dt = \int_\Omega \mathcal{O}(x)\rho(x)dx \tag{6.1}$$

where $x(t)$ is a trajectory in the phase space Ω, $\rho(x)$ is the probability density and T is the duration of the trajectory.

Suppose to consider a bi-stable system with two meta-stable states A and B. Typically the system is confined in the two energetic attractive basins. Thus, a trajectory spends almost all the time in the region of the phase space given by the union of the two stable states $A \cup B$. A reactive trajectory $x(t)$ is a trajectory such that the system comes to A and goes into B. The set of reactive trajectories can be defined as $x(t) : x \in R$ where $t \in R$ if $x(t) \notin A \cup B$, and $x(t^+_{AB}) \in B$, $x(t^-_{AB}) \in A$ in which t^+_{AB} is the smallest time $(\Gamma, t)t$ in which the trajectory is either in A or B and t^-_{AB} is the largest time $\leq t$ such that the trajectory is either in A or B.

In a bimodal system, the probability density $\rho(x)$ is mostly localized in the portion of phase space $A \cup B$, and therefore is not an accurate indicator of the properties of the reactive trajectory. We therefore introduce the probability density function of reactive trajectories $\rho_R(x)$. $\rho_R(x)$ is the probability density of be in x conditional to the trajectory to be reactive. We now derive the form of this function. Let us introduce the indicator function χ_S

$$\chi_S = \begin{cases} 1 & \text{if } x \in S \\ 0 & \text{Otherwise} \end{cases} \tag{6.2}$$

where S is a set in Ω ($S \in \Omega$). Assuming ergodicity, we can define $\rho_R(x)$ through the following relation

$$\lim_{T\to\infty}\frac{1}{2T}\int_{-T}^{T} \mathcal{O}(x(t))\ \chi_{A\cup B}(x(t))\ \chi_A(x(t^+_{AB}))\ \chi_B(x(t^-_{AB}))\ dt = \int_{A\cup B} \mathcal{O}(x)\ \rho_R\ dx \tag{6.3}$$

This integral represents the average value of the observable $\mathcal{O}(x)$ compute along reactive trajectories as the integrant is non zero only when the condition to be reactive (see above) is met. The results of this is that the probability density of reactive trajectory is the probability to be in x times the probability to be reactive ($P_R(x)$): $\rho_R(x) = \rho(x) \cdot P_R(x)$ and the latter is the probability to comes from A

rather than B and to go to B rather than A. Therefore $\rho_R(x) = \rho(x)\ q_+(x)\ q_-(x)$, where q_+ and q_- are committor functions, forward and backward, respectively. The committor functions q_+ gives the probability that the trajectory reaches B rather than A, given that $x(t) = x$. While the backward committor function q_- is the probability that the trajectory came last from A rather than B, always given that $x(t) = x$. However, this equation is not normalized and therefore it need to be changed into

$$\rho_R(x) = \rho(x)\ q_+(x)\ q_-(x)\ /Z_{AB} \tag{6.4}$$

where Z_{AB} is the normalizing factor and it is given by

$$\begin{aligned} Z_{AB} &= \int_{A\cup B} \rho(x)\ q_+(x)\ q_-(x)dx \\ &= \lim_{T\to\infty} \frac{1}{T} \int_0^T \chi_{A\cup B}(x(t))\ \chi_B(x(t^+_{AB}))\ \chi_A(x(t^-_{AB}))\ dt \end{aligned} \tag{6.5}$$

Let us consider a time reversible dynamics, the probability that a system is in x at time t and in y at time $t + s$, with $s > 0$, is the same as the probability that the system is in y at time t and in x at the time $t + s$. For this dynamic the forward and backward committors are related by $q_-(x) = 1 - q_+(x)$, so the product of the committors in Eq.(6.4) leads to: $q_+(x)\, q_-(x) = q(x)\,(1 - q(x))$, where $q(x)$ takes the place of $q_+(x)$.

The explanation above demonstrates that the committor function is the key ingredient to compute the statistical information on reactive trajectories. Indeed, it can be shown that the committor function allows also to compute the reaction rate and other quantities.

Moreover, It is the statistical indicator of the progress of the transition from the state A to the state B. In such way the committor function is a key quantity to describe the statistical quantity of the reactive trajectory. It is therefore "the" collective coordinate of a process. In the sense that if $q(x)$ is known than whatever can be computed about a process. Unfortunately, it is a complex function of the positions and the momenta of all the atom in the system. In general, the committor function satisfies the backward Kolmogorov equation

$$\begin{cases} 0 = \displaystyle\sum_{i,j=1}^{N} \frac{\partial}{\partial x_i} \left(a_{ij}(x)\rho(x) \frac{\partial q(x)}{\partial x_j} \right) \\ q(x)\Big|_{x\in\partial A} = 0\ ; \quad q(x)\Big|_{x\in\partial B} = 1 \end{cases} \tag{6.6}$$

The equation above is impossible to solve except for trivial cases. In fact, in general, it is a differential equation of $6N$ variables, with N the number of atoms. However an approximation to the committor function can be obtained with the use of a set of collective variables.

Let us assume that the committor is function only of the atomic positions and only through a set of n collective coordinates $\theta(r) = (\theta_1(r), \ldots, \theta_n(r))$ such that

$$q(x) \equiv q(r,p) \approx f(\theta_1(r), \ldots, \theta_n(r)) \tag{6.7}$$

where $f(\theta_1(r), \ldots, \theta_n(r))$ is an unknown function. The best approximation of the function f can be obtained by minimizing the following functional

$$I[f] = \int_{\mathbb{R}^N \mathrm{X} \mathbb{R}^N} dr\, dp\, e^{-\beta H(r,v)} |Lf(\theta(r))|^2 \tag{6.8}$$

where H is the Hamiltonian of the system and L is the differential operator of the Kolmogorov equation (Eq.(6.6)). Since $I \geq 0$ by definition, and $I = 0$ only if $f(\theta(r) = q(x)$, then the best approximation to $q(x)$ is the function $f(\theta(r))$ that minimize the functional of Eq.(6.8). By some algebra Eq.(6.8) can be transformed into

$$I[f] = \int_{\mathbb{R}^n} dz\, e^{\beta F(z)} \sum_{i,j=1}^{n} \frac{\partial f(z)}{\partial z_i} M_{ij}(z) \frac{\partial f(z)}{\partial z_j} \tag{6.9}$$

where z are the dynamical variable associated to the collective variables $\theta(r)$, i.e. a realization of $\theta(r)$. Eq.(6.9) has the following boundary conditions $f|_{z\in a} = 0$ and $f|_{z\in b} = 0$ where a and b are the representation of the set A and B in the space of the collective variables and

$$M_{ij}(z) = e^{\beta F(z)} \int dr\, e^{-\beta V(r)}\, \nabla\theta_i\, \nabla\theta_j\, \delta(\theta(r) - z) \tag{6.10}$$

is the metric tensor associated with the change from the space of the coordinates into the space of the collective variables.

The Euler-Lagrange associated with the minimization of Eq.(6.9) is

$$\begin{cases} 0 = \displaystyle\sum_{i,j=1}^{n} \frac{\partial}{\partial z_i} \left(M_{ij}(z) e^{-\beta F(z)} \frac{\partial f}{\partial z_j} \right) \\ f\Big|_{z\in a} = 0\ ; \quad f\Big|_{z\in b} = 1 \end{cases} \tag{6.11}$$

It is worth noticing that the equation above is n-dimensional, with n the number of the collective variables used. This is a gain with respect the $6N$ dimensions of Eq.(6.6), but to solve numerically Eq.(6.11) might result still impossible. Moreover, Eq.(6.11) contains terms, like $M_{ij}(z)$ and $F(z)$, which are not readily available. By resorting to stochastic calculus, we recognize that there is a dynamics equation associated to Eq.(6.11) (see Ref[71]) which is

$$\dot{z}_i(\tau) = -\sum_{J=1}^{n}\left(M_{ij}(z(\tau))\frac{\partial F(z(\tau))}{\partial z_j} - \beta^{-1}\frac{\partial M_{ij}(z(\tau))}{\partial z_j}\right) + \sqrt{2\beta^{-1}}\sum_{j=1}^{N} M_{ij}^{1/2}(z(\tau))\eta_j(\tau) \tag{6.12}$$

where $\eta_j(\tau)$ is a white noise such that $\langle \eta_j(\tau)\eta_j(\tau^{'})\rangle = \delta_{ij}\delta(\tau - \tau^{'})$ and τ is an artificial time. The introduction of an artificial time derives from the fact that the collective variables do not depend on the momenta. This means that Eq.(6.12) is the dynamical equation (in collective variable space) generating reactive trajectories with an associated committor $f(z)$ that satisfy Eq.(6.11). If the set of collective coordinates $\{\theta(r)\}$ is a good set of variables to describe the mechanism of the reaction, then this mechanism should be analyzed by the reaction given in the system defined by Eq.(6.12). As shown in the Ref.[71] in the limit of $\beta \to \infty$ the Eq.(6.12) can be written as

$$\dot{z}_i(\tau) = -\sum_{j=1}^{n} M_{ij}(z(\tau))\frac{\partial F(z(\tau))}{\partial z_j} \tag{6.13}$$

The solution of the equation above connects a saddle point of $F(z)$ to the two minima of $F(z)$.

In order to better understand the solution of the Eq.(6.11) is useful to recall the minimum energy path.The MEP in an energy landscape $V(x)$ in terms of Cartesian coordinates x is a path which connects two minima of $V(x)$ via a saddle point. This MEP corresponds to the steepest descent path on $V(x)$ from the saddle point. For our purpose it is better to parameterize the MEP by the curve $x(\alpha)$, where $\alpha \in [0,1]$ is the parameter that parameterize the curve. By definition the force $-\nabla V(x)$ is everywhere tangent to the MEP, this leads to

$$\frac{dx_k(\alpha)}{d\alpha} \;||\; \frac{\partial V(x(\alpha))}{\partial x_k} \tag{6.14}$$

with the boundary condition $x(0) = x_a$ and $x(1) = x_b$ where x_a and x_b are

the corresponding values of the coordinate x at the minimum of $V(x)$. In the space of the collective variables $z = \theta(x)$, supposing that passing from x to $z = \theta(x)$ is like a change of coordinate, from Eq.(6.14), let that $z(\alpha) = \theta(x(\alpha))$ and $V(x) = U(\theta(x))$, can be obtained

$$\frac{dz_i(\alpha)}{d\alpha} = \sum_{k=1}^{N} \frac{\partial\theta_i(x(\alpha))}{\partial x_k}\frac{dx_k(\alpha)}{d\alpha} \;||\; \sum_{k=1}^{N} \frac{\partial\theta_i(x(\alpha))}{\partial x_k}\frac{\partial V(x(\alpha))}{\partial x_k} = \sum_{j,k=1}^{N} \frac{\partial\theta_i}{\partial x_k}\frac{\partial\theta_j}{\partial x_k}\frac{U(z(\alpha))}{\partial z_j} \tag{6.15}$$

The same consideration about the MEP is valid for the free energy. In the same way one can obtain the minimum free energy path (MFEP). Replacing $U(z)$ with $F(z)$ and the tensor $\sum_k(\partial\theta_i/\partial x_k)(\partial\theta_j/\partial x_k)$ with the average M_{ij} given by Eq.(6.10), the Eq.(6.15) leads to

$$\frac{dz_i(\alpha)}{d\alpha} \;||\; \sum_{j=1}^{n} M_{ij}(z(\alpha))\frac{\partial F(z(\alpha))}{\partial z_j} \tag{6.16}$$

The solution $z(\alpha)$ of Eq.(6.16) gives the minimum free energy path. The MFEP is a very important path in a dynamical process because it is the most likelihood path of the transition between the states A and B. It is worth to note that the condition of the MFEP (Eq.(6.16)) corresponds to the Eq.(6.13) relative to the Euler-Lagrange equation.

Summarizing the solution of the Eq.(6.16) $z(\alpha)$ is the MFEP on $F(z)$. Along this special path of the free energy surface an approximation of the committor function can be obtained from Eq.(6.11). In Ref.[71] is given a procedure to evaluate the approximation of the committor function $f(z)$ around the MFEP. This approximation is obtained using the capability of foliation of the committor function. Indeed, the phase space can be divided in iso-surface with constant value of the committor function. The main property of these iso-surfaces is that they are not crossing each other. This means that the MFEP can be divided in iso-surface along which the value of the committor is the same for every point. Thus, the MFEP can be parameterized with a parameter $\alpha \in [0, 1]$. The conclusion is that along the MFEP the value of the approximation of the committor function $f(z(\alpha))$, as expressed in terms of collective variables, is such that

$$f(z(\alpha)) \approx \begin{cases} 0 & \text{if } \alpha < \alpha_s \\ 1/2 & \text{if } \alpha = \alpha_s \\ 1 & \text{if } \alpha > \alpha_s \end{cases} \tag{6.17}$$

where α_s is the value of the parameter at the saddle point. The Eq.(6.17) gives a posteriori criterion to evaluate the reliability of the approximation to express the committor function as a function of a set of collective variables. If the committor on the surface relative to the saddle point is equal to 1/2 then the choice of the collective variables is adequate to sample the dynamics of a reactive trajectory. The physical meaning of Eq.(6.17) is that the stable states are equally accessible from the transition state.

In Fig.(6.2) is reported the committor function along the MFEP and the corresponding pictorial view of the system. In the figure is reported a reactive trajectory that goes from the state A to the state B. With the dashed line is reported the iso-surface relative to the transition state. If a trajectory starts from the configuration relative to the transition state, it has the same probability to reach the state A rather than the B. This means that the committor has the value 0.5 for the transition state. While a trajectory that starts from a point after the saddle point, it reaches the state B. Thus, the value of the committor is 1. This is the third case of Eq.(6.17). Otherwise taking as starting configuration a point before the transition state, the trajectory reaches A and the corresponding value of the committor is zero.

2 Committor Analysis

As explained in the previous section the calculation of the committor on the iso-surface at the saddle point is an indicator of the goodness of the collective variables. It is worth to note that the transition state is identified as the saddle point of the free energy expressed in terms of collective variables. This means that the given transition state is a function of the collective variables, while the committor is a function of the coordinates and momenta of the atoms. As a consequence a transition state is represented with a set of atomic configurations that satisfy the conditions on the collective coordinates to be at the saddle point

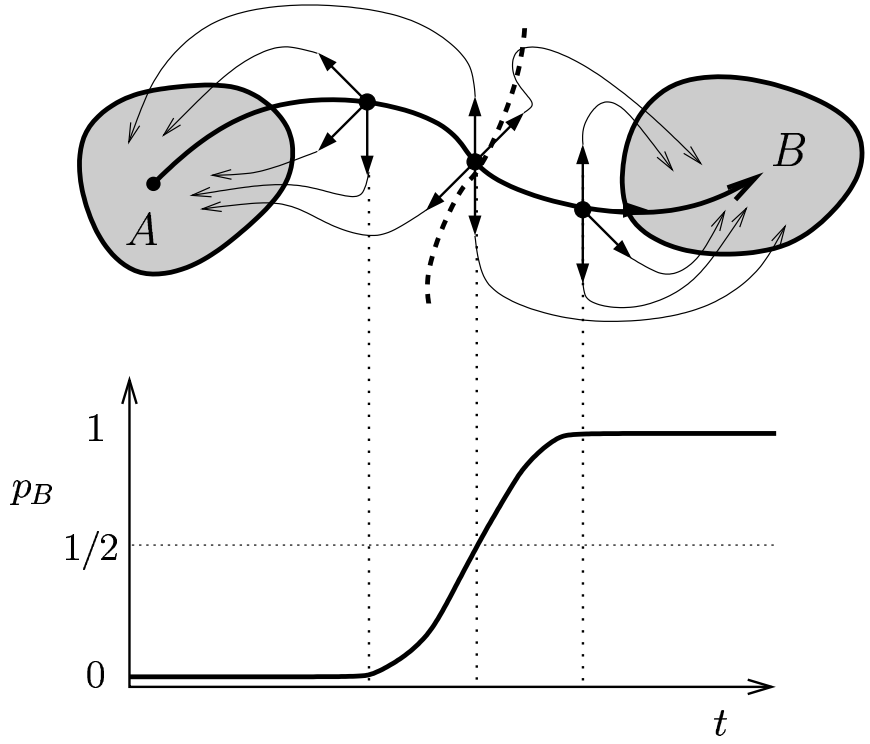

Figure 6.2: The committor as a function of time along a reactive trajectory. The portion of the phase space relative to the transition state is represented with a dashed line. The corresponding committor value is 1/2. While for points of the reactive trajectory before of the transition state the committor is zero, and for points after the transition state the committor has a unitary value. Figure taken from Ref.[74].

of the free energy. In other words there is not a bijection between the transition state identified with the collective variables and the relative atomic configurations which satisfy these collective variables. Thus, using molecular dynamic simulations we can not obtain the value of the committor function but we can evaluate the distribution of the committor.

The calculation of the committor distribution is a two steps process. The first step consists in the generation of a set of configurations for which is satisfied the restrain consistent with the saddle point. Then for each of these restrained configurations a set of unbiased simulations is performed with initial velocities

obtained from a Boltzmann distribution. The contribution to the distribution of the committor of a single restrained configuration is obtained counting the number of unbiased trajectories that reach B rather than A.

The distribution of the committor is a powerful analysis for discriminating coordinates that are able to drive a transition with those that are only correlated with it. The committor distribution relative to collective variables that are important from a dynamical point of view will be narrowly distributed around 1/2.

As an example, in Fig.(6.3) are shown three possible free energy landscapes. In this figure the energy landscapes are reported as a function of two collective variables. On the right panel are also reported the committor distributions for the maximum of the free energy as a function of only one of the coordinates. Suppose one wants to known if the coordinate q is a good collective coordinate for the three cases in exam. If the free energy in the space of the q coordinate has a maximum for $q = q^*$, one has to evaluate the corresponding committor distribution. In the case (a) the reaction is correctly described by the collective variable q, as a consequence the committor distribution is peaked at 1/2. Instead in the case (b) the coordinate q is not the only relevant coordinate in the dynamical process, but also q' plays a significant role. Indeed, in this case, the committor distribution is not peaked at 0.5 but it has a bi-modal shape. Finally, also in the case (c) q' plays a significant role in the reaction and q is not a good reaction coordinate. The corresponding committor distribution is flat and with the same value.

In the next section will be reported the results obtained for the committor distribution in the case of the $\mathcal{Q}_6$ collective variable.

3 Results

As explained in the Sec.(5), in the present calculations two meta-stable states, one crystalline and the other amorphous, are found for Si nano-particles embedded in a-SiO_2. In order to understand if the $\mathcal{Q}_6$ bond order parameter is a good reaction coordinate the committor distributions are analyzed. In the present case only one collective coordinate is used. Thus, the free energy profile is obtained as a function of only one coordinate. The ensemble of the transition state is given by the atomic configurations that satisfy the constrain on the $\mathcal{Q}_6$ relative to the

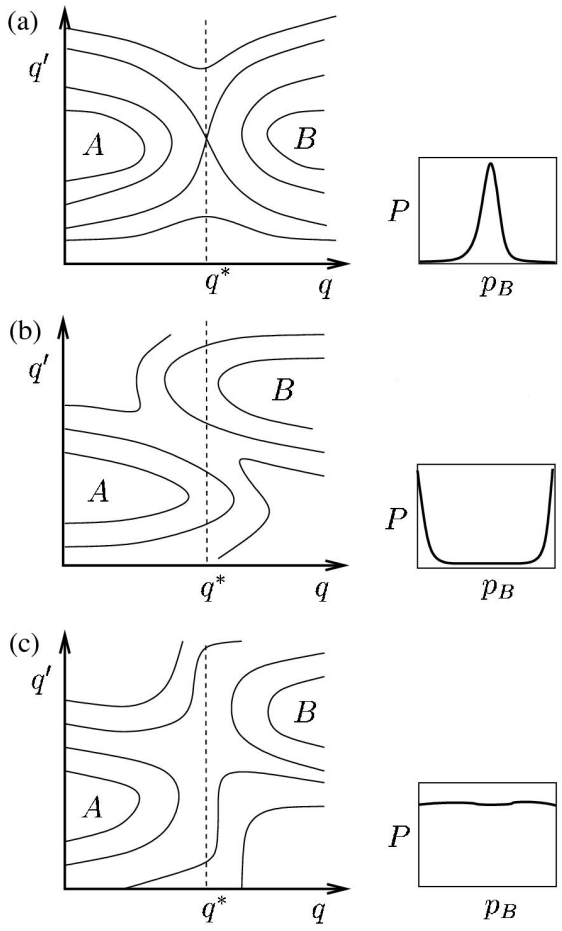

Figure 6.3: Three examples of free energy landscape of bi-stable systems. On the left is reported the energy landscape as a function of two collective variables. The collective coordinate q is able to reproduce the two basins of the free energy landscape for each of the three cases. The maximum of the free energy is obtained for the value $q = q^*$. On the right is reproduced the distribution of the committor for the maximum of the free energy as a function of only the coordinate q. Figure taken from Ref.[74].

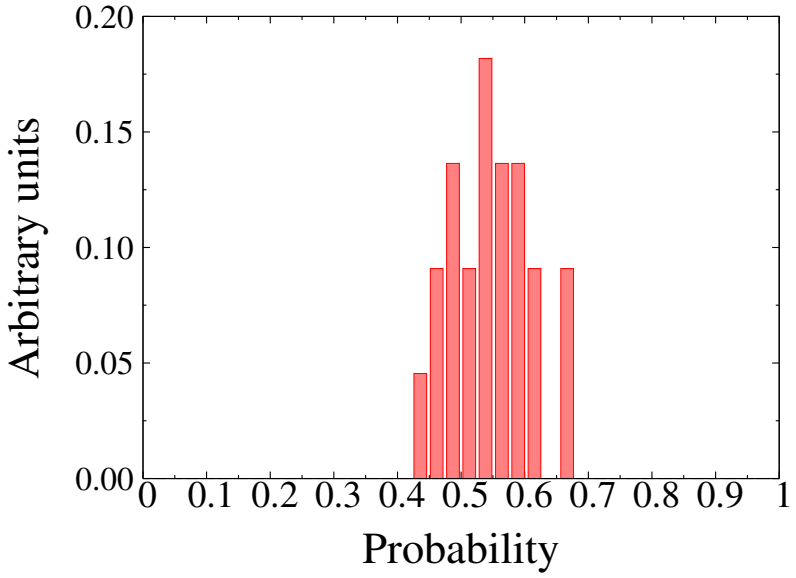

Figure 6.4: Committor distribution of the nano-particle of radius 1.3 nm evaluated at 1250 K. The distribution is relative to the transition ensemble given by $\mathcal{Q}_6 = 0.187$.

point of maximum of the free energy reported as a function of $\mathcal{Q}_6$.

The first step in the calculation of the committor distribution is the generation of a set of configurations relative to the iso-committor surface of the saddle point of the energy landscape. In the present case the transition state is represented by the maximum point in the free energy profiles of Fig.(5.10). This means that the distribution of the committor should be evaluated for the configurations that satisfy the requirement $\mathcal{Q}_6 = \mathcal{Q}_6^{max}$ where $\mathcal{Q}_6^{max}$ is the value of $\mathcal{Q}_6$ for which there is a maximum of free energy.

It is worth to note that the points in the Fig.(5.10) represent the value of $\mathcal{Q}_6$ for which the free energy is calculated through the combination of restrained MD and parallel tempering method, as explained in Sec.(2). Thus, the configurations in the trajectories used for the calculation of the integral in Eq.(5.8) compose a good transition ensemble from which the committor distributions can be evaluated.

Due to the interval between the points in the curves of Fig.(5.10) it is possible

that the maximum in the free energy does not correspond to a value of $\mathcal{Q}_6^*$ used in the calculation of the free energy (i.e. the values of $\mathcal{Q}_6$ reported in the figure). In other words, the chosen values of $\mathcal{Q}_6$ used to restrain the MD for the evaluation of the free energy may be not corresponding to a maximum in the free energy. In order to remedy to this drawback the value of $\mathcal{Q}_6^{max}$ is estimated through a fitting procedure. The free energy profiles as functions of $\mathcal{Q}_6$ are fitted with a cubic spline. The point of maximum in the free energy is obtained by this extrapolation. Then a set of configurations relative to the extrapolated value of $\mathcal{Q}_6^{max}$ are simulated imposing the restrain $\mathcal{Q}_6 = \mathcal{Q}_6^{max}$. These new configurations are our best approximation to the transition ensemble.

Due to the very high computational effort needed by the evaluation of the committor distribution, it is evaluated only for a single temperature for each dimension of the Silicon nano-particle. The distributions are evaluated at a temperature high enough to eliminate possible biases due to poor sampling.

In the case of the nano-particle of radius 1.3 nm. The temperature of the analysis is 1250 K. The maximum of the free energy, as obtained with the extrapolation procedure, is located at $\mathcal{Q}_6 = 0.187$. A set of configurations that satisfy this restrain is obtained starting from the trajectories used to evaluate the free energy profile with the $\mathcal{Q}_6^*$ closer to 0.187 and imposing the new restrain. These configurations can be used as starting points of the committor analysis. Thirty different configurations are extracted from the transition ensemble. Their committor value is computed from 100 trajectories generated from each configuration by assigning initial random momenta distributed as a Boltzmann distribution. The committor distribution is evaluated counting the number of trajectories, for every starting configuration, that reaches the crystalline state rather than the amorphous.

In Fig.(6.4) is reported the resulting distribution. Useful informations can be extracted both from the shape of the curve and from the location of the peak. The shape of the distribution is good because it is single peaked. This is an indicator of the fact that in this case the $\mathcal{Q}_6$ is able also to give information on the dynamic of the transition. Moreover the peak is centered around 0.55. This means that the hyper-surface chosen as transition state is a good approximation of the iso-committor 1/2 surface.

It is worth noticing that the distribution of the committor for the transition

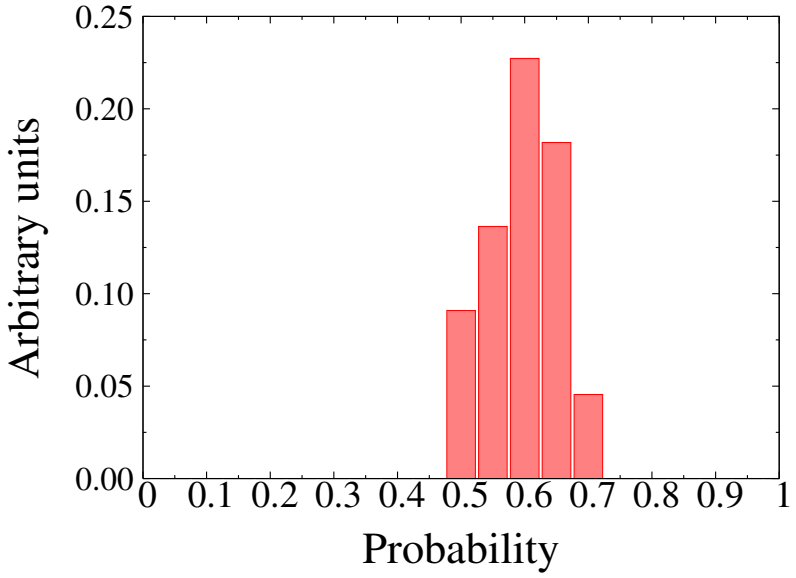

Figure 6.5: Same as Fig.(6.4) except that the transition ensemble s given by $\mathcal{Q}_6 = 0.19$.

ensemble obtained without the extrapolation procedure of the maximum of the free energy leads to worse results. Indeed, the distribution of the transition ensemble given by $\mathcal{Q}_6^{max} = 0.19$, which is the closest $\mathcal{Q}_6^*$ used in the calculation of the free energy profile, is reported in Fig.(6.5). While the distribution exhibits a single peak as before, in this case the distribution is centered at higher values. Indeed the peak is further from 1/2. This means that this transition ensemble is a worse approximation than the one obtained with the procedure of the extrapolation of the maximum. However, from the distribution of Fig.(6.5) a further confirm of the reliability of the $\mathcal{Q}_6$ as collective variable can be achieve. Indeed, the committor distribution of Fig.(6.5) is obtained from an approximation of the transition state that is closer to the crystal state than in the previous case. As explained before the value of the committor gives the probability to reach the crystalline state rather than the amorphous, it is a quantitatively indicator of the progress of a reaction. This means that the probability to reach the crystal state should be higher for state close to the crystal state. In fact, in Fig.(6.5) the distri-

bution of the committor is peaked at higher value than the curve of Fig.(6.4). In other words, the committor, hence the probability to reach the product, is higher for the state closer to the product. This is what one expects from a reaction coordinate.

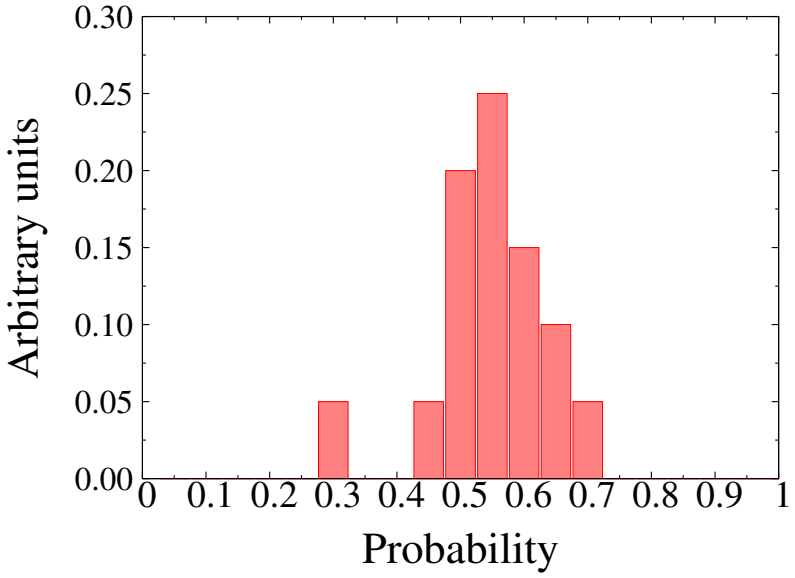

Figure 6.6: Committor distribution for transition state given by $\mathcal{Q}_6 = 0.11$ for the nano-particle of radius 0.8 nm at 1500 K.

The same conclusion on the reliability of the $\mathcal{Q}_6$ as collective variable holds true in the case of the nano-particle of smaller size (radius of 0.8 nm). In this case the committor is analyzed at 1500 K, which is relative to the free energy profile reported with a line and triangles in Fig.(5.10). The maximum of the free energy is obtained for $\mathcal{Q}_6 = 0.11$ and its distribution of the committor is reported in Fig.(6.6). In the present case the distribution is even better peaked. Indeed the maximum of the curve is closer to the 0.5 than the previous case.

For the larger nano-particle, the distribution of the committor is reported in Fig.(6.7). In this case the distribution is not so good than for the smaller nano-particles. Indeed, the distribution is double peaked. Moreover there is any peak around 1/2. This means that in the case of large nano-particles the $\mathcal{Q}_6$ does not

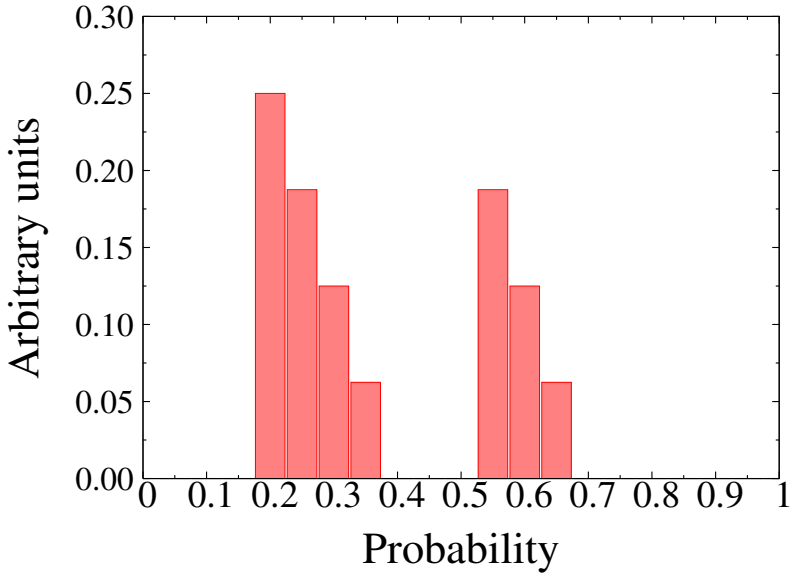

Figure 6.7: Committor distribution for transition ensemble given by $\mathcal{Q}_6 = 0.155$ for the nano-particle of radius 1.8 nm at 1500 K.

describe the dynamical process completely. In this case there is another slow coordinate that is relevant in the dynamical process and the $\mathcal{Q}_6$ parameter is not enough to obtain dynamical information on the process.

The analysis of the committor distributions can lead to useful informations on the mechanism of the nucleation of the Silicon nano-particles. This suggests that the mechanism process of the nucleation depends on the size of the nano-particle. It is important to stress that the $\mathcal{Q}_6$ bond order parameter is a global order parameter. In the sense that it depends on the overall order of the system. In the case of confined systems (the small nano-particles) the $\mathcal{Q}_6$ is a good collective coordinate. This suggests that the nucleation takes place as a homogeneous process. In other words all the regions of the nano-particle become crystalline at the same time without any point of aggregation.

Instead for bulk systems, the large nano-particle, has been revealed that the only $\mathcal{Q}_6$ is not sufficient to describe the process of nucleation completely. This leads to the conclusion that the nucleation mechanism for bulk system is different

and that it is not a homogeneous process. In fact the $\mathcal{Q}_6$ is not able to identify possible nucleation sites. As a consequence of the global nature of the bond order parameters, $\mathcal{Q}_6$ is not able to discern a large crystal cluster from two little ones inside the nano-particle. For example, a nano-particle with a large portion of crystalline core and another with two little crystalline regions could have the same value of $\mathcal{Q}_6$. Thus, the $\mathcal{Q}_6$ parameter is not a good collective coordinate for heterogeneous nucleation.

This is an important difference which is useful to better understand the nucleation process. Indeed the above-quoted $\mathcal{Q}_\ell$ bond order parameters are often used to study the mechanism of nucleation in bulk system, like in Refs.[55, 56], where Frenkel and collaborators studied the nucleation of a Lennard-Jones system driving the MD with $\mathcal{Q}_\ell$ bond order parameters. In the case of bulk system one has to take in account that the $\mathcal{Q}_\ell$ are not good collective coordinates and the dynamical informations may be misleading.

Once demonstrated the reliability of the $\mathcal{Q}_6$ used as collective variable, the free energy barriers of the phase transition from crystalline to amorphous nano-particles can be evaluated from Fig.(5.10). The energetic barriers for Si nano-particles of different size are reported in Fig.(6.8) as functions of the temperature. The barriers are defined by the difference between the free energies of the transition state (TS) and of the most stable state. As clearly shown in the figure the energetic barrier depends on the temperature. The energetic barrier decreases with the temperature for each of the three sizes of the nano-particle.

Moreover in the figure are reported the free energy difference between the transition state and a single meta-stable state. The barriers relative to the amorphous state are reported with a dashed line, while with the dotted line are reported the energetic differences of the crystal phase and the transition state. The temperature of inversion of stability between the amorphous and the crystal phase can be estimated from the intersection of the two curves. As shown in the figure, for small nano-particles, the temperature of inversion raises with the size of the nano-particle. Indeed, in both cases of small nano-particles (Radius = 0.8, 1.3 nm) the inversion of stability takes place between the last two temperatures reported in the figure. For the smallest the T of inversion is very near to 1500 K, while for the particle with a radius of 1.3 nm is about 1100 K. Finally for the largest nano-particle the temperature of inversion of the phase is about 1400 K. However,

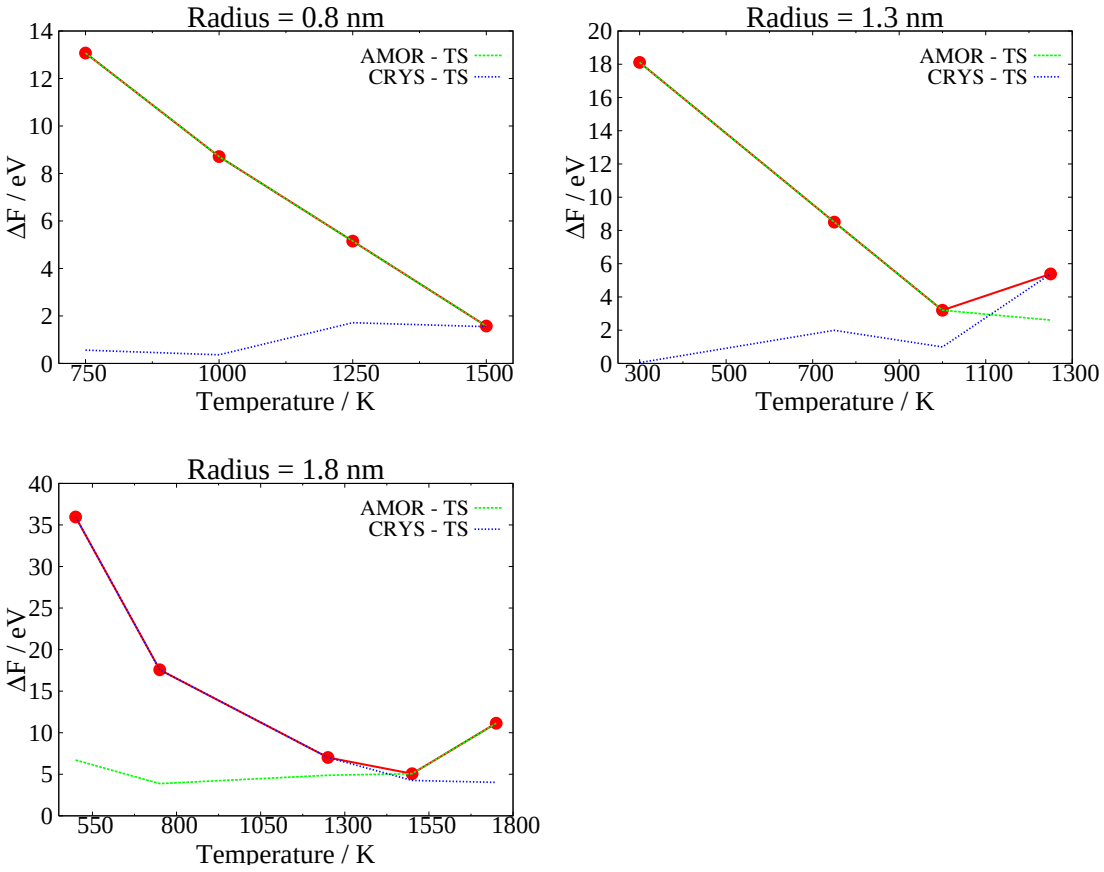

Figure 6.8: Free energy barriers of the transition from crystalline to amorphous phase of Si nano-particle embedded in a-SiO_2 for different size of the nano-particle (Radius = 0.8, 1.3, 1.8 nm). The barriers are relative to the difference between the free energy of the transition state and the most stable state of the profiles reported in Fig.(5.10). Moreover, with a dashed line is reported the free energy difference between the transition state and the amorphous phase. While the dotted lines shows the free energy differences between the crystalline and the transition state.

it is worth to stress that the free energy barriers for large nano-particles have to be take in account with the adequate precaution because we know that the $\mathcal{Q}_6$ is not the only relevant collective coordinate in the present physical process.

Chapter 7

Hydrodynamic Evolution of an Interface from Statistical Mechanics

In order to model phenomena in the hydrodynamic limit, i.e. when the scale length and time are much longer than the characteristic atomistic value, continuum theory have been developed. The continuum equations are derived from conservation laws such that mass, momentum and energy conservation, in combination with phenomenological laws of transport. The equations of transport are characterized by the transport coefficients, like diffusion coefficient in the case of mass transport or viscosity and thermal conductivity in the case of momentum and heat transport. The transport coefficients are phenomenological quantities depending on the nature and the conditions of the system. The validity of the continuum theory of the hydrodynamic is limited by the knowledge of these transport coefficients.

A fundamental question which is still open is the validity of the hydrodynamic description at the nanometric scale. An atomistic model of the hydrodynamic should be overcome the limitations of the continuum theory. In the 1950 Irving and Kirkwood [75] derived the atomistic theory of the hydrodynamic by means of the classical statistical mechanics.

An atomistic model of hydrodynamic deal with non equilibrium statistical mechanics. Since molecular dynamic provide a powerful tool to sample ensemble average from a system at equilibrium. This is ensured by the ergodic theorem

that justified the use of time average in place of ensemble average. In the case of non-equilibrium dynamics the situation is much complex. In the non-equilibrium processes the use of time average is not justified except in the case of a linear response [76] to an external field or for stationary non-equilibrium process [77].

The case of the evolution of an interface between two immiscible liquids is an example of non-equilibrium process that is not included nor in the case of the linear response neither in the case of stationary non-equilibrium. The hydrodynamic evolution of an interface is a genuine non-equilibrium process.

In this chapter will be presented a method for studying the evolution of an interface between two immiscible liquids. The chapter is organized as follows. In Sec.(1) an atomistic definition of the hydrodynamic variables is given. Then in Sec.(2) a method for evaluating non-equilibrium ensemble average will be exposed. In the following section the application of the method in the case of the evolution of an interface will be presented. The final section is reserved to the results.

1 Theoretical Background

Let consider a system composed by N particles. Let $\vec{r}_i$ and $\vec{p}_i$ be the position and the momenta, respectively, of the i-th particle and $\Gamma=\{\vec{r}_i, \vec{p}_i\}$ be a point in the phase space. In statistical mechanical theory the expectation value of any macroscopic dynamical variable $\mathcal{O}(\Gamma, t)$ is given by an ensemble average over the phase space of the corresponding microscopic observable $\hat{\mathcal{O}}((\Gamma, t)) = \sum_{i=1}^{N} \mathcal{O}_i(\Gamma)\delta(\vec{r}_i - \vec{r})$ that is given by

$$\mathcal{O}(\Gamma, t) = \int_{\mathbb{R}^{6N}} d\Gamma \; \hat{\mathcal{O}}(\vec{r}, \Gamma) \; w(\Gamma, t) \equiv \langle \hat{\mathcal{O}}(\vec{r}, \Gamma), \; w(\Gamma, t) \rangle \tag{7.1}$$

where $w(\Gamma, t)$ is the normalized probability density. Hereafter $\langle \mathcal{O}, w \rangle$ denotes the expectation value of a given observable $\mathcal{O}$ of a distribution w. It is simply the inner product of $\mathcal{O}$ and w over phase space.

Irving and Kirkwood express the dynamical variables concerned in the equations of hydrodynamics as expectation values over an ensemble having w as distribution function [75]. First they defined the density field starting from the consideration that the probability per unit of volume that the i-th molecule is at

$\vec{r}_{\,i}$ is

$$\int \dots \int d\vec{r}_{\,1} \cdots d\vec{r}_{\,i-1}\, d\vec{r}_{\,i+1} \cdots d\vec{r}_{\,N}\; d\vec{p}_{\,1} \cdots d\vec{p}_{\,N}\; w(\Gamma;t) \tag{7.2}$$

where the integrals are over all the position vectors except $\vec{r}_{\,i}$ and over all momenta. Note that the integral above is $6N-3$ dimensional. Introducing the Dirac's delta function, the probability per unit volume that the i-th molecule is at $\vec{r}$ at time t is

$$\langle \delta(\vec{r}_{\,i} - \vec{r}\,), w(t) \rangle = \int_{\mathbb{R}^{6N}} d\Gamma\; \delta(\vec{r}_{\,i} - \vec{r}\,)\; w(\Gamma;t) \tag{7.3}$$

Thus, the total mass density at $\vec{r}$ and at time t is given by

$$\rho(\vec{r}\,;t) = \sum_{i=1}^{N} m_i \langle \delta(\vec{r}_{\,i} - \vec{r}\,), w(t) \rangle \tag{7.4}$$

The equation above defines the macroscopic density field.

The mean momentum of the i-th particle, providing that it is in $\vec{r}$ while the positions of the others particle remain undefined, is given by

$$\frac{\displaystyle\int_{\mathbb{R}^{6N}} d\Gamma\; \vec{p}_{\,i}\; \delta(\vec{r}_{\,i} - \vec{r}\,)\; w(\Gamma,t)}{\displaystyle\int_{\mathbb{R}^{6N}} d\Gamma\; \delta(\vec{r}_{\,i} - \vec{r}\,)\; w(\Gamma,t)} = \frac{\langle \vec{p}_{\,i}\; \delta(\vec{r}_{\,i} - \vec{r}\,), w(\vec{r}\,;t) \rangle}{\langle \delta(\vec{r}_{\,i} - \vec{r}\,), w(\vec{r}\,;t) \rangle} \tag{7.5}$$

This means that the factor $\langle \vec{p}_{\,i}\, \delta(\vec{r}_{\,i} - \vec{r}\,), w(\vec{r}\,;t) \rangle$ is the product of the mean momentum by the probability per unit of volume that the particle i is at $\vec{r}$. In other words it is the contribution of the particle i to the total momentum. The total momentum density at $\vec{r}$ is obtained simply summing the contribution of all particles, which leads to

$$\vec{v}\,(\vec{r}\,;t) = \frac{\displaystyle\sum_{i=1}^{N} \langle \vec{p}_{\,i}\; \delta(\vec{r}_{\,i} - \vec{r}\,), w(t) \rangle}{\rho(\vec{r}\,;t)} \tag{7.6}$$

where $\vec{v}\,(\vec{r}\,;t)$ is the velocity field at $\vec{r}$.

Once defined the density and the velocity field, the temperature field can be defined as

$$T(\vec{r}\,;t) = \frac{1}{2mk_B} \frac{\displaystyle\sum_{i=1}^{N} \langle \Big[\vec{p}_{\,i} - m\vec{v}\,(\vec{r}\,;t)\Big]^2 \delta(\vec{r}_{\,i} - \vec{r}\,), w(t) \rangle}{\rho(\vec{r}\,;t)} \tag{7.7}$$

where k_B is the Boltzmann constant. Note that in the equation above the $\vec{p}_i$ is the momentum of the particle i, while $\vec{v}(\vec{r};t)$ is the velocity field as given by Eq.(7.6). Thus the temperature field is given by the square of the difference between the momentum of a given particle minus the global momentum of all the particles given by the velocity field.

Moreover the energetic fields can be defined. The kinetic energy of the i-th particle is given by $\vec{p}_i^{\,2}/2m_i$. While the contribution to the kinetic density given that the particle is at $\vec{r}$ is given by the term $\langle(\vec{p}_i^{\,2}/2m_i)\delta(\vec{r}_i - \vec{r}), w(t)\rangle$. The total kinetic energy density is obtained by the sum of the contribution of all the particles, this leads to the following expression

$$E_K(\vec{r};t) = \sum_{i=1}^{N} \langle \frac{\vec{p}_i^{\,2}}{2\,m_i}\, \delta(\vec{r}_i - \vec{r}), w(t)\rangle. \tag{7.8}$$

As regards to the potential energy, suppose that there is no external force on the system, consequently the potential energy of the system is given only by the mutual interaction energy between the particles. Under this condition the potential energy of the system can be express like a sum of two body contributions $1/2\sum_{i=1}^{N}\sum_{j\neq i}^{N} V_{ij}$. The total interaction potential energy density at $\vec{r}$ is given by

$$E_V(\vec{r};t) = \frac{1}{2}\sum_{i=1}^{N}\sum_{j\neq i}^{N} \langle V_{ij}\, \delta(\vec{r}_i - \vec{r}), w(t)\rangle. \tag{7.9}$$

The expression of the total energy density at $\vec{r}$ can be obtained simply summing the contribution of the kinetic and the potential energy density. That leads to

$$E_T(\vec{r};t) = E_V(\vec{r};t) + E_K(\vec{r};t). \tag{7.10}$$

In such way a exhaustive definition of the dynamical fields concerning the hydrodynamics are introduced on the base of the statistical mechanic theory. These quantities are key observables to compute during a hydrodynamic simulation. In the next section a method to compute this quantity in the case of non equilibrium dynamic is exposed.

2 Non Equilibrium Molecular Dynamic

The statistical properties of a non-stationary system out of equilibrium can be obtained with the dynamical approach to non-equilibrium molecular dynamic (NEMD) [78, 79, 80]. Within this method rigorous ensemble average of a microscopic observable can be obtained by taking an average over the initial ensemble of the observable evolved in time under a perturbed dynamic. The basic theory of the method is the following.

Supposing to compute the response for a given property of a system to a Hamiltonian perturbation. The total Hamiltonian H of the system can be defined as a sum of the standard equilibrium Hamiltonian $H_0 = K + V$ plus a perturbing term H_P

$$H = H_0 + H_P \tag{7.11}$$

where the perturbing term is given by

$$H_P = -A(\Gamma)\ \psi(\Gamma, t) \tag{7.12}$$

where A is a suitable local property coupling the system with an external local field $\psi(\Gamma, t)$.

The dynamic corresponding to the total Hamiltonian is given by

$$\begin{cases} \dot{\vec{r}} & = \frac{\partial H_0}{\partial \vec{p}} + \frac{\partial H_P}{\partial \vec{p}} = \frac{\vec{p}}{m} - \frac{\partial A}{\partial \vec{p}}\psi(t) \\ \dot{\vec{p}} & = -\frac{\partial H_0}{\partial \vec{r}} - \frac{\partial H_P}{\partial \vec{r}} = F + \frac{\partial A}{\partial \vec{r}}\psi(t) \end{cases} \tag{7.13}$$

The probability density associated to the dynamic of Eq.(7.13) is the solution of the Liouville equation

$$\frac{\partial w}{\partial t} = i\mathcal{L}(t)w = (i\mathcal{L}_0 + i\mathcal{L}_P)\, w = \{H, w\} \tag{7.14}$$

where $\{H, \cdots\}$ are the Poisson bracket and $i\mathcal{L}(t) \equiv \{\cdots, H(\vec{r}, \vec{p})\}$ is the Liouville operator.

A formal solution of the Eq.(7.14) is given by

$$w(\Gamma, t) = \mathcal{S}^{\dagger}\ w(\Gamma, 0) \tag{7.15}$$

where $\mathcal{S}^{\dagger}$ is the adjoint of the time evolution operator of the dynamic of Eq.(7.13). This means that an observable of the system evolves with $\mathcal{O}(t) \equiv \mathcal{O}(\vec{r}(t), \vec{p}(t)) = \mathcal{S}(t)\mathcal{O}(\Gamma, 0)$

The operator $\mathcal{S}^\dagger$ satisfies the Dyson equation

$$\mathcal{S}^\dagger(t) = \mathcal{S}_0^\dagger + \int_0^t d\tau\ \mathcal{S}^\dagger(t-\tau)\ i\mathcal{L}_P(\tau)\mathcal{S}^\dagger(\tau) \tag{7.16}$$

This can be simply verified substituting Eq.(7.15) into Eq.(7.14).

Assuming that at the initial instant $t = 0$ the system is at equilibrium with $w(\Gamma, t = 0) = w_{eq}(\Gamma)$, the time dependent non-equilibrium average of any observable that evolves like $\hat{\mathcal{O}}(t) = \mathcal{S}(t)\hat{\mathcal{O}}$ can be obtained as follows

$$\begin{aligned} \mathcal{O}(t) = \langle\hat{\mathcal{O}}\rangle_{NE} = \int d\Gamma\ \hat{\mathcal{O}}(\Gamma)\ w(\Gamma,t) \equiv \Big(\hat{\mathcal{O}}, \mathcal{S}^\dagger(t) w_0\Big) = \\ = \Big(\mathcal{S}(t)\hat{\mathcal{O}}, w_{eq}\Big) \equiv \langle\mathcal{S}(t)\hat{\mathcal{O}}\rangle_{eq} \end{aligned} \tag{7.17}$$

where $(\cdots, \cdots)$ denotes the ensemble average of the scalar product and the property of the scalar product $(\hat{O}\psi, \phi) = (\psi, \hat{O}^\dagger\phi)$ is used. The Eq.(7.17) is the Onsager-Kubo equation. It is of fundamental importance to understand a non-equilibrium dynamic. The meaning of Eq.(7.17) is that for system initially at equilibrium the non equilibrium properties can be obtained as an average over the equilibrium ensemble of the observable evoluted with the full dynamic. In other words the non-equilibrium properties can be computed using equilibrium average according to evolve the system with the full dynamic.

The computational procedure is to chose some independent configurations of the system in a steady state then a non-equilibrium dynamic is started from each of these configurations. Along the perturbed trajectories the microscopic observables is evaluated. A macroscopic field is an ensemble average of a microscopic observable over all the perturbed trajectories. In the Fig.(7.1) a pictorial view of the method is reported. In the figure is shown the stationary MD trajectory from which a set of configurations, i.e. the point along the trajectory, is chosen as starting points for non-equilibrium dynamics.

3 Hydrodynamic Evolution of an Interface

In the present case the relaxation of an interface between two immiscible liquids is analyzed. In order to define an interface between the liquids a discrete decomposition of the sample is done. Suppose to divide the sample in M cells. In such

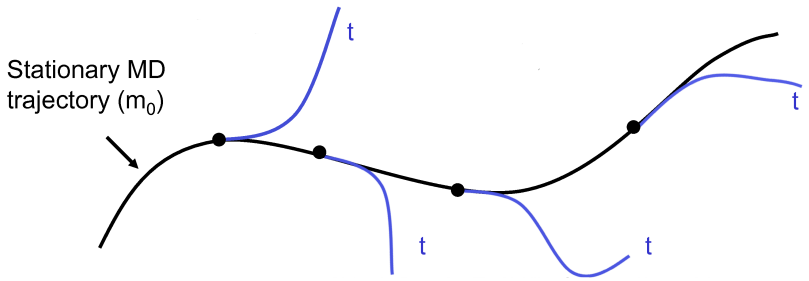

Figure 7.1: Pictorial example of a NEMD simulation. The stationary MD trajectory is reported with a black line. The point along the trajectory are the starting points for a set of non-equilibrium dynamics which are represented with the blue lines. The expectation value of an observable is evaluated as an average over the non-equilibrium trajectories.

a way the simulation box is composed by a grid of M points. Each of these points represents a cell.

Let $\vec{x}_\alpha$ define a grid point of the simulation box, in the discretized representation the microscopic observable $\hat{\mathcal{O}}$ in the cell α is given by

$$\hat{\mathcal{O}}(\vec{x}_\alpha;\vec{r}\,,\vec{p}\,) = \frac{1}{\Omega_\alpha}\int_{\Omega_\alpha} d\vec{x}\,\sum_{i=1}^{N}\delta(\vec{x}-\vec{r}_{\,i})\;\mathcal{O}_i(\vec{r}\,,\vec{p}\,) \tag{7.18}$$

where Ω_α is the volume of the cell α. Note that in the equation above the sum runs over all the atoms and the delta function selects only the atoms which reside inside the cell α.

As explained in the previous section the time evolution of an observable is evaluated from an ensemble average on an initial condition of the system (see Eq.(7.17)). The present initial condition is such that a non flat interface is defined between the two liquids. In order to define the interface in the discretized representation of the system, the difference of the density of the species inside the cell is analyzed.

The $\Delta\rho$ of a cell α is simply given by the difference of the density of the specie A and the density of the specie B inside the cell $\Delta\rho(\vec{x}_\alpha) = \rho^A(\vec{x}_\alpha) - \rho^B(\vec{x}_\alpha)$, where

the densities are defined, according to the Eq.(7.18), as

$$\rho(\vec{x}_\alpha;\vec{r}\,,\vec{p}\,) = \frac{1}{\Omega_\alpha}\int_{\Omega_\alpha} d\vec{x}\sum_{i=1}^{N}\delta(\vec{x}-\vec{r}\,_i) \tag{7.19}$$

An interface between the two specie can be defined as the surface $\mathcal{S}$ on which $\Delta\rho = 0$. Thus the initial condition is given by

$$\Delta\rho(\vec{x}_\alpha; t=0) = \rho^A(\vec{x}_\alpha; t=0) - \rho^B(\vec{x}_\alpha; t=0) = 0 \tag{7.20}$$

for each cell α which belongs to the surface $\mathcal{S}$ (i.e. $\vec{x}_\alpha \in \mathcal{S}$).

In order to sample the initial condition a restrained MD is used. In such way a biased term is added to the Hamiltonian. The total Hamiltonian is given by the sum of the original one plus the biased term, this leads to

$$H(\vec{r}\,,\vec{p}\,) = H_0(\vec{r}\,,\vec{p}\,) + \frac{k}{2}\sum_{\vec{x}_\alpha\in\mathcal{S}}\Delta\rho(\vec{x}_\alpha;\vec{r}\,)^2 \tag{7.21}$$

The sum of the perturbated Hamiltonian runs only on the cells which belong to the interface. There is no bias on the other cells of the system.

A macroscopic field $\mathcal{O}$ at time t can be evaluated with the Onsager-Kubo equation (Eq.(7.17)). In the present case the Onsager-Kubo equation for a field $\mathcal{O}$ in the cell β given the initial macroscopic condition of Eq.(7.20) is

$$\begin{aligned}\mathcal{O}(\vec{x}_\beta, t|\Delta\rho^0 = 0, \vec{x}_\alpha \in \mathcal{S}) &= \left\langle \mathcal{S}(t)\hat{\mathcal{O}}\right\rangle_{w_0} \\ &\equiv \left\langle \mathcal{O}(\vec{x}_\beta;\vec{r}\,(t),\vec{p}\,(r))\right\rangle_{w_0}\end{aligned} \tag{7.22}$$

where the notation $\mathcal{O}(\vec{x}_\beta, t|\Delta\rho^0 = 0, \vec{x}_\alpha \in \mathcal{S})$ is used to stress the fact that the observable depends parametrically on the initial condition $\Delta\rho^0 = 0$ on the cells at the interface. The average on the equation above is explicitly given by

$$\begin{aligned}&\left\langle \mathcal{O}(\vec{x}_\beta;\vec{r}\,(t),\vec{p}\,(r))\right\rangle_{w_0} = \\ &= \int d\vec{r}\,^0 d\vec{p}\,^0\ \hat{\mathcal{O}}(\vec{x}_\beta;\vec{r}\,(r),\vec{p}\,(t))\ w_0(\vec{r}\,^0,\vec{p}\,^0|\Delta\rho^0 = 0, \vec{x}_\alpha \in \mathcal{S})\end{aligned} \tag{7.23}$$

where the integral is over the coordinations $\vec{r}\,^0$ and the momenta $\vec{p}\,^0$ of the initial configurations and w_0 is the probability density distribution of the initial

conditions of the system given that at the initial the system is in a canonical ensemble. The w_0 can be expressed as

$$w_0(\vec{r}^{\,0}, \vec{p}^{\,0} | \Delta\rho^0 = 0, \vec{x}_\alpha \in \mathcal{S}) = \frac{\exp(-\beta(\vec{r}^{\,0}, \vec{p}^{\,0})) \prod_{\vec{x}_\alpha \in \mathcal{S}} \delta(\Delta\hat{\rho}(\vec{x}_\alpha; \vec{r}^{\,0}))}{\mathcal{Z} P[\Delta\hat{\rho}(\vec{x}_\alpha; \vec{r}^{\,0}) = 0, \vec{x}_\alpha \in \mathcal{S}]} \tag{7.24}$$

where $\exp(-\beta(\vec{r}^{\,0}, \vec{p}^{\,0})$ is the probability density of the initial canonical ensemble, $\mathcal{Z}$ is the relative partition function and $P[\Delta\hat{\rho}(\vec{x}_\alpha; \vec{r}^{\,0}) = 0, \vec{x}_\alpha \in \mathcal{S}]$ is the probability that the system is in the given initial condition. The delta function means that contribute only the microscopic states for which $\Delta\rho(\vec{x}_\alpha; \vec{r}^{\,0}) = 0$.

Summarizing, the simulation of the evolution of the surface is performed averaging the surface computed on a given number of unbiased MD simulations started from point in the phase space extracted along a biased MD governed by the Hamiltonian of Eq.(7.21).

It is worth to note that the biased dynamic describe above may lead to an impulsive dynamic in the case of atoms which resides in the boundary of the cells. Suppose the case in which a atom i enters and exits from a cell during the biased dynamic. There is an impulsive force acting on it due to the derivative $\partial\Delta\rho/\partial\vec{r}_i$. This drawback is solved by approximating the Dirac's delta function $\delta(\vec{x} - \vec{r}_i)$ with a Gaussian function.

$$g(\vec{x} - \vec{r}_i) = \frac{1}{(2\pi\sigma^2)^{3/2}} \exp\left(\frac{-(\vec{x} - \vec{r}_i)^2}{2\,\sigma^2}\right) \xrightarrow{\sigma \to 0} \delta(\vec{x} - \vec{r}_i) \tag{7.25}$$

4 Computational Setup

In the present calculations the evolution of an interface between two immiscible Lennard-Jones liquids are evaluated.

The computational procedure can be summarized as follows. First a sample of a single specie of the chosen density is thermalized at a given temperature. Then the particles of the sample is differentiated in order to create an interface of a given shape between the two species. At this time the attractive part of the inter-specie interaction is suppressed and the restrained MD is performed in order to keep fix the interface between the liquids. Then unbiased simulation

are performed starting from initial configurations extracted by the biased trajectory. The macroscopic fields can be evaluated as an average over the unbiased trajectories.

In the present calculations the interaction is modeled by a Lennard-Jones potential. The interaction between particles of the same specie is described by a 6-12 Lennard-Jones potential with both the attractive and the repulsive part

$$V^{AA}(r) = V^{BB}(r) = \begin{cases} 4\epsilon \left[\left(\frac{\sigma}{r}\right)^{12} - \left(\frac{\sigma}{r}\right)^{6} \right] & \text{if } r < r_{cut} \\ 0 & \text{if } r > r_{cut} \end{cases} \tag{7.26}$$

where a cutoff radius r_{cut} is introduced in order to cut long range contribution. The cutoff radius is fixed at 3σ. While for the interaction between different species the attractive part is suppressed in order to take in account the immiscible nature of the liquids

$$V^{AB} = 4\epsilon \left(\frac{\sigma}{r}\right)^{12}. \tag{7.27}$$

The parameter of the potential is $\epsilon = 0.01032$ eV and $\sigma = 3.405$ Å. The masses are all unitary.

The first step of the procedure is the preparation of a well equilibrated sample at given density and temperature. The sample is composed of 171500 particles in a simulation box of $\sim$ 45 x 45 x 90 in units of σ. This correspond to a density of 1.024 particles$\cdot\sigma^3$. It is equilibrated at the temperature of 1.5 ϵ/k_B for 50 ps with a time step of $4.53 \cdot 10^{-3}$ τ in reduced units with $\tau \equiv \sigma(\epsilon/m)^{1/2}$. The condition of the simulation is chosen in accord to the phase diagram of the Lennard-Jones system [81], in order to ensure that in the given condition a LJ system is in the liquid phase. After the equilibration the pair correlation function of the sample is analyzed in order to check the phase of the system. The g(r) calculated correctly reproduces a pair distribution function of a Lennard-Jones liquid.

Then an interface is introduced in the sample by differentiating the specie of the particles. The particles of the two species are not different apart from their label. The interface is chosen such that divides the sample in two regions along the long direction of the sample, i.e. along the direction z. The shape of the interface is given by a sinusoid along one of the short direction, i.e. along x. In this kind of system the rule is to call perpendicular the long direction, i.e. z coordinate. While the directions parallel to the interface, i.e. x and

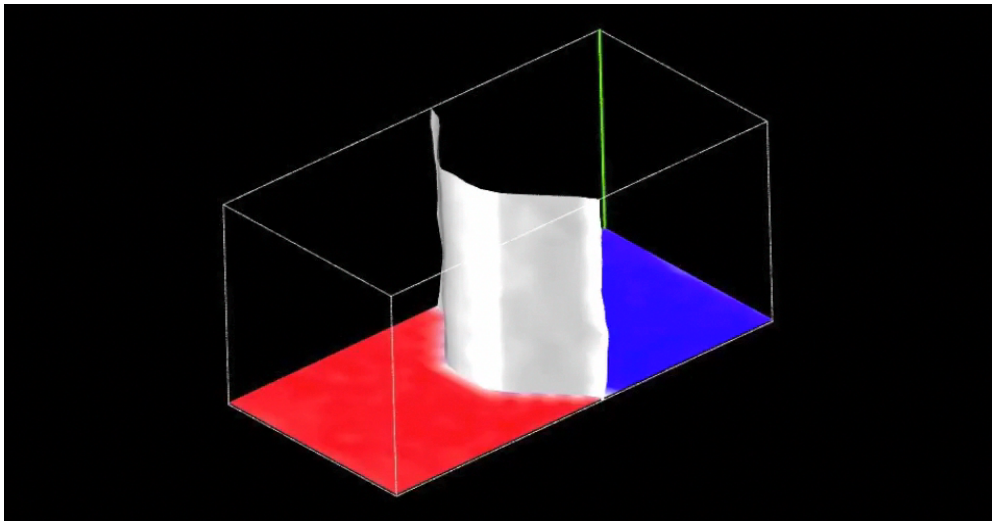

Figure 7.2: Initial restrained configuration at time $t = 0$. In the figure the total simulation box is reported. In the bottom of the box is shown the projection of the difference of the density fields of the two species. The red region corresponds to the region with $\Delta\rho > 0$. In other words the region with the specie A. While for the blue region $\Delta\rho < 0$, that corresponds to the region occupied by the particles of the specie B. The surface shown is the isosurface of $\Delta\rho = 0$ which corresponds to the interface between the liquids.

y in this case, are called the lateral coordinates. The shape and the position along the perpendicular direction of the interface is controlled with the function $\Theta(A(z - M_z/2) - \sin(k\pi x/M_x))$ where Θ is the Heaviside step function, z and x are the coordinates of a particle, M_z and M_x are the corresponding lengths of the simulation box, A is a parameter that controls the curvature of the interface and k gives the number of the nodes of the interface. The specie of the particle are chosen by the value of the Θ function, if $\Theta = 0$ the specie of the particle is A otherwise the specie is B. In the present calculation the parameter A is fixed at $\sim 17.6\ \sigma$ that correspond to a 1/5 of the perpendicular direction. While $k = 1$ corresponding to a single phase of the sinusoid. Finally an interface is created in the middle of the long direction. The final sample consists of 88889 particles of specie A and 82611 particles of specie B. The sample obtained is shown in Fig.(7.2).

At this point the sample is discretized into cells. The cell length is chosen such that at least thirty atoms are inside each cell. The resulting cell is a cubic box of length 3.22 σ. The grid consists of 14 x 14 x 28 points for a total of 5488 cells.

Now the biased MD is performed imposing the restrain that $\Delta\rho(\vec{x}) = 0$ for $\vec{x} \in \{\mathcal{S}(\vec{x}) : A(\vec{x}_z - L/2) + \sin(\pi\vec{x}_x/L) = 0\}$ where L is the cell length and $\vec{x}_\ell$ is the coordinate ℓ of the grid point $\vec{x}$. The restrained simulation needed a time step of an order of magnitude lower than the usual time step of a LJ system, so the time step is fixed at $4.53{\cdot}10^{-4}$ in reduced units. From the biased trajectory the starting configurations for the unbiased dynamics are extracted.

In order to take un-correlated starting configurations the auto-correlation function of the velocities for the restrained MD are evaluated. The auto-correlation function of the restrained MD goes to zero in about 50000 steps. Thus every 75000 steps of the restrained trajectory an unbiased MD simulation is started from the restrained configuration. The macroscopic fields are evaluated as average over forty unbiased configurations.

5 Results

The evolution of the interface is evaluated calculating the time evolution of the difference of the macroscopic density fields of the two species $\Delta\rho(\vec{x}_\alpha) = \rho^A(\vec{x}_\alpha) - \rho^B(\vec{x}_\alpha)$. The density fields are evaluated according to the Eq.(7.4). In Fig.(7.3) is reported the evolution of the interface at different time. As expected the interface become flat. The interface at the equilibrium is located on the plane that lie in the middle of the starting interface. Indeed the smoothness direction of the interface is opposite in the middle of the interface end at the periphery of the box, as clearly shown in Fig.(7.3). The time required for the smoothing of the interface is of about 35 ps. This means that the average velocity of the process is ~ 80 m/s.

The analysis of the perpendicular component of the velocities of all the atoms, given by

$$v^z_{A/B} = \frac{1}{N_{A/B}} \sum_{i=1}^{N_{A/B}} v^z_i \tag{7.28}$$

reveals that the interface relax at the equilibrium via a damped oscillation which

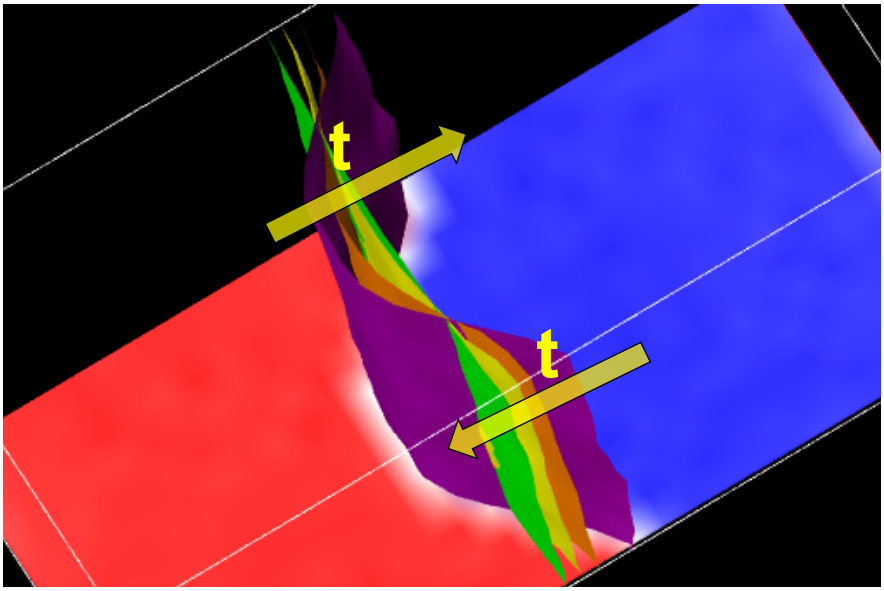

Figure 7.3: Time evolution of the interface between the immiscible liquids. At different times the interface is reported with different colors.

could be related to a pressure wave. In Fig.(7.4) is reported the component z of the velocities of all the atoms of the specie A and of the specie B. As shown in the figure the particles of the two species follow a synchronous damped oscillation.

The analysis of the macroscopic field of the velocity (see Eq.(7.6)) can give information about the mechanism of the smoothness of the interface. In Fig.(7.5) (top panel) is reported the projection of the velocity field in the plane perpendicular the interface, i.e. the x-z plane. The interface relaxes to the equilibrium through a convective flow from the center to the periphery of the interface. For clarity sake is reported only one slab of the velocity field and only the field relative to one specie. Note that the overall flow is symmetric with respect to the symmetry plane which divide transversely the plane of the figure. This means that the field of the present simulation respects the natural symmetry of the problem.

In the Fig.(7.5) (bottom panel) is reported the velocity field of a single unbiased trajectory. In other word the vector field not averaged over the unbiased trajectories, but the vector field given by

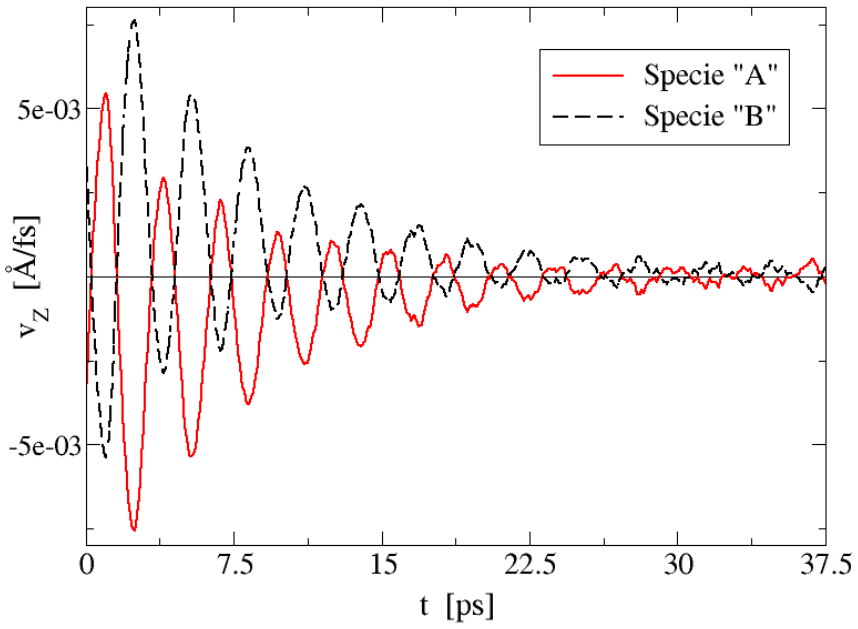

Figure 7.4: Time evolution of the component z (i.e. long direction) of the velocities for the particles of the specie A (continuous line) and for the particles of specie B (dashed line). The component z of the velocities are evaluated according to Eq.(7.28).

$$\vec{v}\,(\vec{x};t) = \frac{\vec{p}\,(\vec{x};t)}{\rho(\vec{x};t)}. \tag{7.29}$$

The velocity field of this single trajectory is quite different from the velocity field averaged over the unbiased trajectories. Indeed in this case the interface relaxes to the equilibrium through a flow that circles in anti-clockwise. It starts in the middle of the interface and ends in the top of the plane. It is important to stress that the single realization may not respect the symmetry of the problem. This means that the analysis of a single MD of a non-equilibrium process, even if locally mediated on time, may lead to misleading conclusions. It is important to stress this point because it is a common practice to study process of non-equilibrium averaging the observable on time [82, 83]. This technique should be used with caution because the present case is a typical example in which the

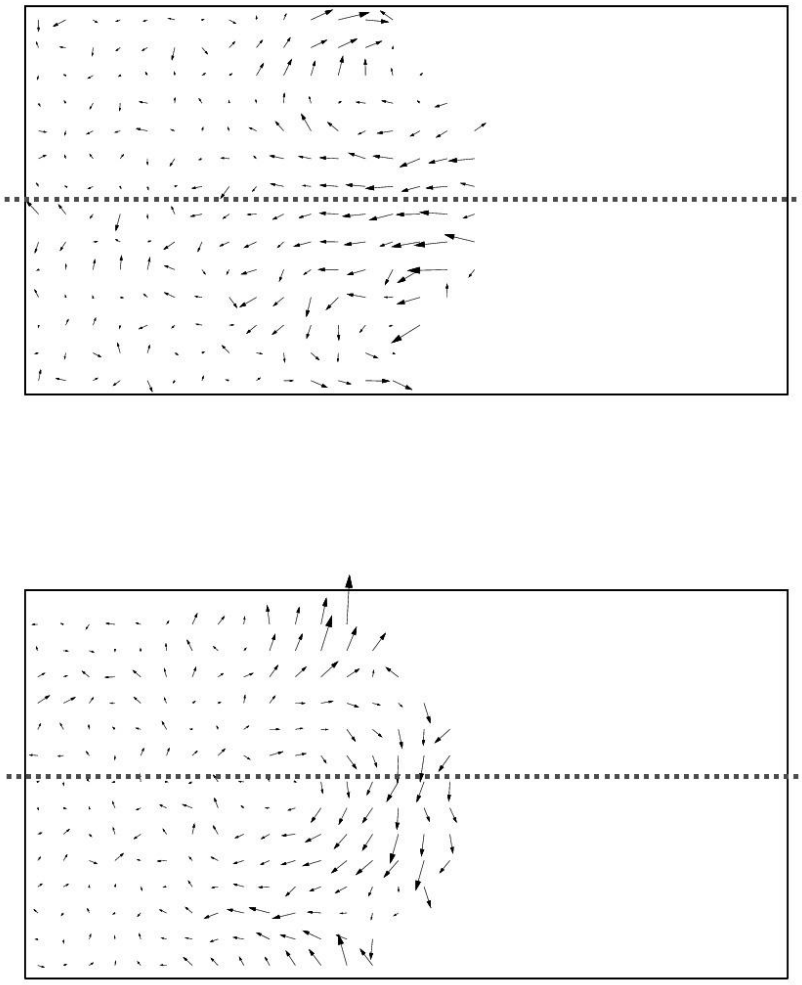

Figure 7.5: top panel) Projection along the x-z plane of the macroscopic velocity field for only the particles of specie A. Each vector is relative to a cell of the system. The velocity field are evaluated according to Eq.(7.6). The symmetry plane is also reported in the figure with a bold dashed line. bottom panel) Same as top panel except the fact that the velocity field is not averaged over the unbiased trajectories but it is relative to a single trajectory. In this case the velocity field is evaluated according to Eq.(7.29). In this case the natural symmetry of the system is not respected by the velocity field.

average on time may be not sufficient to describe the problem or in the worst case may lead to wrong results. Instead the D-NEMD approach described in Sec.(2) gives rigorous ensemble average that avoids this drawback.

Chapter 8

Conclusion

Nano-sized systems are attracting much interest as in many cases their properties are different, and improved, with respect to the bulk counterpart. However, in preparing such system it must be taken in account that also the phase diagram might strongly differ from the bulk case. This is the case of Si nano-particles embedded in amorphous silica. In fact at a variance from the Si bulk, the range of temperature in which the crystalline or the amorphous phase is the most stable depends on the size of the nano-particle. This fact is of paramount importance for developing new approach for the preparation of systems of well defined structural properties. Another relevant aspect to be considered in developing nano-sized systems is that their structural properties, and therefore possible also other properties (like photoluminescence, etc.), are not homogeneous within the particle. However, the origin of this inhomogeneity is not the presence of localized defect, rather the structure of the system changes continuously in going from the center to the periphery of the nano-particle. This is the result of the stress field induced by the presence of the amorphous embedding matrix. This suggest that on the one hand one have to take into account this inhomogeneity when designing a new system with tailored properties; on the other hand, it could be possible to introduce dopants to increase the "inertia" of the interface to the distortion induced by the matrix, so as to keep the structure homogeneous all over the nano-particle.

In Sec.(5) the phase diagram of Silicon nano-particles embedded in silica as a function of the size of the nano-particle and the temperature is reported. In small nano-particles the relative stability of disordered and ordered phase is inverted

with respect to the bulk. Indeed at lower temperature the most stable phase is the amorphous, while at high temperature the crystalline become the most stable. The phase diagram gives us informations about the mechanism of the formation of the nano-particles. Indeed the nano-particles are initially formed in the amorphous state not because this configuration is kinetically favored and the evolution to the crystalline state is observed at a temperature high enough to overcome the free energy barrier but because the amorphous state is the most stable. In this case the system is always in the thermodynamic equilibrium state.

On the basis of the results of Sec.5 a mechanism for interpreting the experimental results can be proposed. i) At lower annealing temperature the nano-particles are small (this is an experimental evidence) and amorphous as it is thermodynamically the most stable phase. ii) At higher temperatures there are two effects: on the one hand the temperature increases the size of the nano-particle and at this size (and temperature) the crystal phase is the most stable. However, in real sample the nano-particles do not have all the same size and some remain small. But, due to the inversion of stability in the small nano-particle, at the higher temperature the most stable phase is the crystal one. The mechanism is able to explain the experimental results that the fraction of amorphous nano-particles decrease with the temperature.

Moreover, the structural data of the Si nano-particles have been reported, demonstrating that the crystalline phase of small nano-particles is less ordered than the corresponding phase of larger nano-particles and that the degree of order decreases in going from the center to the surface of the nano-particle.

The bond orientational order parameter developed by Steinhardt *et al.* [47] has been used to obtain a free energy profile of the Si nano-particles as a function of the size of the nano-particle and the temperature. The $\mathcal{Q}_6$ has been revealed a good order parameter because it is able to discern the amorphous from the crystalline phase. In Sec.(6) the ability of $\mathcal{Q}_6$ also as collective variable has been checked. The committor analysis reported in the section is essential in order to study also the mechanism of the process.

On the basis of the results of Sec.(6), a possible mechanism of the nucleation of the Silicon nano-particle embedded in a-SiO_2 can be given. Since the $\mathcal{Q}_6$ is an adequate collective coordinate only for the small nano-particles and not for large ones, the mechanism of nucleation is sensitive to the size of the nano-particle.

Since the $\mathcal{Q}_6$ is able to detect only the overall degree of order, in the case of small nano-particles the nucleation is an overall and homogeneous process. While for large nano-particles (i.e. in bulk phase) the nucleation process is a heterogeneous process that involve nucleation sites.

In Sec.(4) the Silicon diffusion process is investigated. A set of mechanisms of diffusion have been identified. In particular, the three most important mechanisms governing the diffusion are: i) the tendency of undercoordinated O atoms to restore the complete coordination, ii) the tendency of undercoordinated Si atom to restore the complete coordination, and iii) the swapping of Si-O bonds for Si-Si bonds (and vice versa). This behavior has been interpreted in terms of the abundance of defects compatible with the identified mechanisms. In order to measure the contribution of each of them to the diffusivity, a method to compute the diffusivity associated to each mechanism has been developed. At low Silicon concentration the O-driven mechanism is responsible for the diffusion of Si while at higher concentration the diffusion is due to the Si-driven and bond-swapping mechanisms. These results, and, in particular, the dependency of the relevance of the various mechanisms on the Si concentration and the thermodynamical conditions, suggest two main conclusions: i) a single diffusion path is not adequate for describing this phenomenon as it might depend on the local Si concentration (fluctuations of stoichiometry might occur in real samples) and iii) temperature deeply affects the diffusion mechanism.

Appendix A

Derivatives of the Tersoff potential

0.1 Potential

In the Tersoff like potential described in Ref.[19], as reported in the Sec.(2) the general equation for the energy is

$$E = \frac{1}{2}\sum_{i\neq j} V_{ij} + N_I \sum_I E_I^0 + \sum_i E_i^c \tag{A.1}$$

where V_{ij} is given by

$$V_{ij} = f_{ij}^{IJ}\left(A_{IJ}\, e^{-\lambda_{IJ}\, r_{ij}} \; - \; b_{ij}^{IJ}\, B_{IJ}\, e^{-\mu_{IJ}\, r_{ij}}\right) \tag{A.2}$$

the V_{ij} explicit depends on

$$V_{ij} = V_{ij}(r_{ij},\, b_{ij}) \tag{A.3}$$

The cutoff function is defined as

$$f_{ij}^{IJ} = \begin{cases} 1 & \text{if } \mathrm{r_{ij}} \leq \mathrm{R_{IJ}} \\ \frac{1}{2}\left[1 + \cos\left(\pi \frac{r_{ij}-R_{IJ}}{S_{IJ}-R_{IJ}}\right)\right] & \text{if } \mathrm{R_{IJ}} < \mathrm{r_{ij}} \leq \mathrm{S_{IJ}} \\ 0 & \text{if } \mathrm{r_{ij}} > \mathrm{S_{IJ}} \end{cases} \tag{A.4}$$

The damping factor as

$$b_{ij}^{IJ} = \chi_{IJ}\left[1 + \left(\beta_I\, \zeta_{ij}^{IJ}\right)^{n_I}\right]^{-\frac{1}{2n_I}} \tag{A.5}$$

and it depends on

$$b_{ij} = b_{ij}(\zeta_{ij}) \tag{A.6}$$

The ζ_{ij} function is defined by

$$\zeta_{ij}^{IJ} = \sum_{k \neq i,j} f_{ik}^{IK}\, e_{ijk}^{IJK}\, t_{ijk}^{I} \tag{A.7}$$

and it depends on the distance r_{ij} and r_{ik} and on the angle θ_{ijk} between these two distances

$$\zeta_{ij} = \zeta_{ij}(r_{ij}, r_{ik}, \theta_{ijk}) \tag{A.8}$$

The radial contribution is given by

$$e_{ijk}^{IJK} = e^{(\mu_{IJ}\, r_{ij} - \mu_{IK}\, r_{ik})^{m_I}}. \tag{A.9}$$

while the angular by

$$t_{ijk}^{I} = 1 + \frac{c_I^2}{d_I^2} - \frac{c_I^2}{d_I^2 + (h_I - \cos(\theta_{ijk}))^2} \tag{A.10}$$

The augmented part of the Billeter *et al.* potential is defined as

$$E_i^c = c_{I,1}\, \Delta z_i + c_{I,2}\, \Delta z_i^2 \tag{A.11}$$

where the term Δz_i is given by

$$\Delta z_i = \frac{z_i - z_I^0}{|z_i - z_I^0|}\, f_s(|z_i - z_I^0|) \tag{A.12}$$

with

$$z_i = \sum_{j \neq i} f_{ij}^{IJ}\, b_{ij}^{IJ} \tag{A.13}$$

and

$$|f_s(z)| = int(|z|) + \begin{cases} 0 & \text{if } |\mathrm{z}| \leq \mathrm{z_T} - \mathrm{z_B}, \\ \frac{1}{2}\left[1 + \sin\left(\pi \frac{|z| - z_T}{2 z_B}\right)\right] & \text{if } \mathrm{z_T} - \mathrm{z_B} < |\mathrm{z}| \leq \mathrm{z_T} + \mathrm{z_B}, \\ 1 & \text{if } \mathrm{z_T} + \mathrm{z_B} < |\mathrm{z}| \end{cases} \tag{A.14}$$

0.2 First Derivatives

The term V_{ij} of Eq.A.2 depends on r_{ij} and b_{ij}, see Eq.A.3. Its derivatives is given by:

$$\frac{\partial V_{ij}}{\partial q_l^\alpha} = \frac{\partial V_{ij}}{\partial r_{ij}} \frac{\partial r_{ij}}{\partial q_l^\alpha} (1 - \delta_{lk}) + \frac{\partial V_{ij}}{\partial b_{ij}} \frac{\partial b_{ij}}{\partial q_l^\alpha} \tag{A.15}$$

where δ_{lk} is the Kronecker delta. The first term in the Eq.A.15 contains the derivatives of the distance r_{ij} with respect of the generic component of the i-th atom, which is given by

$$\frac{\partial r_{ij}}{\partial q_i^\alpha} = -\frac{\partial r_{ij}}{\partial q_j^\alpha} = \frac{q_i^\alpha - q_i^\alpha}{r_{ij}} = \frac{q_{ij}^\alpha}{r_{ij}}. \tag{A.16}$$

The first term of Eq.A.15 contains also the explicit derivative of V_{ij} from the distance r_{ij}, which is given by

$$\begin{aligned} \frac{\partial V_{ij}}{\partial r_{ij}} = & \frac{1}{2} \frac{\partial f_{ij}}{\partial r_{ij}} \left(A_{IJ}\, e^{-\lambda_{IJ}\, r_{ij}} - b_{ij}\, B_{IJ}\, e^{-\mu_{IJ}\, r_{ij}} \right) \\ & + \frac{1}{2} f_{ij} \left(-\lambda_{IJ} A_{IJ}\, e^{-\lambda_{IJ}\, r_{ij}} + \mu_{IJ}\, b_{ij}\, B_{IJ}\, e^{-\mu_{IJ}\, r_{ij}} \right) \end{aligned} \tag{A.17}$$

where the derivative of the cutoff function from a generic distance r_{il} takes the form

$$\frac{\partial f_{ix}}{\partial r_{il}} = \begin{cases} 0 & \text{se} \quad \mathrm{r_{il}} \leq \mathrm{R_{IL}} \\ -\frac{\frac{1}{2}\pi\, \delta_{lx}}{S_{IL} - R_{IL}} \sin\left(\pi\, \frac{r_{il} - R_{IL}}{S_{IL} - R_{IL}} \right) & \text{se} \quad \mathrm{R_{IL}} < \mathrm{r_{il}} \leq \mathrm{S_{IL}} \\ 0 & \text{se} \quad \mathrm{r_{il}} > \mathrm{S_{IL}} \end{cases} \tag{A.18}$$

The second term of the Eq.A.17 is more complex and it is composed by two derivatives. The first is the derivative of V_{ij} with respect the b_{ij} and it is given by

$$\frac{\partial V_{ij}}{\partial b_{ij}} = -\frac{1}{2} f_{ij}\, B_{IJ} e^{-\mu_{IJ}\, r_{ij}}. \tag{A.19}$$

The second is the derivative of b_{ij} with respect of the generic component q_l^α. The term b_{ij} depends only by ζ_{ij} (see Eqs.A.5,A.6) and its derivative takes the form

$$\frac{\partial b_{ij}}{\partial q_l^\alpha} = \frac{\partial b_{ij}}{\partial \zeta_{ij}} ; \frac{\partial \zeta_{ij}}{\partial q_l^\alpha} \tag{A.20}$$

where the first term is given by

$$\frac{\partial b_{ij}}{\partial \zeta_{ij}} = -\frac{1}{2} \chi_{IJ}\, \beta_I^2\, (\beta_I \zeta_{ij})^{n_I - 1} \left[1 + (\beta \zeta_{ij})^{n_I} \right]^{-\frac{1}{2n_I} - 1} \tag{A.21}$$

and the second, depending on the distances r_{ij}, r_{ik} and on the angle θ_{ijk} between these two bonds (see Eqs.A.7,A.8), by

$$\begin{aligned}\frac{\partial \zeta_{ij}}{\partial q_l^\alpha} &= \frac{\partial \zeta_{ij}}{\partial r_{ij}} \frac{\partial r_{ij}}{\partial q_l^\alpha} (1-\delta_{lk}) + \sum_k \left[\frac{\partial \zeta_{ij}}{\partial r_{ik}} \frac{\partial r_{ik}}{\partial q_l^\alpha} (1-\delta_{lj}) \right] \\ &+ \sum_k \left[\frac{\partial \zeta_{ij}}{\partial \cos(\theta_{ijk})} \frac{\partial \cos(\theta_{ijk})}{\partial q_l^\alpha} \right]\end{aligned} \tag{A.22}$$

where the derivatives of the distances r_{ij} and r_{ik} with respect of the generic component q_l^α are expressed with the Eq.A.16. While the derivatives of the cosine of the angle θ_{ijk} with respect of the generic component is given by

$$\frac{\partial \cos(\theta_{ijk})}{\partial q_l^\alpha} = -\frac{1}{r_{il}} \left[\frac{q_{im}^\alpha}{r_{im}} - \frac{q_{il}^\alpha}{r_{il}} \cos(\theta_{ijk}) \right] \tag{A.23}$$

and they obey to this relation

$$\frac{\partial \cos(\theta_{ijk})}{\partial q_i^\alpha} = -\frac{\partial \cos(\theta_{ijk})}{\partial q_j^\alpha} - \frac{\partial \cos(\theta_{ijk})}{\partial q_k^\alpha}. \tag{A.24}$$

In the Eq.A.22 there are the radial and angular derivatives of the ζ_{ij} that take, respectively, the form

$$\frac{\partial \zeta_{ij}}{\partial r_{il}} = \sum_k \left[f_{ik} \frac{\partial e_{ijk}}{\partial r_{il}} t_{ijk} + \frac{\partial f_{ik}}{\partial r_{il}} e_{ijk} t_{ijk} (1-\delta_{lj}) \right] \tag{A.25}$$

and

$$\frac{\partial \zeta_{ij}}{\partial \cos(\theta_{ijk})} = f_{ik}\, e_{ijk} \frac{\partial t_{ijk}}{\partial \cos(\theta_{ijk})} \tag{A.26}$$

where the radial derivatives of the cutoff function of the second term in the Eq.A.25 is given by the Eq.A.18, while the radial derivatives of the e_{ijk} function is given by

$$\frac{\partial e_{ijk}}{\partial r_{il}} = \left[m_I\, e^{(\mu_{IJ}\, r_{ij} - \mu_{IK}\, r_{ik})^{m_I}} (\mu_{IJ}\, r_{ij} - \mu_{IK}\, r_{ik})^{m_I - 1} \right] (\mu_{IJ}\, \delta_{lj} - \mu_{IK}\, \delta_{lk}) \tag{A.27}$$

and the angular derivatives of the function t_{ijk} by

$$\frac{\partial t_{ijk}}{\partial \cos(\theta_{ijk})} = \frac{-2\, c_I^2\, (h_I - \cos(\theta_{ijk}))}{\left[d_I^2 + (h_I - \cos(\theta_{ijk}))^2 \right]^2}. \tag{A.28}$$

Finally the first derivatives of the term b_{ij} with respect to a generic component α of the coordinates of the l-th atom, q_l^α, is given by

$$\frac{\partial b_{ij}}{\partial q_l^\alpha} = \frac{\partial b_{ij}}{\partial \zeta_{ij}} \left\{ f_{ik} \frac{\partial e_{ijk}}{\partial r_{il}} t_{ijk} \left[\frac{\partial r_{ij}}{\partial q_l^\alpha} (1 - \delta_{lk}) + \sum_k \frac{\partial r_{ik}}{\partial q_l^\alpha} (1 - \delta_{lj}) \right] + \sum_k \left[f_{ik} e_{ijk} \frac{\partial t_{ijk}}{\partial \cos(\theta_{ijk})} \frac{\partial \cos(\theta_{ijk})}{\partial q_l^\alpha} \right] + \frac{\partial f_{ik}}{\partial r_{il}} e_{ijk} t_{ijk} \frac{\partial r_{il}}{\partial q_l^\alpha} (1 - \delta_{lj}) \right\} \tag{A.29}$$

0.3 Second Derivatives

The second derivative of the pair potential term V_{ij} with respect to two generic component, α and β, of two generic atoms l and m is given by

$$\begin{aligned} \frac{\partial}{\partial q_m^\beta} \left(\frac{\partial V_{ij}}{\partial q_l^\alpha} \right) = & \frac{\partial r_{ij}}{\partial q_l^\alpha} \frac{\partial}{\partial q_m^\beta} \left(\frac{\partial V_{ij}}{\partial r_{ij}} \right) + \frac{\partial b_{ij}}{\partial q_l^\alpha} \frac{\partial}{\partial q_m^\beta} \left(\frac{\partial V_{ij}}{\partial b_{ij}} \right) \\ & + \frac{\partial V_{ij}}{\partial r_{ij}} \frac{\partial}{\partial q_m^\beta} \left(\frac{\partial r_{ij}}{\partial q_l^\alpha} \right) + \frac{\partial V_{ij}}{\partial b_{ij}} \frac{\partial}{\partial q_m^\beta} \left(\frac{\partial b_{ij}}{\partial q_l^\alpha} \right) \end{aligned} \tag{A.30}$$

This derivative is composed by four terms. The first two terms are composed by a first derivative with respect the generic component of, respectively, r_{ij} and b_{ij}. The derivatives of these two terms are analyzed in the previous section and they are given by Eq.A.16 and Eq.A.20, respectively. The other two components are the derivatives of the two first derivatives given in the previous sections (see Eq.A.17 and Eq.A.19). The derivative of V_{ij} with respect to the distance r_{ij} depends explicitly on r_{ij} and b_{ij} (see Eq.A.17)

$$\frac{\partial V_{ij}}{\partial r_{ij}} = \frac{\partial V_{ij}}{\partial r_{ij}} (r_{ij}, b_{ij}) \tag{A.31}$$

thus its derivative is

$$\frac{\partial}{\partial q_l^\alpha} \left(\frac{\partial V_{ij}}{\partial r_{ij}} \right) = \frac{\partial}{\partial r_{ij}} \left(\frac{\partial V_{ij}}{\partial r_{ij}} \right) \frac{\partial r_{ij}}{\partial q_l^\alpha} + \frac{\partial}{\partial b_{ij}} \left(\frac{\partial V_{ij}}{\partial r_{ij}} \right) \frac{\partial b_{ij}}{\partial q_l^\alpha} \tag{A.32}$$

where the last derivatives of the two terms are given by Eq.A.16 and Eq.A.20, respectively. While the second derivative with respect of the r_{ij} distance of the pair interaction is given by

$$\begin{aligned}\frac{\partial}{\partial r_{ij}}\left(\frac{\partial V_{ij}}{\partial r_{ij}}\right) &= \frac{1}{2}\frac{\partial^2 f_{ij}}{\partial r_{ij}^2}\left[A_{IJ}\, e^{-\lambda_{IJ}\, r_{ij}} - b_{ij}\, B_{IJ}\, e^{-\mu_{IJ}\, r_{ij}}\right] \\ &+ \frac{\partial f_{ij}}{\partial r_{ij}}\left[-\lambda_{IJ}\, A_{IJ}\, e^{-\lambda_{IJ}\, r_{ij}} + \mu_{IJ}\, b_{ij}\, B_{IJ}\, e^{-\mu_{IJ}\, r_{ij}}\right] \\ &+ \frac{1}{2}\, f_{ij}\left[\lambda_{IJ}^2\, A_{IJ}\, e^{-\lambda_{IJ}\, r_{ij}} - \mu_{IJ}^2\, b_{ij}\, B_{IJ}\, e^{-\mu_{IJ}\, r_{ij}}\right]\end{aligned} \tag{A.33}$$

where the second derivative with respect of two generic distances of the cutoff function is given by

$$\frac{\partial}{\partial r_{im}}\frac{\partial f_{ix}}{\partial r_{il}} = \begin{cases} 0 & \text{se} \quad \mathrm{r_{il}} < \mathrm{R_{IL}} \\ -\frac{\frac{1}{2}\pi^2\,\delta_{lx}\,\delta_{mx}}{(S_{IL}-R_{IL})^2}\cdot\cos\left(\pi\,\frac{r_{il}-R_{IL}}{S_{IL}-R_{IL}}\right) & \text{se} \quad \mathrm{R_{IL}} < \mathrm{r_{il}} \leq \mathrm{S_{IL}} \\ 0 & \text{se} \quad \mathrm{r_{il}} > \mathrm{S_{IL}} \end{cases} \tag{A.34}$$

while the first derivative of the second term in Eq.A.32 is given by

$$\frac{\partial}{\partial b_{ij}}\left(\frac{\partial V_{ij}}{\partial r_{ij}}\right) = \frac{\partial}{\partial r_{ij}}\left(\frac{\partial V_{ij}}{\partial b_{ij}}\right) = -\frac{1}{2}\, B_{IJ}\, e^{-\,\mu_{IJ}\, r_{ij}}\,\frac{\partial f_{ij}}{\partial r_{ij}} + \frac{1}{2}\,\mu_{IJ}\, B_{IJ} e^{-\,\mu_{IJ}\, r_{ij}}\, f_{ij} \tag{A.35}$$

Finally the last derivative of the second term in the Eq.A.30 is given by

$$\frac{\partial}{\partial q_l^\alpha}\left(\frac{\partial V_{ij}}{\partial b_{ij}}\right) = \frac{\partial}{\partial r_{ij}}\left(\frac{\partial V_{ij}}{\partial b_{ij}}\right)\frac{\partial r_{ij}}{\partial q_l^\alpha} \tag{A.36}$$

here the first term is equal to the previous equation (Eq.A.35) and the last derivative is given in the previous section (see Eq.A.16).

The second two terms of Eq.A.30 consist of a product of a first derivative, $\partial V_{ij}/\partial r_{ij}$ for the former (see Eq.A.17) and $\partial V_{ij}/\partial b_{ij}$ for the latter (see Eq.A.19), for a second derivatives with respect of two generic component of two atoms. The second derivatives of the distance r_{ij} can be obtained by the following generic equation

$$\frac{\partial}{\partial q_m^\beta}\left(\frac{\partial r_{ix}}{\partial q_l^\alpha}\right) = \frac{(\delta_{li}-\delta_{lx})\,(\delta_{mx}-\delta_{mi})}{r_{ix}}\left[\delta_{\alpha\beta} - \left(\frac{q_{ix}^\alpha}{r_{ix}}\,\frac{q_{ix}^\beta}{r_{ix}}\right)\right]. \tag{A.37}$$

The second order derivative of the last term in the Eq.A.30 is given by

$$\frac{\partial}{\partial q_m^\beta}\left(\frac{\partial b_{ij}}{\partial q_l^\alpha}\right) = \frac{\partial \zeta_{ij}}{\partial q_l^\alpha}\,\frac{\partial}{\partial q_m^\beta}\left(\frac{\partial b_{ij}}{\partial \zeta_{ij}}\right) + \frac{\partial b_{ij}}{\partial \zeta_{ij}}\,\frac{\partial}{\partial q_m^\beta}\left(\frac{\partial \zeta_{ij}}{\partial q_l^\alpha}\right) \tag{A.38}$$

where the first derivative of the first term is analyzed in the Eq.A.22 and the the second derivative of the first term is given by

$$\frac{\partial}{\partial q_m^\beta}\left(\frac{\partial b_{ij}}{\partial \zeta_{ij}}\right) = \frac{\partial}{\partial \zeta_{ij}}\left(\frac{\partial b_{ij}}{\partial \zeta_{ij}}\right)\frac{\partial \zeta_{ij}}{\partial q_m^\beta} \tag{A.39}$$

where $\partial\zeta_{ij}/\partial q_m^\beta$ is given in Eq.A.22 and the other term is given by

$$\frac{\partial}{\partial \zeta_{ij}}\left(\frac{\partial b_{ij}}{\partial \zeta_{ij}}\right) = -\frac{1}{2}\chi_{IJ}\beta_I^2\Bigg[(n_I-1)\,(\beta_I\zeta_{ij})^{n_I-2}\,[1+(\beta\zeta_{ij})^{n_I}]^{-\frac{1}{2n_I}-1} \\ (n_I+\frac{1}{2})\,(\beta_I\zeta_{ij})^{2(n_I-1)}\,[1+(\beta\zeta_{ij})^{n_I}]^{-\frac{1}{2n_I}-2}\Bigg]. \tag{A.40}$$

The last term in the Eq.A.38 is given by

$$\begin{aligned}\frac{\partial}{\partial q_m^\beta}\left(\frac{\partial b_{ij}}{\partial q_l^\alpha}\right) &= \frac{\partial}{\partial q_m^\beta}\left(\frac{\partial \zeta_{ij}}{\partial r_{ij}}\right)\frac{\partial r_{ij}}{\partial q_l^\alpha}(1-\delta_{lk}) + \frac{\partial \zeta_{ij}}{\partial r_{ij}}\frac{\partial}{\partial q_m^\beta}\left(\frac{\partial r_{ij}}{\partial q_l^\alpha}\right)(1-\delta_{lk}) \\ &+ \sum_k\left[\frac{\partial}{\partial q_m^\beta}\left(\frac{\partial \zeta_{ij}}{\partial r_{ik}}\right)\frac{\partial r_{ik}}{\partial q_l^\alpha}(1-\delta_{lj})\right] \\ &+ \sum_k\left[\frac{\partial \zeta_{ij}}{\partial r_{ik}}\frac{\partial}{\partial q_m^\beta}\left(\frac{\partial r_{ik}}{\partial q_l^\alpha}\right)(1-\delta_{lj})\right] \\ &+ \sum_k\left[\frac{\partial}{\partial q_m^\beta}\left(\frac{\partial \zeta_{ij}}{\partial \cos(\theta_{ijk})}\right)\frac{\partial \cos(\theta_{ijk})}{\partial q_l^\alpha}\right] \\ &+ \sum_k\left[\frac{\partial \zeta_{ij}}{\partial \cos(\theta_{ijk})}\frac{\partial}{\partial q_m^\beta}\left(\frac{\partial \cos(\theta_{ijk})}{\partial q_l^\alpha}\right)\right]\end{aligned} \tag{A.41}$$

where the first three terms contain a new term that can be obtained from this general formula

$$\begin{aligned}\frac{\partial}{\partial q_m^\beta}\left(\frac{\partial \zeta_{ij}}{\partial r_{il}}\right) &= \frac{\partial}{\partial r_{ij}}\left(\frac{\partial \zeta_{ij}}{\partial r_{il}}\right)\frac{\partial r_{ij}}{\partial q_m^\beta}(1-\delta_{mk}) + \frac{\partial}{\partial r_{ik}}\left(\frac{\partial \zeta_{ij}}{\partial r_{il}}\right)\frac{\partial r_{ik}}{\partial q_m^\beta}(1-\delta_{mj}) \\ &+ \frac{\partial}{\partial \cos(\theta_{ijk})}\left(\frac{\partial \zeta_{ij}}{\partial r_{il}}\right)\frac{\partial \cos(\theta_{ijk})}{\partial q_m^\beta}\end{aligned} \tag{A.42}$$

with the double radial derivatives of ζ_{ij} that is

$$\frac{\partial}{\partial r_{im}}\left(\frac{\partial \zeta_{ij}}{\partial r_{il}}\right) = \sum_k \left[f_{ik}\,\frac{\partial^2 e_{ijk}}{\partial r_{im}\partial r_{il}}\,t_{ijk}\right] + \frac{\partial f_{ik}}{\partial r_{im}}\,\frac{\partial e_{ijk}}{\partial r_{il}}\,t_{ijk}\,(1-\delta_{lj})(1-\delta_{mj}) + \frac{\partial f_{ik}}{\partial r_{il}}\,\frac{\partial e_{ijk}}{\partial r_{im}}\,t_{ijk}\;\delta_{lk}\delta_{mk} + \frac{\partial^2 f_{ik}}{\partial r_{im}\partial r_{il}}\,e_{ijk}\,t_{ijk}\;\delta_{lk}\delta_{mk} \tag{A.43}$$

in which the only new term is the second derivative of the function e_{ijk} with respect to the generic distances r_{il} and r_{im} that is given by

$$\frac{\partial}{\partial r_{im}}\left(\frac{\partial e_{ijk}}{\partial r_{il}}\right) = m_I\, e^{(\mu_{IJ}\, r_{ij} - \mu_{IK}\, r_{ik})^{m_I}} \left[(m_I-1)\,(\mu_{IJ}\, r_{ij} - \mu_{IK}\, r_{ik})^{m_I-2} + m_I\,(\mu_{IJ}\, r_{ij} - \mu_{IK}\, r_{ik})^{2(m_I-1)}\right] (\mu_{IJ}\,\delta_{lj} - \mu_{IK}\,\delta_{lk})\,(\mu_{IJ}\,\delta_{mj} - \mu_{IK}\,\delta_{mk}) \tag{A.44}$$

and the angular derivative of the radial derivative of ζ_{ij} given by

$$\frac{\partial}{\partial \cos(\theta_{ijk})}\left(\frac{\partial \zeta_{ij}}{\partial r_{il}}\right) = \sum_k \left[f_{ik}\,\frac{\partial e_{ijk}}{\partial r_{il}}\,\frac{\partial t_{ijk}}{\partial \cos(\theta_{ijk})}\right] + \frac{\partial f_{ik}}{\partial r_{il}}\,e_{ijk}\,\frac{\partial t_{ijk}}{\partial \cos(\theta_{ijk})}\,(1-\delta_{lj}). \tag{A.45}$$

The fifth term in the Eq.A.41 contains a new term that is given by

$$\begin{aligned}\frac{\partial}{\partial q_m^\beta}\left(\frac{\partial \zeta_{ij}}{\partial \cos(\theta_{ijk})}\right) &= \frac{\partial}{\partial r_{ij}}\left(\frac{\partial \zeta_{ij}}{\partial \cos(\theta_{ijk})}\right)\frac{\partial r_{ij}}{\partial q_m^\beta}\,(1-\delta_{mk}) \\ &+ \frac{\partial}{\partial r_{ik}}\left(\frac{\partial \zeta_{ij}}{\partial \cos(\theta_{ijk})}\right)\frac{\partial r_{ik}}{\partial q_m^\beta}\,(1-\delta_{mj}) \\ &+ \frac{\partial}{\partial \cos(\theta_{ijk})}\left(\frac{\partial \zeta_{ij}}{\partial \cos(\theta_{ijk})}\right)\frac{\partial \cos(\theta_{ijk})}{\partial q_m^\beta}\end{aligned} \tag{A.46}$$

where

$$\frac{\partial}{\partial \cos(\theta_{ijk})}\left(\frac{\partial \zeta_{ij}}{\partial \cos(\theta_{ijk})}\right) = f_{ik}\,e_{ijk}\,\frac{\partial}{\partial \cos(\theta_{ijk})}\left(\frac{\partial t_{ijk}}{\partial \cos(\theta_{ijk})}\right) \tag{A.47}$$

with

$$\frac{\partial}{\partial \cos(\theta_{ijk})}\left(\frac{\partial t_{ijk}}{\partial \cos(\theta_{ijk})}\right) = \frac{2\,c_I^2}{\left[d_I^2 + (h_I - \cos(\theta_{ijk}))^2\right]^2} + \frac{8\,c_I^2\,(h_I - \cos(\theta_{ijk}))^2}{\left[d_I^2 + (h_I - \cos(\theta_{ijk}))^2\right]^3} \tag{A.48}$$

The last term in Eq.A.41 contains the second derivative of the cosine of the angle θ_{ijk} with respect to two generic components of two atoms. This derivative can be obtained by the following generic formula

$$\begin{aligned}\frac{\partial}{\partial q_m^\beta}\left(\frac{\partial\cos(\theta_{ijk})}{\partial q_l^\alpha}\right) = \frac{-(1-\delta_{lm})}{r_{ij}r_{ik}}\Bigg[&-\delta_{\alpha\beta}+\frac{q_{ij}^\alpha}{r_{ij}}\frac{q_{ij}^\beta}{r_{ij}}+\frac{q_{ik}^\alpha}{r_{ik}}\frac{q_{ik}^\beta}{r_{ik}}\\&-\left(\frac{q_{ij}^\alpha}{r_{ij}}\frac{q_{ik}^\beta}{r_{ik}}\cdot\delta_{lj}+\frac{q_{ij}^\beta}{r_{ij}}\frac{q_{ik}^\alpha}{r_{ik}}\delta_{lk}\right)\cos(\theta_{ijk})\Bigg]\\&+\frac{-\delta_{lm}}{r_{il}^2}\left[\frac{q_{ij}^\alpha}{r_{ij}}\frac{q_{ik}^\beta}{r_{ik}}+\frac{q_{ij}^\beta}{r_{ij}}\frac{q_{ik}^\alpha}{r_{ik}}+\left(\delta_{\alpha\beta}-3\frac{q_{il}^\alpha}{r_{il}}\frac{q_{il}^\beta}{r_{il}}\right)\cos(\theta_{ijk})\right]\end{aligned} \tag{A.49}$$

These second order derivatives respect the following relation

$$\begin{aligned}\frac{\partial}{\partial q_i^\beta}\left(\frac{\partial\cos(\theta_{ijk})}{\partial q_l^\alpha}\right) = \frac{\partial}{\partial q_l^\alpha}\left(\frac{\partial\cos(\theta_{ijk})}{\partial q_i^\beta}\right) =\\-\frac{\partial}{\partial q_j^\beta}\left(\frac{\partial\cos(\theta_{ijk})}{\partial q_l^\alpha}\right)-\frac{\partial}{\partial q_k^\beta}\left(\frac{\partial\cos(\theta_{ijk})}{\partial q_l^\alpha}\right)\end{aligned} \tag{A.50}$$

Bibliography

[1] G. Moore, Electronics **38**, 1 (1965).

[2] D. Kovalev, H. Heckler, M. Ben-Chorin, G. Polisski, M. Schwartzkopff, and F. Koch, Phys. Rev. Lett. **81**, 2803 (1998).

[3] B. Delley and E. F. Steigmeier, Phys. Rev. B **47**, 1397 (1993).

[4] L. T. Canham, Appl. Phys. Lett. **57**, 1046 (1990).

[5] B. Gelloz, T. Nakagawa, and N. Koshida, Appl. Phys. Lett. **73**, 2021 (1998).

[6] H. Mizuno, H. Koyama, and N. Koshida, Appl. Phys. Lett. **69**, 3779 (1996).

[7] O. Akcakir, J. Therrien, G. Belomoin, N. Barry, J. D. Muller, E. Gratton, and M. Nayfeh, Appl. Phys. Lett. **76**, 1857 (2000).

[8] G. M. Torrie and J. P. Valleau, J. Comp. Phys. **23**, 187 (1977).

[9] J. P. Valleau, J. Comp. Phys. **96**, 193 (1991).

[10] J. P. Valleau, J. Chem. Phys. **99**, 4718 (1993).

[11] A. Laio and M. Parrinello, Proc. Nat. Acad. Sci. USA **99**, 12562 (2002).

[12] L. Maragliano and E. Vanden-Eijnden, Chem. Phys. Lett. **426**, 168 (2006).

[13] H. Eyring, J. Chem. Phys. **3**, 107 (1935).

[14] F. H. Stillinger and T. A. Weber, Phys. Rev. B **31**, 5262 (1985).

[15] B. W. H. van Beest, G. J. Kramer, and R. A. van Santen, Phys. Rev. Lett. **64**, 1955 (1990).

[16] J. Tersoff, Phys. Rev. Lett. **56**, 632 (1986).

[17] J. Tersoff, Phys. Rev. B **37**, 6991 (1988).

[18] J. Tersoff, Phys. Rev. B **39**, 5566 (1989).

[19] S. R. Billeter, A. Curioni, D. Fischer, and W. Andreoni, Phys. Rev. B **73**, 155329 (2006).

[20] S. R. Billeter, A. Curioni, D. Fischer, and W. Andreoni, Phys. Rev. B **79**, 169904 (2009).

[21] D. Fischer, A. Curioni, S. Billeter, and W. Andreoni, Appl. Phys. Lett. **88**, 012101 (2006).

[22] M. Ippolito, S. Meloni, and L. Colombo, Appl. Phys. Lett. **93**, 153109 (2008).

[23] T. Laino, D. Donadio, and I. W. Kuo, Phys. Rev. B **76**, 195210 (2007).

[24] I. Saika-Voivod, F. Sciortino, T. Grande, and P. H. Poole, Phys. Rev. E **70**, 061507 (2004).

[25] G. J. Martyna, M. L. Klein, and M. Tuckerman, J. Chem. Phys. **97**, 2635 (1992).

[26] R. W. G. Wyckoff, *Crystal Structures (Comparative Studies in Behavioral Science: A Wiley Series)* (John Wiley & Sons, 1969), 2nd ed.

[27] K. Kihara, Eur J Mineral **2**, 63 (1990).

[28] W. A. Dollase and W. H. Baur, American Mineralogist **61**, 971 (1976).

[29] L. Levien and C. T. Prewitt, American Mineralogist **66**, 324 (1981).

[30] X. X. Wang, J. G. Zhang, L. Ding, B. W. Cheng, W. K. Ge, J. Z. Yu, and Q. M. Wang, Phys. Rev. B **72**, 195313 (2005).

[31] D. Yu, G. S. Hwang, T. A. Kirichenko, and S. K. Banerjee, Phys. Rev. B **72**, 205204 (2005).

[32] G. Henkelman and H. Jnsson, J. Chem. Phys. **113**, 9978 (2000).

[33] G. Henkelman, B. P. Uberuaga, and H. Jnsson, J. Chem. Phys. **113**, 9901 (2000).

[34] A. D. Fano and G. Jacucci, Phys. Rev. Lett. **39**, 950 (1977).

[35] P. A. V. Johnson, A. C. Wright, and R. N. Sinclair, J. Non-Cryst. Sol. **58**, 109 (1983).

[36] S. Susman, K. J. Volin, D. L. Price, M. Grimsditch, J. P. Rino, R. K. Kalia, P. Vashishta, G. Gwanmesia, Y. Wang, and R. C. Liebermann, Phys. Rev. B **43**, 1194 (1991).

[37] J. Sarnthein, A. Pasquarello, and R. Car, Phys. Rev. B **52**, 12690 (1995).

[38] M. Uematsu, H. Kageshima, Y. Takahashi, S. Fukatsu, K. M. Itoh, K. Shiraishi, and U. Gosele, Appl. Phys. Lett. **84**, 876 (2004).

[39] T. Takahashi, S. Fukatsu, K. M. Itoh, M. Uematsu, A. Fujiwara, H. Kageshima, Y. Takahashi, and K. Shiraishi, J. Appl. Phys. **93**, 3674 (2003).

[40] D. Tsoukalas, C. Tsamis, and P. Normand, J. Appl. Phys. **89**, 7809 (2001).

[41] D. Mathiot, J. P. Schunck, M. Perego, M. Fanciulli, P. Normand, C. Tsamis, and D. Tsoukalas, J. Appl. Phys. **94**, 2136 (2003).

[42] F. Iacona, J. Appl. Phys. **95**, 3723 (2004).

[43] I. Stenger, B. Gallas, L. Siozade, C. Kao, S. Chenot, S. Fisson, G. Vuye, and J. Rivory, J. Appl. Phys. **103**, 114303 (2008).

[44] Y. Wakayama, T. Inokuma, and S. Hasegawa, J. Cryst. Growth **183**, 124 (1998).

[45] T. Inokuma, Y. Wakayama, T. Muramoto, R. Aoki, Y. Kurata, and S. Hasegawa, J. Appl. Phys. **83**, 2228 (1998).

[46] S. Boninelli, F. Iacona, G. Franz, C. Bongiorno, C. Spinella, and F. Priolo, J. Phys.: Cond. Mat. **19**, 225003 (2007).

[47] P. J. Steinhardt, D. R. Nelson, and M. Ronchetti, Phys. Rev. B **28**, 784 (1983).

[48] M. Tanemura, Y. Hiwatari, H. Matsuda, T. Ogawa, N. Ogita, and A. Ueda, Prog. Theor. Phys. **58**, 1079 (1977).

[49] J. N. Cape, J. Chem. Phys. **75**, 2366 (1981).

[50] S. Nose and F. Yonezawa, J. Chem. Phys. **84**, 1803 (1986).

[51] W. C. Swope and H. C. Andersen, Phys. Rev. B **41**, 7042 (1990).

[52] S. Torquato, T. M. Truskett, and P. G. Debenedetti, Phys. Rev. Lett. **84**, 2064 (2000).

[53] N. Quirke and P. Sheng, Chem. Phys. Lett. **110**, 63 (1984).

[54] M. J. Uttormark, M. O. Thompson, and P. Clancy, Phys. Rev. B **47**, 15717 (1993).

[55] J. S. van Duijneveldt and D. Frenkel, J. Chem. Phys. **96**, 4655 (1992).

[56] P. R. ten Wolde, M. J. Ruiz-Montero, and D. Frenkel, J. Chem. Phys. **104**, 9932 (1996).

[57] A. Cacciuto and D. Frenkel, Phys. Rev. E **72**, 041604 (2005).

[58] F. Trudu, D. Donadio, and M. Parrinello, Phys. Rev. Lett. **97**, 105701 (2006).

[59] D. J. Earl and M. W. Deem, Phys. Chem. Chem. Phys. **7**, 3910 (2005).

[60] M. Falcioni and M. W. Deem, J. Chem. Phys. **110**, 1754 (1999).

[61] Y. Sugita and Y. Okamoto, Chem. Phys. Lett. **314**, 141 (1999), ISSN 0009-2614.

[62] S. Meloni, M. Rosati, A. Federico, L. Ferraro, A. Mattoni, and L. Colombo, Comp. Phys. Comm. **169**, 462 (2005).

[63] URL `https://cmsportal.caspur.it/index.php/CMPTool`.

[64] URL `http://www.mcs.anl.gov/research/projects/mpi`.

[65] N. Daldosso, M. Luppi, S. Ossicini, E. Degoli, R. Magri, G. Dalba, P. Fornasini, R. Grisenti, F. Rocca, L. Pavesi, et al., Phys. Rev. B **68**, 085327 (2003).

[66] U. Gasser, E. R. Weeks, A. Schofield, P. N. Pusey, and D. A. Weitz, Science **292**, 258 (2001).

[67] K. Kelton and A. Greer, *Nucleation in Condensed Matter* (Elsevier, Amsterdam, 2010).

[68] G. Henkelman, B. P. Uberuaga, and H. Jnsson, J. Chem. Phys. **113**, 9901 (2000).

[69] G. Henkelman and H. Jnsson, J. Chem. Phys. **113**, 9978 (2000).

[70] W. E, W. Ren, and E. Vanden-Eijnden, Phys. Rev. B **66**, 58 (2002).

[71] L. Maragliano, A. Fischer, E. Vanden-Eijnden, and G. Ciccotti, J. Chem. Phys. **125**, 024106 (2006).

[72] C. Dellago, P. G. Bolhuis, F. S. Csajka, and D. Chandler, J. Chem. Phys. **108**, 1964 (1998).

[73] P. G. Bolhuis, D. Chandler, C. Dellago, and P. L. Geissler, Ann. Rev. Phys. Chem. **53**, 291 (2002).

[74] C. Dellago, P. G. Bolhuis, and P. L. Geissler, *Transition Path Sampling* (John Wiley & Sons, Inc., 2003).

[75] J. H. Irving and J. G. Kirkwood, J. Chem. Phys. **18**, 817 (1950).

[76] B. J. Alder and T. E. Wainwright, Phys. Rev. A **1**, 18 (1970).

[77] D. J. Evans and G. P. Morriss, *Statistical mechanics of nonequilibrium liquids* (Cambridge University Press, 2008).

[78] G. Ciccotti and G. Jacucci, Phys. Rev. Lett. **35**, 789 (1975).

[79] G. Ciccotti, G. Jacucci, and I. R. McDonald, J. Stat. Phys. **21**, 1 (1979).

[80] G. Ciccotti, C. Pierleoni, and J. P. Ryckaert, in *Microscopic simulations of complex hydrodynamic phenomena* (Plenum Press, 1992), pp. 25–45.

[81] J. Hansen and L. Verlet, Phys. Rev. **184**, 151 (1969).

[82] A. Milchev and K. Binder, J. Chem. Phys. **114**, 8610 (2001).

[83] R. L. C. Vink, J. Horbach, and K. Binder, J. Chem. Phys. **122**, 134905 (2005).